Gravitational Stability in Complex Colloidal Systems

Samuel Hare

A dissertation submitted to the University of Bristol in accordance with the requirements for award of the degree of Doctor of Philosophy in the Faculty of Science.

School of Chemistry

February 19, 2019

Word Count: 41742

Declaration of Authorship

I declare that the work in this dissertation was carried out in accordance with the requirements of the University's Regulations and Code of Practice for Research Degree Programmes and that it has not been submitted for any other academic award. Except where indicated by specific reference in the text, the work is the candidate's own work. Work done in collaboration with, or with the assistance of, others, is indicated as such. Any views expressed in the dissertation are those of the author.

SIGNED: ..... DATE:.....

"*Do. Or do not. There is no try.*"

Jedi Master Yoda, *Star Wars: Episode V - The Empire Strikes Back.*

Abstract

Gravitational Stability in Complex Colloidal Systems

Weak colloidal gels formed by a depletion attraction are metastable for a finite time before undergoing a catastrophic collapse. This delayed-collapse phenomenon has been previously linked to ageing and the lifetime of a gel explained by the way of single particle-particle bond kinetics. Here we present the dependence of the delay time before collapse (τ_d) on temperature, with a striking two-regime dependence becoming clear, one at low and one at high temperatures. We compare τ_d to the calculated Kramer's escape time (τ_{esc}) and find that the single-bond model is not sufficient to explain the decrease in τ_d observed.

To bridge the microscopic and macroscopic length-scales, we use the technique Particle Tracking Velocimetry (PTV) to probe the mesoscopic length-scale in colloidal gels. This allows us to probe changes in the gel structure using 25 micron fluorescent tracer beads. As well as gaining much more detailed information about the dynamics that occur within colloid-polymer gels, we can track this tracer movement before macroscopic collapse is observed. We find that in the low-temperature regime, tracers are quiescent for a period of time before heterogeneous tracer movement begins in localised regions, which eventually propagates throughout the sample to cause macroscopic collapse. At higher temperatures however, tracer movement is homogeneous and no tracer quiescence is observed.

Acknowledgements

I would like to thank my supervisor Paul Bartlett for all his help and support through out this project. I'd also like to thank my industrial supervisors John Hone and Carl Formstone at Syngenta for their guidance and advice. Thank you to both the EPSRC and Syngenta for funding, with additional thanks to Syngenta and John Hone for access and help performing rheology experiments at Jealott's Hill. I'd also like to thank my project students Charlotte Rowan, Stephen Baker, and Nicola Haynes.

I'd like to thank all my friends in the Soft Matter Group for all their support over the years and for many useful discussions. Furthermore I'd like to thank my teammates in both the Doodlebobs, and Space Created for helping keep me sane these last few years.

Finally I'd like to thank my family, and my girlfriend Rachel, without whose help and encouragement I'm sure I would not have made it to the end of this PhD.

Contents

List of Figures

List of Tables

List of Abbreviations

PMMA	**P**oly(**M**ethyl)**M**eth**A**crylate
AO	**A**sakura **O**osawa
SANS	**S**mall **A**ngle **N**eutron **S**cattering
DLS	**D**ynamic **L**ight **S**cattering
AFM	**A**tomic **F**orce **M**icroscopy
TIRM	**T**otal **I**nternal **R**eflection **M**icroscopy
HEC	**H**ydroxy**E**thyl**C**ellulose
FVT	**F**ree **V**olume **T**heory
MSD	**M**ean **S**quare **D**isplacement
CCD	**C**harge **C**oupled **D**evice
PTV	**P**article **T**racking **V**elocimetry
PDMS	**P**oly**D**i**M**ethyl**S**iloxane
POW	**P**oints **O**f **W**indow
EG	**E**thylene **G**lycol

Chapter 1

Introduction

1.1 Motivation

In this chapter we will explore the current body of scientific understanding concerning colloidal suspensions and their behaviours when a polymer is added, mostly the formation of colloid-polymer gels. We will then discuss the various methods of collapse of colloid-polymer gels, as well as the possible effects changing temperature will have on both the components of the system and the system as a whole.

With many industrial products using gelation as a method of formulation stabilisation, such as agrochemical products, personal care products, and even foods, there is a great deal of interest in improving the fundamental understanding of key parameters to consider when formulating a product. As well as looking for methods to reliably accelerate the collapse of samples, and to find early indicators of a product's long-term stability. However, a product does not just sit on a shelf until it is purchased, it must be shipped to many destinations in many different ways, so understanding the conditions a product is exposed to during transit is of paramount importance. For example, temperatures in a shipping container can vary between 10 and 50 °C [1], a significant variation that may lead to a product being unstable when shipped to one region but not another. Other factors to be considered in the lifetime of a product include humidity, oxygen content and also packaging [2].

Temperature specifically is of great interest, as it has been long used as a method for accelerating the collapse of a formulation, this can be done either by cycling the temperature up and down [3] to stress the sample, or by storing the sample at a constant but higher temperature [4].

(A)

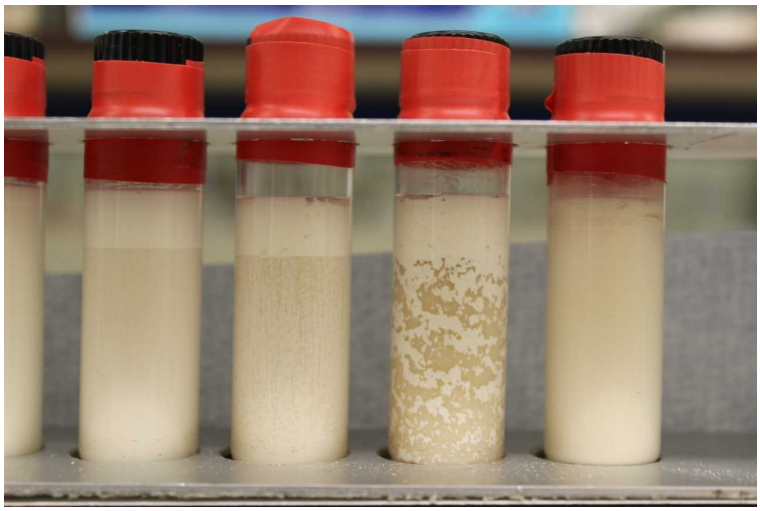

(B)

FIGURE 1.1: Two images showing various simplified model formulations at different stages of collapse. Provided by John Hone (Syngenta UK).

Figure 1.1a shows various simplified model formulations during collapse, the colours are determined by the active ingredient used in the formulation. Most of these samples begin to collapse as soon as they are made. The suspended particles (milled active ingredient crystals) are denser than the solvent so sediment down, leaving a denser colloid phase below a predominantly solvent serum above. With the brown samples, most form a visible interface during collapse, but the clarity of the serum above the dense phase varies between samples, with some giving a clear interface (left-hand side of second row down) and others giving a hard to identify interface (middle top row). This brings about complications when trying to quantify the stability of these formulations, as detecting an interface can be challenging. The yellow

samples in the bottom half of the image have a much clearer serum than the brown samples in most cases, however on the left-hand side many of the samples have no clear interface, but a gradual change in colloid density from high to low. This makes tracking the collapse of the samples over time very difficult as it is almost impossible to quantify the location of the interface.

When combining these complications with the long time-scales associated with industrial formulation collapse (often months to years) it is clear to see how challenging it is to accurately measure the lifetime of a formulation by observation. Firstly, you must wait a long time to observe the collapse, and secondly, even after such a wait, you may gain limited or flawed data.

Figure 1.1b shows close ups of a simplified model formulation that does not collapse in an easily observable manner. The left-hand sample appears to have a clear interface between the bright white top of the sample and cream coloured phase, which could be easily tracked. The middle two samples show a splitting of the cream phase, which is very pronounced in the third sample. Now whilst at first you may think the third sample provides the greater challenge, it is in fact the second sample. It is clear to the eye that the third sample has collapsed, whilst it is much more ambiguous in the second (it is in fact collapsed but very difficult to see).

1.2 Colloidal Suspensions

Colloids are by no means a recent discovery, having been used throughout history. An excellent example of this is the use of colloidal gold in staining glass, with some examples, such as the Lycurgus Cup, dating back to Roman times [5]. However, thankfully, our understanding of colloids and their applications has significantly increased since ancient times, with even colloidal gold finding new, novel applications in various fields such as cancer pro-drug therapies [6].

Colloids come in many forms, such as solid dispersed in a liquid (sol), liquid dispersed in a gas (aerosol), a gas dispersed in a liquid (foam), or as emulsions of oil and water.

1.2.1 Stabilisation Methods

Van der Waals attractions arising from permanent dipoles, induced dipoles and temporary dipoles, caused by variation in the electron cloud of atoms drive aggregation in colloidal suspensions. Whilst these attractions are from the atomic level, the work of Hamaker [7] allows for the attraction between particles to be calculated. Equation 1.1 shows this for short particle-particle separations ($h \ll 2a$), where A is the Hamaker constant, a is the particle radius, and h is particle separation [8]. The Hamaker constant is a material property and is determined by the density and electrical polarisability of the material.

$$V_A = -\frac{Aa}{12h} \tag{1.1}$$

Overcoming these Van der Waals attractions is required for the stabilisation of colloidal suspensions to be achieved.

The first method we will discuss is steric stabilisation [9], in which a colloidal particle has polymers adsorbed to its surface in sufficiently high amounts to introduce a repulsion between colloidal particles. This can be achieved by having a steric layer which is greater in size than the range of attraction between the particles, thus giving a repulsion at long ranges and preventing the particles from entering the range at which they are strongly attracted [10]. A common sterically stabilised colloidal system is poly(methyl)methacrylate (PMMA) particles with a stabilising layer of poly-12-hydroxystearic acid (PHSA). These particles act like almost hard spheres [11], can be dyed with a variety of fluorescent dyes [12], and can be synthesised at a wide range of sizes [13]. This makes them an excellent system to use in exploring the phase behaviour of colloidal suspensions [14], as well as probing the forces that bring about the electrostatic stabilisation of colloids discussed below [15].

As alluded to above, the second form of colloidal stability is achieved through electrostatic stabilisation, in which, rather than a physical layer preventing the particles from attracting, the charged surface of the colloid provides a repulsion against aggregation. This electrostatic stabilisation comes about due to a double layer of counter-ions surrounding the charged surface of the colloid, with co-ions depleted from it. This Stern layer of counter-ions is an immobile monolayer, after which there

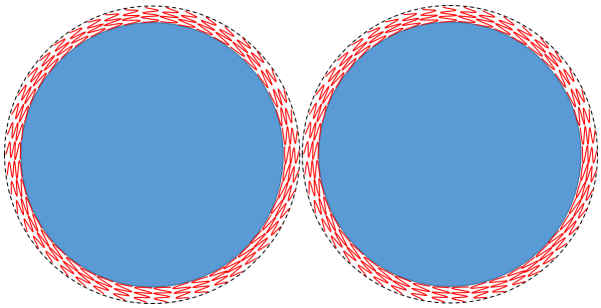

FIGURE 1.2: Diagram showing two colloidal particles with a steric stabilising layer preventing them from aggregating.

is a diffuse (Gouy-Chapman) layer of predominantly counter-ions, before which the distribution of ions evens out in the bulk solution. It is the Stern and diffuse layers that are referred to as the double layer and are what account for the electrostatic repulsion between colloidal particles. The decay length of the double layer can be described by the Debye screening length κ^{-1}, which is shown below in equat8ion 1.2. Where λ_B is Bjerrum length, and ρ_{ion} is the number density of ions (assuming the ions are univalent). The Bjerrum length is defined as the separation at which an electrostatic attraction between two elementary charges becomes comparable to the thermal energy k_BT [16]. From this equation it becomes clear that increasing the salt concentration (ρ_{ion}) in a colloidal suspension reduces the range of the electrostatic repulsions in a system which can lead to aggregation or phase separation [8]. The Bjerrum length is shown in Equation 1.3, where e is the elementary charge, ε_0 is the permittivity of free space, and ε_r is the dielectric constant.

$$\kappa^{-1} = (4\pi\lambda_B\rho_{ion})^{-1/2} \tag{1.2}$$

$$\lambda_B = \frac{e^2}{4\pi\varepsilon_0\varepsilon_r k_B T} \tag{1.3}$$

The DLVO theory (named after its four developers Derjaguin and Landau [17], Verwey and Overbeek [18]) combines both the attractive Van der Waals interactions, as well as electrostatic repulsions to give an energy curve similar to the one shown in Figure 1.4. From Figure 1.4 it is clear that increasing either the range or magnitude of electrostatic repulsions will increase the energy barrier that must be crossed by the system for it to irreparably aggregate, and that stronger Van der Waals attractions

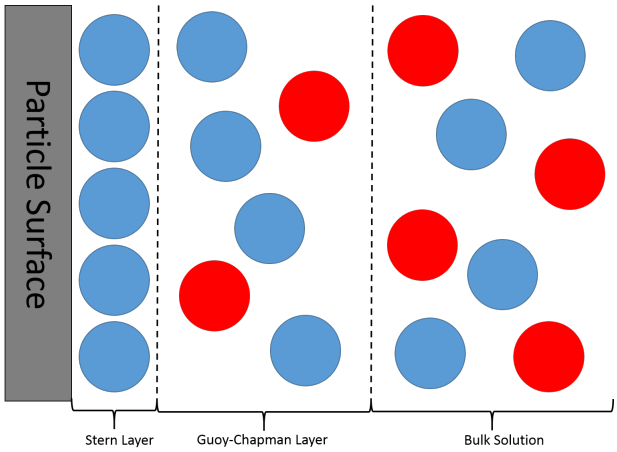

FIGURE 1.3: Diagram showing the double layer of counter-ions next to a charged particle surface

will increase the likelihood of flocculation (differentiated from aggregation by the fact that it may be re-suspended). Conversely if the electrostatic repulsions are weaker, then the energy barrier for the system to aggregate is lowered, therefore it is normally through the control of electrostatic repulsions that colloidal stability can be achieved.

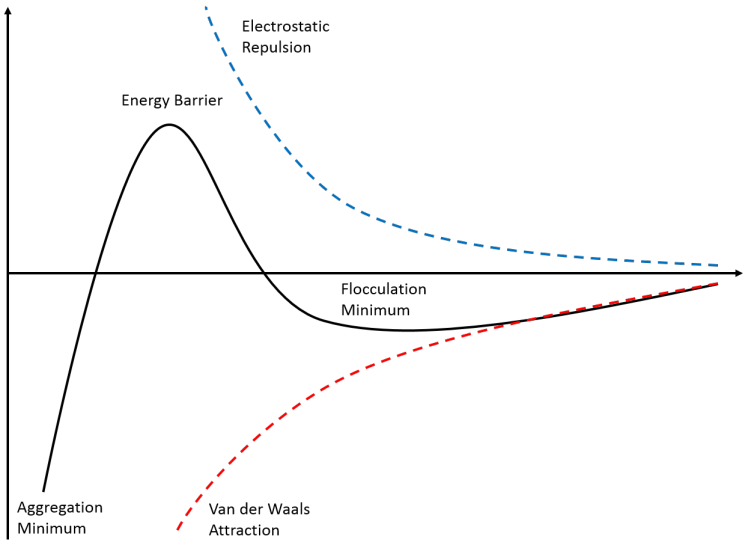

FIGURE 1.4: Energy potential for a colloidal suspension, combining both the electrostatic repulsion between colloidal particles and the Van der Waals attraction.

1.2.2 Colloid-Polymer Mixtures

When a polymer is added to a colloidal suspension, phase separation tends to occur, with a broad range of phase behaviour dependent on polymer size and concentration, as well as the surface chemistry of both colloid and polymer[10]. Phase separation

can be caused by bridging flocculation [19], in which the polymer molecule adsorbs to the surface of multiple particles, thus bridging them. This method of inducing flocculation is used widely in various industries, such as the oil industry [20], to remove suspended particles from a solution, and are referred to as either clarifying agents or de-emulsifiers.

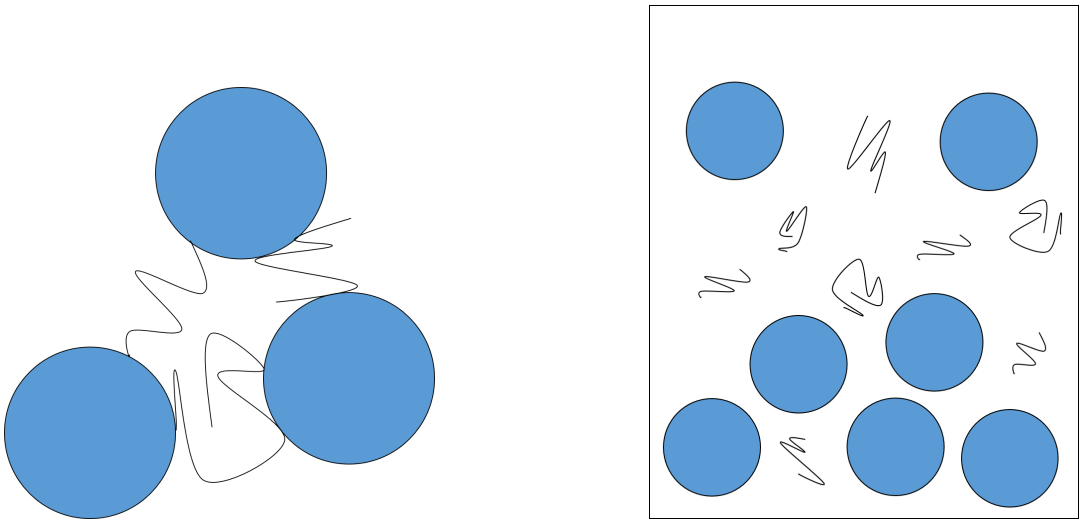

(A) Bridging (B) Depletion

FIGURE 1.5: Diagram showing the two mechanisms through which phase separation can occur when a polymer is added to a colloidal suspension.

If the polymer added to the suspension is non-adsorbing, then phase separation will still occur, but through a dramatically different mechanism, called depletion [21], an entirely physical effect. As the polymer is non-adsorbing, there is a layer around each particle which the polymer's centre of mass cannot occupy, called the depletion zone and is equal to the radius of gyration of the polymer, overlap of this depletion zone leads to an excluded volume between the particles that the polymer cannot occupy. A diagram of this is shown in Figure 1.6.

A simple way to rationalise the depletion attraction is by considering both the entropy available to the particles and by the polymer solution. In the dilute colloid limit, where there is no overlap of depletion volumes, the polymer is free to move within free volume of the system (V_f), which is the overall volume (V), minus the volume occupied by the colloids (V_c) and their depletion zone (V_{dep}).

$$V_f(dil) = V - (V_c + V_{dep}) \tag{1.4}$$

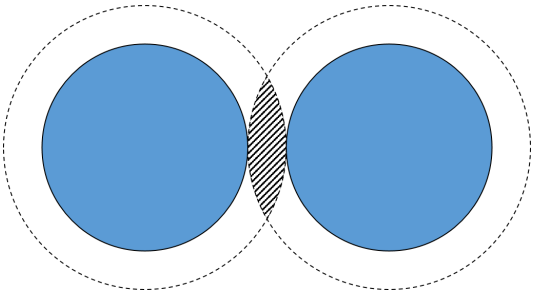

FIGURE 1.6: Diagram showing the depletion (dashed) and overlap (hatched) volumes around two colloidal particles.

Therefore, increasing the free volume will lead to increased entropy for the polymer as it has more space to occupy. Many methods can be used to change this, such as lowering the colloid volume fraction (ϕ), changing the polymer to lower V_{dep}, or diluting the entire sample to increase V. Changing these variables are what lead to the wide and varied phase behaviours found in colloid-polymer mixtures and will be further discussed below.

However, whilst the depletion zone is governed by polymer size, there is also the consideration that depletion zones can overlap, giving an excluded or overlap volume (V_{ov}) between colloidal particles. By increasing this overlap volume, you reduce the V_{dep} in the system, increase the free volume available to the polymer and thus the entropy of the polymer solution.

$$V_f(conc) = (V - (V_c + V_{dep})) + V_{ov} \tag{1.5}$$

It is this entropic driving force from depletion zones overlapping that causes the colloidal particles to come together and aggregate. Whilst the colloidal particles lose entropy by coming closer together, this is outweighed by the entropy gain for the polymer.

1.3 The Depletion Interaction

Another way to model the depletion interaction is as an imbalance of osmotic pressure exerted on the particles by the polymer solution, originally proposed by Asakura and Oosawa [21, 22]. In the Asakura Oosawa (AO) theory, the colloidal particles are considered as purely repulsive hard spheres and the polymer chains considered as

penetrable hard spheres that do not interact with one another. As they are ideal polymers, the osmotic pressure (Π_p) can be calculated from Van't Hoff's law shown in Equation 1.6, where n_b is the number density of the polymer.

$$\Pi_p = n_b k_B T \tag{1.6}$$

When two particles' depletion zones overlap this causes an excluded volume between the two particles to form, in which no polymer can occupy that space. In turn this causes a decrease in the osmotic pressure exerted on the particles.

$$U_{ov} = \begin{cases} +\infty & h \leq d \\ -\Pi_p V_{ov} & d < h \leq d + 2R_g \\ 0 & h > d + 2R_g \end{cases} \tag{1.7}$$

The attraction caused by depletion can be modelled as an attractive pair potential U_{ov} where Π_p is the osmotic pressure of the polymer, d is the particle diameter, R_g is the polymer radius of gyration, and h is the centre to centre particle separation [23]. The top line is the assumed hard sphere potential between the particles. The volume of the overlapping depletion zones between two particles at a separation h is calculated from Equation 1.8 where ξ is the ratio of the polymer radius of gyration (R_g) to the particle radius (a), R_g/a. This is commonly referred to as the colloid polymer ratio.

$$V_{ov} = \left(1 - \frac{3h}{2d(1+\xi)} + \frac{1}{2}\left[\frac{h}{d(1+\xi)}\right]^3\right) \frac{\pi}{6} d^3 (1+\xi)^3 \tag{1.8}$$

The depletion potential is entirely governed by the osmotic pressure of the polymer solution Π_p and the volume of overlap between the two depletion zones around the particles. A larger V_{ov} will require a larger depletion thickness around the particles, which is determined by the ratio of the polymer radius of gyration and the particle radius R_g/a.

1.3.1 In the Semi-dilute Regime

Whilst at low polymer concentrations the range of the depletion interaction is the same as the size of the polymer R_g, above the concentration at which individual polymer chains begin to overlap this is no longer the case. The concentration at which the polymer chains begin to overlap is dubbed the overlap concentration C_p^* and is shown in Equation 1.9.

$$C_p^* = \frac{3M_w}{4\pi R_g^3 N_A} \tag{1.9}$$

Where M_w is the molecular weight of the polymer, R_g the polymer radius of gyration, and N_A is Avogadro's constant.

The strength of the depletion potential is quoted as its strength at contact (U_0 or sometimes U_c) in units of k_BT, shown in Equation 1.10. This captures the dependence on not only the range of the attraction, but also the polymer concentration, in determining the strength of a pair potential between two colloid particles due to depletion [24]. Where q_s is the relative range calculated from Equation 1.11, where y is the reduced polymer concentration $y = C_p/C_p^*$, and the de Gennes exponent γ is 0.77 for excluded volume chains in a good solvent [25], and q_R is the size ratio of the polymer and particle radius R_g/a.

$$\frac{-U_0}{k_BT} = q_s^2 \left(q_s + \frac{3}{2}\right) q_R^{-3} y(1 + 3.77y^{1.31}) \tag{1.10}$$

$$q_s = 0.865 q_R^{0.88}(1 + 3.95y^{2\gamma})^{-0.44} \tag{1.11}$$

The depletion thickness around sphere of radius a can also be approximated, using the following power laws for a Θ solvent and good solvent respectively [10, 24]. Where ϕ_p is the relative polymer concentration.

$$\frac{\delta_s}{a} = 0.938 \left(q_R^{-2} + 6.02 q_R^{-2} \phi_p^2\right)^{-0.45} \tag{1.12}$$

$$\frac{\delta_s}{a} = 0.865 \left(q_R^{-2} + 3.95 q_R^{-2} \phi_p^{1.54}\right)^{-0.44} \tag{1.13}$$

With many models and estimations for calculating the strength and range of the depletion potential, and in some cases whether a depletion attraction is even present, available in the literature, there are still limitations to directly measure the depletion attraction in colloidal systems, which we will discuss below.

1.3.2 Measuring the Depletion Potential

The presence and magnitude of a depletion potential has been measured by Tuinier et al. [26] using a combination of Small Angle Neutron Scattering (SANS), light transmission measurements and Dynamic Light Scattering (DLS). Further to this, Milling et al. [27] use Atomic Force Microscopy (AFM) to measure the depletion potential between 3.8 μm silica particles with a short ranged depletion attraction of around 20 nm. Total Internal Reflection Microscopy (TIRM) can also be used to measure the depletion attraction between a wall and a colloidal particle, with either a polymer depletant to give an attraction [28], or where the particle is depleted from the surface giving a repulsion [29]. Optical tweezers can also be used to measure the depletion potential between colloidal particles [30], however due to constraints of tracking the colloidal particles this has only been performed using large molecules such as DNA as a depletant [31].

The main challenges faced when measuring the depletion potential directly appear to be predominantly technique resolution, with AFM only able to measure extremely short-range depletion attractions, and optical tweezers only having sufficient resolution to measure extremely long range depletion potentials. However due to recent techniques allowing the particles to be resolved at very close separations, optical tweezers could be a powerful method in measuring the depletion potential of industrially relevant polymers such as xanthan or Hydroxyethylcellulose (HEC) derivatives. Furthermore, AFM and TIRM measure depletion against a wall, which does not allow the measurement in situ of a system. So, results would need to be converted from the particle-wall attraction measured, to a particle-particle attraction.

1.4 Phase Behaviour

The phase behaviour of colloid-polymer mixtures is rich and varied with many equilibrium and non-equilibrium states having been observed [23, 32, 33]. At low polymer concentrations a single phase colloidal fluid is formed. Above a critical concentration of polymer, the depletion interaction is sufficient to drive phase separation, and a colloid-rich (liquid) phase and colloid-poor (gas) phase is formed, this critical concentration is lowered as colloid volume fraction (ϕ) is increased. At higher polymer concentrations and colloid volume fractions a crystalline phase is formed along with a gas phase, with triple points and co-existence areas being predicted and observed [32, 34]. In each of these phase transitions the two phases are in thermodynamic equilibrium with one another, and at the triple point, three phases.

An example of non-equilibrium phase behaviour is gelation, where phase separation becomes arrested, in this case, the phase separation dynamics are either halted or slow significantly. This leaves the sample thermodynamically unstable, whilst appearing metastable when viewed by eye. Gelation is usually observed when a system is quenched deep into the gas and crystal phase, as the crystal phase has sufficient volume fraction and depletion attraction that it forms a space-spanning network throughout the system, allowing it to support its own weight.

As it is the favourable overlap of depletion zones that drives this phase separation, the polymer size (R_g) relative to the colloid size (a) is an important factor in predicting the phase behaviour of a colloid-polymer mixture.

The Free Volume Theory (FVT) developed by Lekkerkerker et al. [32] accurately predicts the phase behaviour of colloid-polymer mixtures at different colloid volume fractions and polymer concentrations. The free volume (α) available to the polymer solution is shown in Equation 1.14, allowing the polymer concentration to be stated as $c_p^{tot} = \alpha c_p$.

$$\alpha = (1-\phi)\exp(-Af - Bf^2 - Cf^3) \tag{1.14}$$

Where ϕ is volume fraction and:

$$f = \phi/(1-\phi) \tag{1.15}$$

With the coefficients:

$$A = (1 + q_s)^3 - 1 \tag{1.16}$$

$$B = 3q_s^3(q_s + 3/2) \tag{1.17}$$

$$C = 3q_s^3 \tag{1.18}$$

Where q_s is δ_s/a, the relative depletion range.

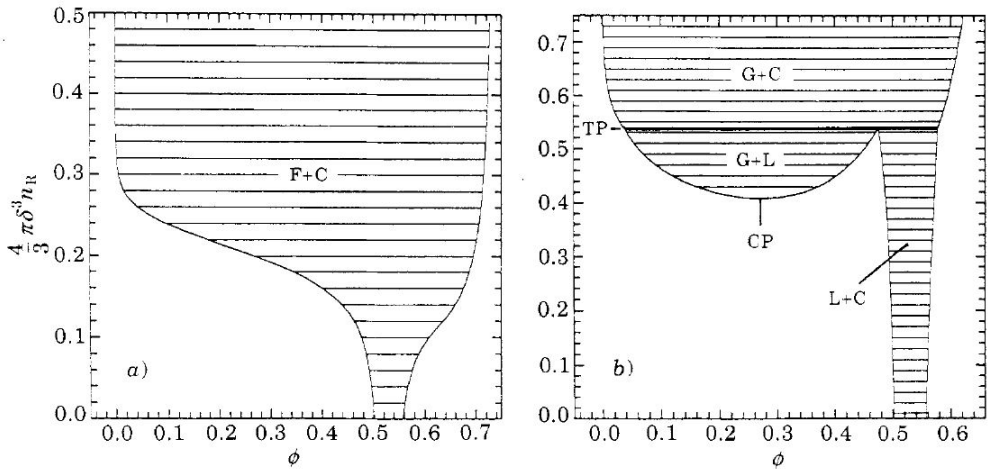

FIGURE 1.7: Phase Diagrams of colloid-polymer mixtures of colloid volume fraction (ϕ) and dimensionless polymer concentration, for size ratios 0.1 (left) and 0.4 (right). Reproduced from [32].

Figure 1.7 shows phase diagrams generated by Lekkerkerker et al. [32] using FVT for colloid-polymer ratios of 0.1 and 0.4. Increasing the colloid-polymer ratio gives rise to more complex phase behaviour, with the emergence of gas + liquid, liquid + crystal, and gas + crystal phases.

Fleer and Tuinier [24] build upon Free Volume Theory by incorporating the shrinking of the depletion zone in the semi-dilute polymer regime. The depletion range crosses over from being of order R_g in the dilute regime to of order the blob size ξ. The depletion range in this crossover between the dilute and semi-dilute regimes is shown in Equation 1.11.

1.4.1 The Effect of Temperature on Phase Behaviour

The effect of temperature on colloid-polymer mixtures has only been sparsely studied, presumably due to the fact that increasing polymer concentration in a phase diagram has been made analogous to reducing temperature [25, 35, 36], as well as used as a parameter in the simulation of gelation in colloidal suspensions.

Taylor et al. [37] explore the effect of temperature on a system of PMMA particles ($a = 540$ nm) and polystyrene ($M_w = 8.5$ x 10^6) in cis-decalin. Giving a θ temperature of 10 °C and a R_g^θ of 95 nm, and a colloid-polymer ratio equalling 0.176.

For the effect of temperature on the radius of gyration of polystyrene, Taylor et al. [37] proposed Equation 1.19 which was fitted to experimental data obtained by Berry [38].

$$R_g(T) = R_g^\theta \left[\sqrt{2} \left(1 - \exp\left(\frac{T_\theta - T}{\tau} \right) \right) + 1 \right] \tag{1.19}$$

Where τ is 20°C, T_θ is the temperature at which the solvent becomes a θ - solvent, and $R_g\theta$ being the unperturbed radius of gyration. The expansion of the radius of gyration is due to the crossover from a poor solvent to a good solvent, causing the polymer to swell.

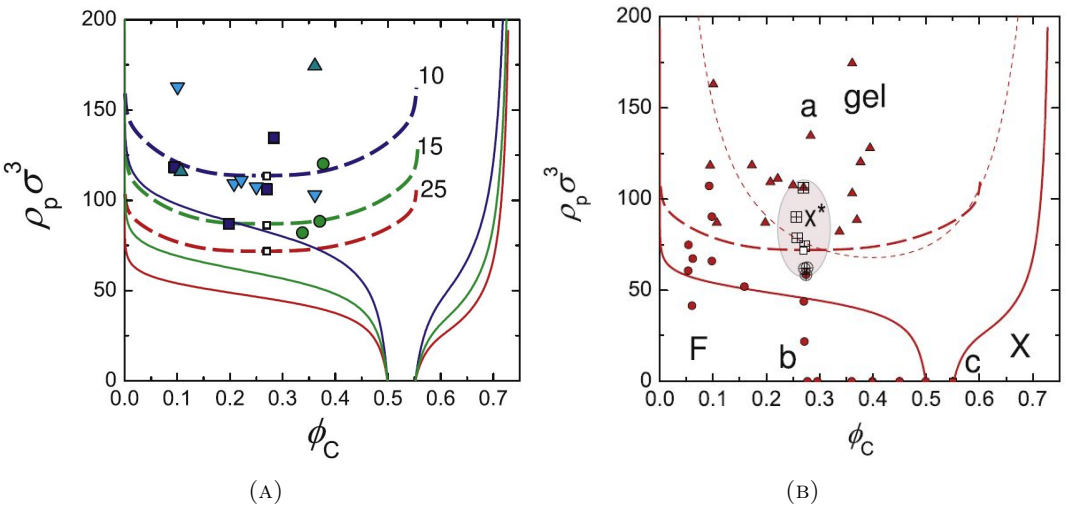

(A) (B)

FIGURE 1.8: Phase diagrams for a mixture of PMMA and polystyrene, (A) showing the effect of temperature on phase boundaries, and (B) comparing experimental observations and AO theory. Both reproduced from [37].

Poon et al. [39] explore the effect of temperature on a colloid-polymer mixture at

$\phi = 0.2$ using a system consisting of PMMA particles ($a = 217$ nm) and polystyrene ($R_g = 12.8$ nm) in cis-decalin, giving a colloid-polymer ratio of 0.06. They study between 8 °C and 28 °C with the θ temperature of polystyrene in decalin being 12.5 °C. Figure 1.9 shows the phase diagram of this system at room temperature observed visually.

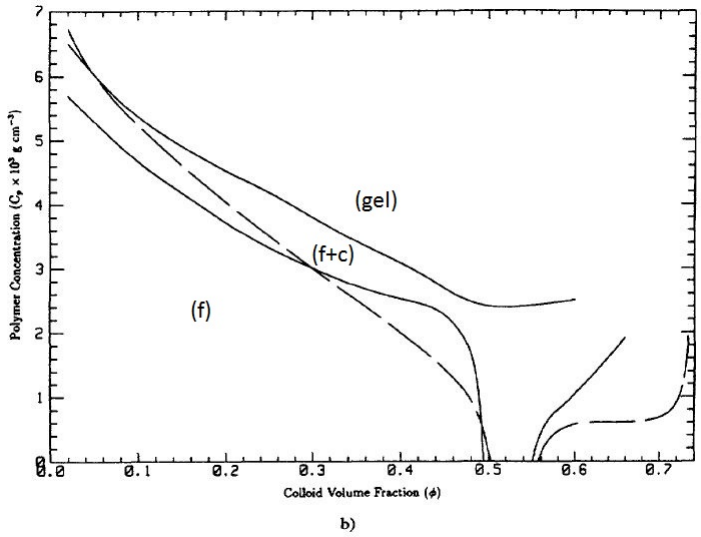

FIGURE 1.9: Phase Diagram comparing experimental observations (solid lines) and free volume theory of Lekkerkerker (dashed lines) [32]. Reproduced from [39].

Figure 1.10 shows the effect of temperature on the phase boundaries in the system, with the main effect being that increasing temperature reduces the amount of polymer required to observe fluid-crystal coexistence. This decrease is attributed to firstly, the polymer coils expanding and thus increasing the range of the depletion interaction (δ) and secondly, that osmotic pressure (Π_p) exerted by the polymer increases with temperature.

Whilst the work on the effect of temperature is indeed limited, the studies of Taylor and Poon find that any change in the phase behaviour of colloid polymer mixtures due to temperature is caused by the expansion or contraction of the polymer used. It would appear that the effect of temperature on the phase boundaries lessens as temperature is further increased (shown in Figure 1.10). Therefore, if a system can be accurately characterised at different temperatures, any change in the phase diagram can be mapped.

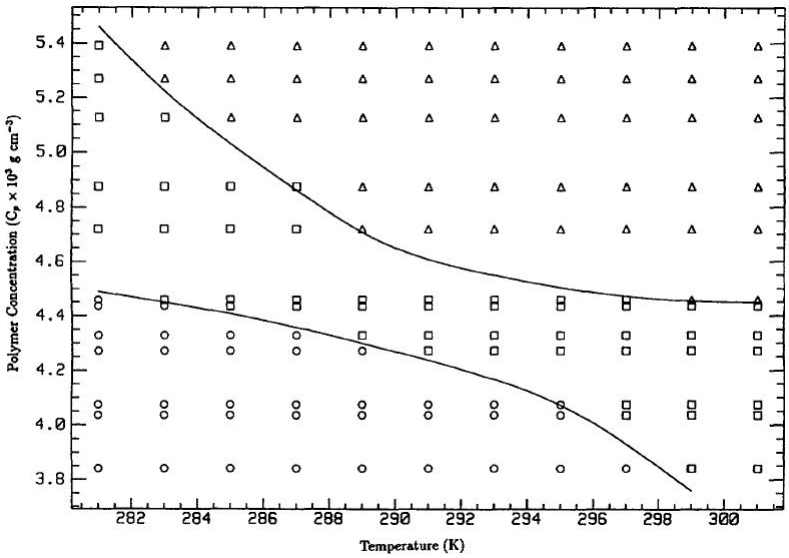

FIGURE 1.10: The effect of temperature on the fluid (circles), fluid and crystal (squares), and gel (triangles) phase boundaries. Reproduced from [39].

1.5 Dynamics in a Depletion System

Understanding the diffusion of colloidal particles through a polymer solution is an area of great interest, especially when concerned with non-adsorbing polymers and depletion based systems. The Brownian motion of a free particle can be calculated from when the Mean Squared Displacement (MSD) $\langle r^2 \rangle$ grows linearly with time. It is dependent on the time (t) and the diffusion coefficient D_0. Equation 1.20 shows the relationship between the MSD and D_0 in three dimensions. The Stokes-Einstein equation (Equation 1.21) relates the diffusion constant D_0 to the radius of a particle a, and the viscosity of the medium it moves through η. The Brownian relaxation time (τ_B), is the time taken for the particle to diffuse its own radius, and is shown in Equation 1.22, where η_0 is the solvent viscosity, and a the particle radius.

$$\langle r^2 \rangle = 6D_0 t \tag{1.20}$$

$$D_0 = \frac{k_B T}{6\pi\eta a} \tag{1.21}$$

$$\tau_B = \frac{6\pi\eta_0 a^3}{k_B T} \tag{1.22}$$

However, when a particle moves through a polymer solution it 'senses' the non-uniform viscosity of the fluid, which results in the particle not being affected by the solvent viscosity or the polymer viscosity entirely, but an effective viscosity, the value of which lies between the two [40]. Figure 1.11 compares experimental data and two-layer model results for various depletion ranges and polymer concentrations, with the two-layer model (discussed below) appearing to breakdown at high polymer concentrations and for longer range depletion attractions.

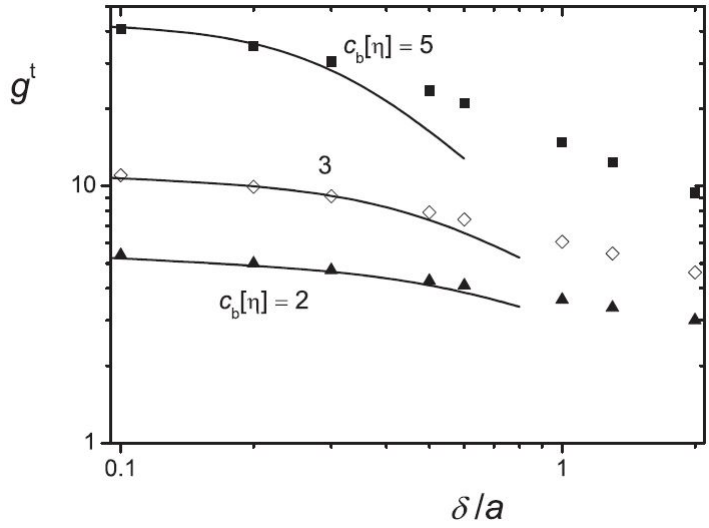

FIGURE 1.11: Correction function to the translational friction coefficient as a function of relative depletion thickness for three polymer concentrations. Data points from [41] and solid lines follow the analytical two-layer results from [42]. Reproduced from [40].

Fan et al. [42] have modelled the motion of a particle through a polymer solution and find that a two-layer approach is appropriate when considering particle dynamics. The first layer is the depletion zone around the particle, in which the particle experiences solvent viscosity (as the polymer is depleted from the particle surface). After this layer, the particle experiences the bulk polymer viscosity. However, as the range of the depletion zone increases (δ/a) the two layer approximation does begin to deviate from analytical results.

Figure 1.12 shows the reciprocal of the translational correction factor (g^t) plotted against dimensionless depletion thickness d ($d = \delta/a$). The correction factor g^t is shown in Equation 1.23 and related to the solvent viscosity η_0 and the effective viscosity experienced by the particle η_{eff}, with η_{eff} being between the solvent η_0 and

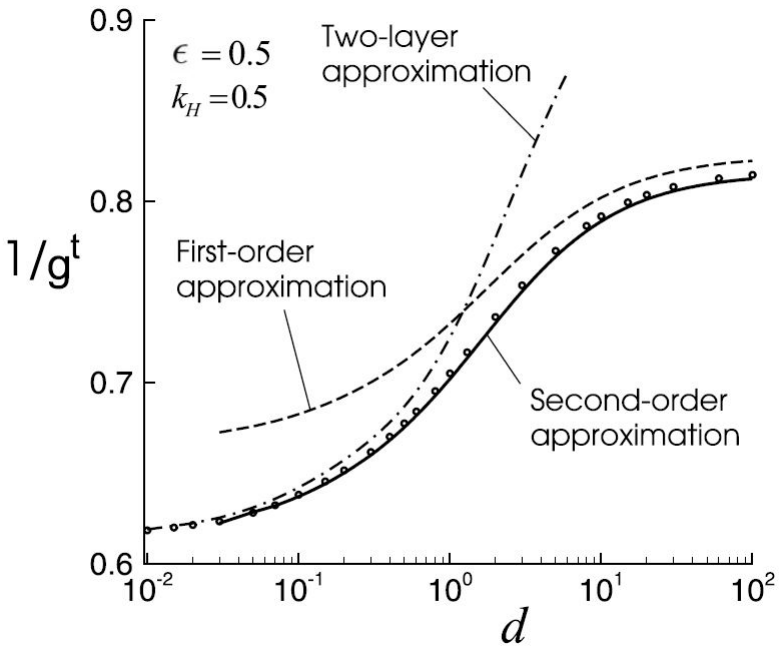

FIGURE 1.12: Comparison of the two-layer approximation to asymptotic first and second order solutions for the correction function g^t. Two layer results from [42]. Reproduced from [41].

polymer η_L viscosities.

Comparing a first order approximation and second order approximation, shows that the first order over-estimates slightly at large depletion thicknesses and diverges as depletion range decreases. The second order approximation fits across all depletion ranges shown. The two-layer approximation from [42] is also compared, and fits well at low depletion thicknesses and begins to diverge at $d \approx 0.8$.

$$\eta_{eff} = \eta_0 g^t \tag{1.23}$$

$$\eta_0 < \eta_{eff} < \eta_L \tag{1.24}$$

Figure 1.13 shows the depletion zones around two particles (with a range of $d = 1$) with viscosity gradients around each particle that then merge as the depletion zone around each particle overlap. The bulk viscosity outside of these depletion zones is given as $\approx$ 100 times the solvent viscosity. The first contour around each particle is two times the solvent viscosity, a dramatic decrease from the bulk viscosity. This shows how the two-layer model differs at high depletion ranges, as there appears to be

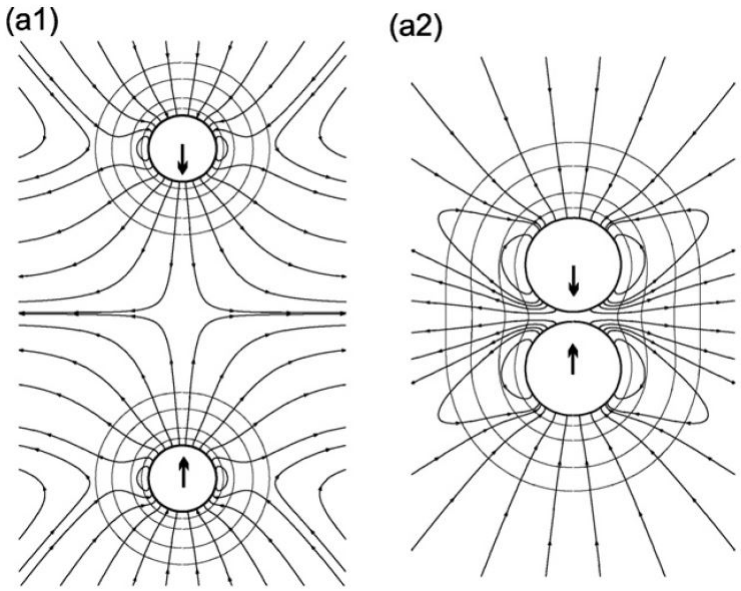

FIGURE 1.13: Flow patterns with the depletion effect present ($d = 1$), at two separation distances. Viscosity contours are 2, 10, 50, and 80 times the solvent viscosity, with the bulk viscosity value being 100 times the solvent viscosity. Reproduced from [43].

a gradual transition from η_0 to η_L in Figure 1.13 not the jump from η_0 to η_L assumed in the two-layer model.

Even from this brief overview, it is clear to see that understanding the dynamics in a depletion system has significant complications. Whilst assumptions and simplifications for certain parameters are available, accurate models require a significant degree of complexity and effort to implement.

1.6 Colloid-Polymer Gels

Under the correct conditions, gels will form when a space-spanning network of colloidal particles is created, either due to chemical bonding or physical bonding [44]. An example of the formation of a chemical gel is the curing of resins, such as epoxy [45]. Gels are often defined as having solid-like behaviour and properties, such as a yield stress. Rheologically, a gel is defined as having a larger elastic modulus (G') than viscous modulus (G''), signifying that the sample primarily has solid-like behaviour.

Common colloid systems used include: an emulsion of PDMS drops in 1,2-ethanediol (ED) and water [46], PMMA particles suspended in decalin [47], silica spheres dispersed in hexadecane [48, 49] or water [50].

1.6.1 Position on Phase Diagram

Figures 1.14 and 1.15 show state diagrams for colloid-polymer mixtures for short and long colloid-polymer ratios, defined as < 0.3 and > 0.3 respectively. These state diagrams include both the equilibrium phases (such as stable fluids or gas + liquid phases), and non-equilibrium states such as gels and glasses.

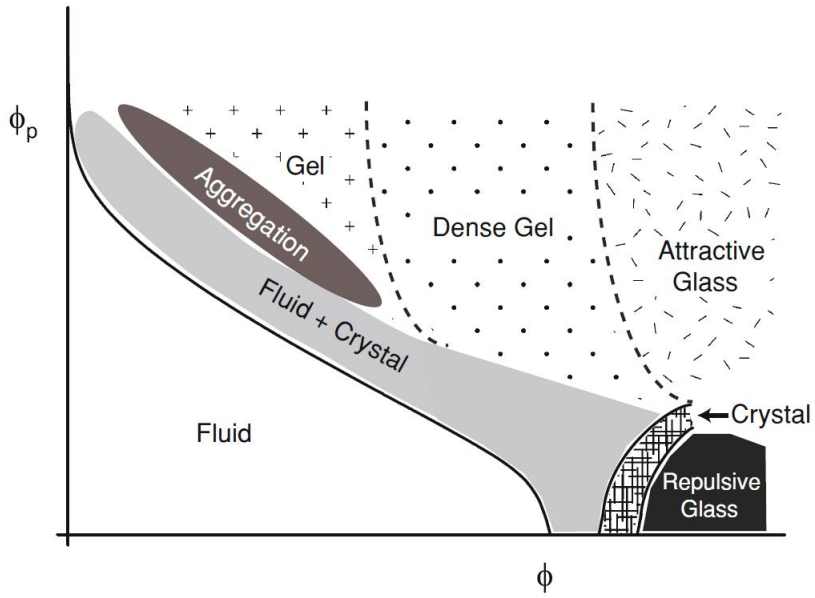

FIGURE 1.14: State diagram for colloid-polymer mixtures with a short colloid-polymer ratio (< 0.3). Reproduced from [10].

In both cases gels appear at low to moderate colloid volume fractions, and at moderate to high polymer concentrations. As colloid volume fraction is lowered, the amount of polymer required for a gel to form is increased, and as colloid volume fraction is increased, a gel will form at lower polymer concentrations. In the case of a short-range depletion attraction, more states are observed at high colloid volume fraction. With very little polymer, a repulsive glass is formed, where little to no attraction is present but a particle cannot escape the cage of particles surrounding it due to the high volume fraction. With the addition of more polymer, attractions begin to form between particles causing them to cluster and holes to form within the gel network, giving a metastable fluid. With further addition of polymer an attractive glass is formed where the attraction is strong enough that particles are tightly bound in cages of surrounding particles with no possible escape.

For $q < 0.3$, at lower volume fractions the addition of polymer causes aggregation

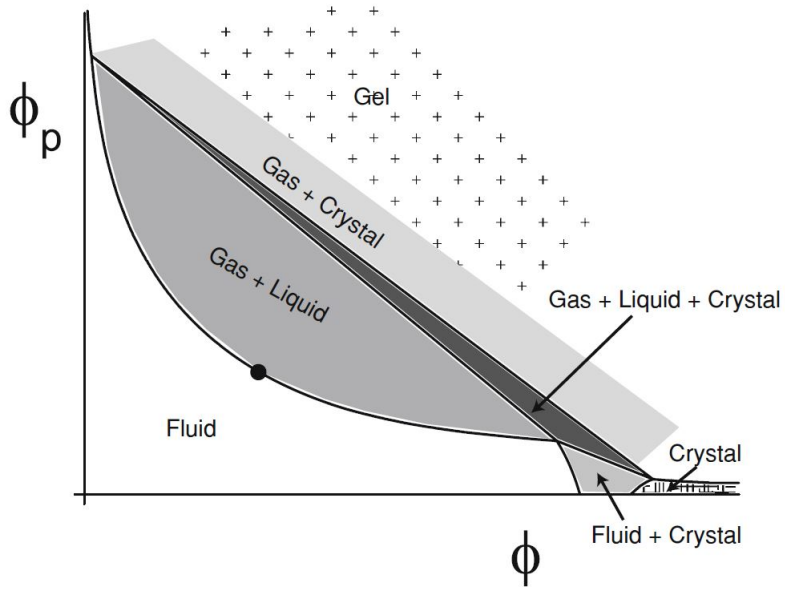

FIGURE 1.15: State diagram for colloid-polymer mixtures with a large colloid-polymer ratio (> 0.3). Reproduced from [10].

as there is sufficient attraction for particles to come together but there are not sufficient particles to form a space-spanning network. When there is sufficient volume fraction for a network to arrest phase separation, a gel is formed.

1.6.2 Weak and Strong Gels

Colloidal gels can be broken down into two main categories, the first being weak gels with interactions $U_0/k_BT < 10$ meaning that bonds formed within the gel structure are relatively weak and short lived. The second category of gel is a strong gel ($U_0/k_BT \gg 10$) in which the bonds formed in the particle network are strong and long lived and hence considered permanent.

Strong gels tend to exhibit creeping sedimentation, in which fractures begin to form in the gel, allowing the fluid trapped within it to flow [52]. Early fluid flow (before fractures form) associated with strong gel collapse can be related to the pressure gradient along the gel by using Darcy's Law [53], where the $\kappa(\phi)$ is the permeability of the network, v is the velocity of the interface, and p the fluid pressure.

$$v = -\frac{\kappa(\phi)}{\eta}\frac{\partial p}{\partial z} \tag{1.25}$$

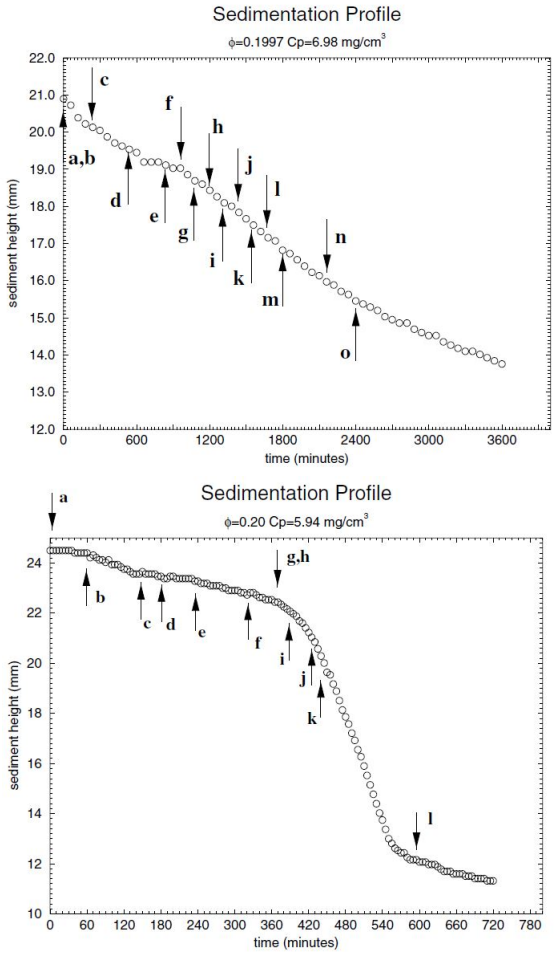

FIGURE 1.16: Two sedimentation profiles obtained through dark-field imaging showing creeping sedimentation (Top) and delayed collapse (Bottom). Reproduced from [51].

$$\kappa(\phi) = \kappa_0 \left[\frac{\phi_0}{\phi(z,t)}\right]^{\frac{2}{3-d_f}} \tag{1.26}$$

Where υ is the velocity of the interface, p is the fluid pressure, k_0 is the initial permeability of the network, ϕ_0 is the initial volume fraction, and d_f is the fractal dimension.

One of the main driving forces behind gel collapse is that colloidal particles are prone to sedimentation/creaming due to Stokes law where a particle settles under gravity with a Stokes velocity υ_0, where a is the particle radius, ρ_p the particle density, ρ_s the density of the solvent, g the acceleration due to gravity and η_0 the viscosity of the solvent [54].

$$\upsilon_0 = \frac{2}{9}\frac{(\rho_p - \rho_s)ga^2}{\eta_0} \tag{1.27}$$

Weak gels tend to be metastable for a finite time, defined as the delay time τ_d, before the gel undergoes a rapid collapse [51] and either sediments, or phase separates into a colloid rich and a colloid poor region [32].

Figure 1.16 shows two height profiles in which creeping sedimentation (top) is observed at a higher polymer concentration and delayed collapse (bottom) is observed at a slightly lower concentration. Creeping collapse manifests in a drastically different way and if an industrial formulation was to collapse in this way, then determining a shelf-life may be difficult. Whereas with delayed collapse there is the delay time that can be determined as the shelf-life. Starrs et al. [51] determine that the crossover from delayed to creeping collapse is caused by the increase in depletion potential arising from the higher polymer concentration and can also be induced by drastically changing the dimensions of the sample container.

The delay time before collapse (τ_d) has been found to depend on a wide variety of parameters, Gopalakrishnan et al. [55] find that increasing the colloid volume fraction (θ) increases the delay time, whilst also decreasing the initial settling velocity of the gels. This change in initial settling velocity is attributed to the permeability of the network through which solvent up-flow can occur, with τ_d being the change in settling velocity observed similar to that in Figure 1.16, this is thus due to a change in network permeability.

1.6.3 Gel Structure

For a gel to form, a space-spanning network must be formed that has sufficient strength to resist the gravitational stress applied to the system. However, the particles making up the network are not stationary. Previous work has shown that the network of weak colloidal gels is continuously rearranging and coarsens with time [56–58] leading to thicker strands of particles forming the space-spanning network. Figure 1.17 shows how strand thickness and pore size increase with time as the network coarsens. This coarsening is driven by thermal fluctuations within the gel and because the attractions within the gel are of order k_BT. As the gel structure coarsens and the strands thicken, the pores between the strands of particles within the gel increase. This increase in pore size allows for larger amounts of the continuous phase

to move if there is a failure of one of the strands, eventually this leads to the macroscopic collapse of the gel. This coarsening is driven by gradual rearrangement of the particles within the gel network, quantified by the Kramer's escape time shown in Equation 1.29, therefore any change in the Kramer's escape time would affect the rate of coarsening within a gel.

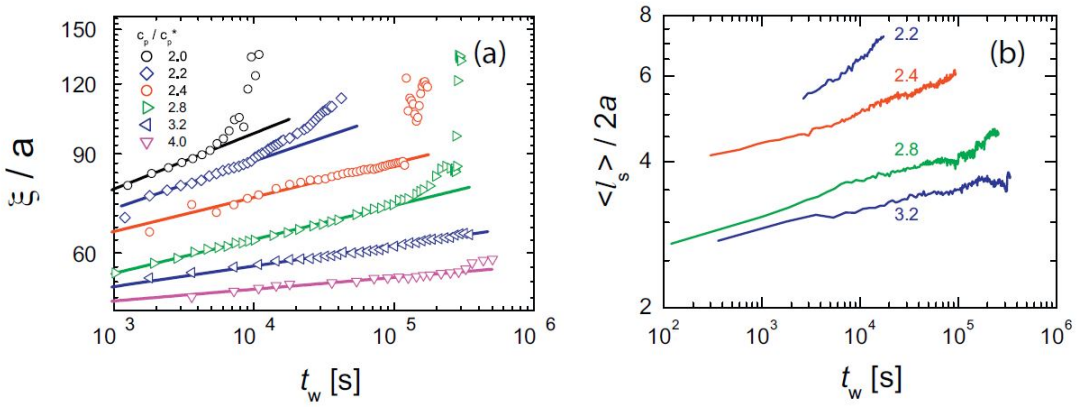

FIGURE 1.17: Time evolution of pore size ξ and strand thickness l_s at different polymer concentrations. Reproduced from [56].

1.6.4 Structural Evolution

Zia et al. [59] have proposed a differing mechanism of gel coarsening, in which particles on the outside of a strand that have a lower contact number, migrate through diffusive steps (caused by thermal fluctuations within the sample) to form thicker strands, thus causing the particles to have a higher contact number and become caged. Coarsening was seen as the probability of a particle contact number gradually increased as the gel aged, snapshots of two gels with differing attraction strengths can be see in Figure 1.18, here it can be easily seen that the gels coarsened at differing rates, due to the difference in the depth of attractive well for each gel. Zia et al. comment that whilst bond kinetics play a clear role in the rate of gel coarsening, they are not the only factor controlling the rate of coarsening within a colloidal gel, this suggested that a simple single-bond model may not be enough to fully capture the process in which gels age and eventually fail.

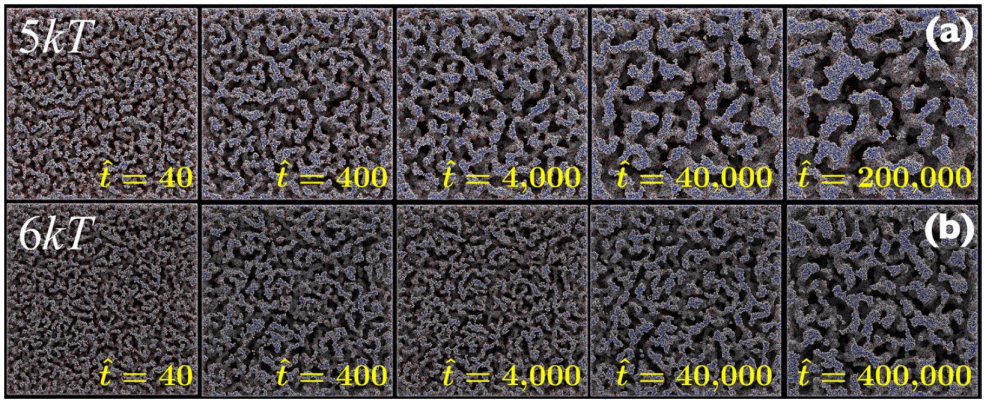

FIGURE 1.18: Evolution of particle strands for two gels with different depletion potentials. Reproduced from [59].

1.6.5 Accelerated Strand Ageing

Sprakel et al. [60] have explored the stress dependence of delayed collapse in a wide variety of gel systems, including strong gels of 8 wt% carbon black, thermoreversible gels of stearylated silica, pNIPAm-grafted colloids ($\theta = 0.075$) and depletion gels of polystyrene colloids and dextran ($\theta = 0.3$, $c_p = 50$ mg/ml). They found two distinct collapse regimes which are fitted by Equation 1.28, with the two regimes described as when the rate of strand disassociation k'_D is significantly lower than the rate of strand association k_A, and when the rate of strand association k_A is much lower than the rate of strand disassociation k'_D, with the first regime found at high applied stress and the second found at low applied stress, this is seen in Figure 1.19b. Figure 1.19a shows thermoreversible gels of stearylated silica with a differing amount of pre-shear applied. As the amount of pre-shear applied was increased the delay time for the gel decreased at a faster rate and the transition from one regime to another became more distinct. Also shown in Figure 1.19a is a normal distribution of delay times for the same pre-shear and volume fraction, indicating that macroscopic gel collapse is a stochastic event due to the rupture of multiple particle strands at once.

$$T_d \approx \left\{ \begin{array}{ll} \dfrac{1}{n^2 \sigma C k_A} \left(\dfrac{k_A}{k_D} \right)^n e^{-n\sigma C}, & k'_D \ll k_A \\ \dfrac{S_n}{\sigma C k_D} e^{-\sigma C}, & k'_D \gg k_A \end{array} \right\} \tag{1.28}$$

Where C $= \delta / n \rho_0 k_B T$ in units of compliance, σC is the elastic energy per bond at yield, n is the number of bonds in the strand, and S_n is the strand survival probability.

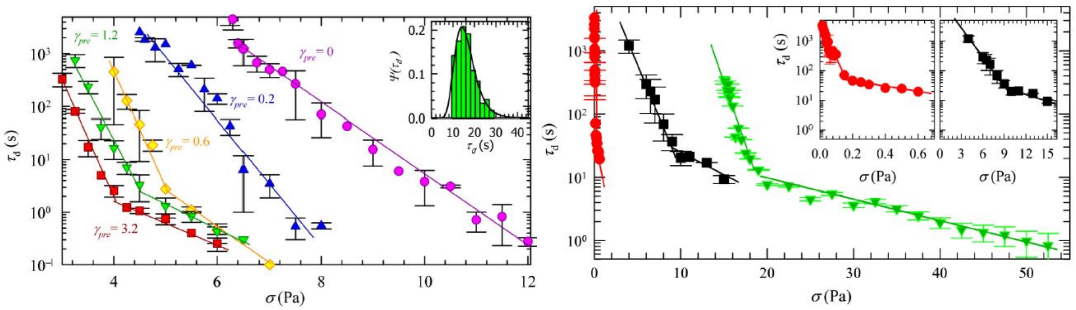

(A) Thermoreversible stearylated silica gels, with inset showing the distribution of delay times at $\theta = 0.25$ and $\sigma = 8$ Pa.

(B) Delay times for the 3 gel systems described above.

FIGURE 1.19: Delay times of various colloidal gels at a range of shear rates. Both graphs reproduced from [60].

1.6.6 Microscopic Dynamics

Linking long time-scales to short time-scales has clear merit in understanding the long-term stability of formulations. The ability to measure or calculate a short time-scale which can then be scaled up to give an indication of stability, allows for formulations to be more intelligently designed.

Previous work [33, 46, 54, 55, 61] linking the microscopic dynamics of a gel and its delayed collapse has used the Kramer's escape time (τ_{esc}) which is described as the average lifetime of an individual particle bond before it breaks due to thermal fluctuations within a gel, and is shown below in Equation 1.29 [61].

$$\tau_{esc} = \frac{\delta^2}{D_t} \frac{\exp(-U_0/k_BT) - (1 - U_0/k_BT)}{(U_0/k_BT)^2} \tag{1.29}$$

Where δ^2 is the range of the depletion potential calculated from the linear equation of Fleer et al. [24] shown in Equation 1.34. U_0/k_BT is the depletion potential at contact in units of k_BT, calculated from Equation 1.10. D_t is the translational diffusion constant, which is estimated from the short-time self-diffusion constant (D_0) of a hard sphere suspension of the same volume fraction. The limiting low shear viscosity (η_L) can be determined by extrapolating the steady-shear rheology of a polymer solution to a vanishing shear rate which is then fitted to the Martin equation shown below in Equation 1.31 [46].

$$D_0 = \frac{k_B T}{6\pi\eta_L \alpha} \tag{1.30}$$

$$\frac{\eta_L}{\eta_0} = 1 + [\eta]\, c_p \exp\left(\kappa_H\, [\eta]\, c_p\right) \tag{1.31}$$

Where η_0 is the solvent viscosity, $[\eta]$ is the intrinsic viscosity, c_p is the polymer mass concentration and where k_H is a constant that is equivalent to the Huggins constant at low polymer concentrations.

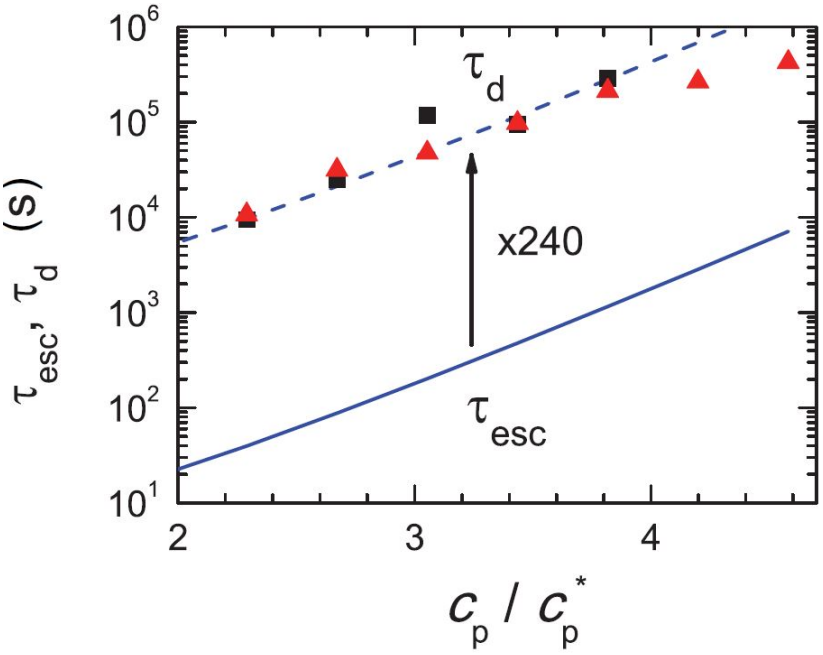

FIGURE 1.20: Graph showing the relation between Kramer's escape time and delay time. Reproduced from [46].

Figure 1.20 shows τ_d and τ_{esc} for a xanthan-PDMS gel with a size ratio R_g/a of 0.62, as a function of the reduced polymer concentration C_p/C_p^*. Here it is clear that there is a strong correlation between the lifetime of a single particle-particle bond and the lifetime of a gel on the macroscopic scale. It is also interesting that over almost two orders of magnitude, the correlation remains roughly consistent, with $\tau_d \sim 240\tau_{esc}$.

Buscall et al. [33] review a wide range of gels in which the delayed collapse phenomenon is observed, including gels of long-ranged weak attractions ($R_g/a = 0.62$, $U_0 \sim 5k_BT$) and stronger, short-ranged attractions ($R_g/a = 0.076$, $U_0 \sim 10k_BT$), as well as aqueous and non-aqueous solvents. They find that the correlation between

delay time and escape time remains consistent across all the gels studied, with the delay times normalised by the diffusion time $\tau_0 = 5\pi R\mu/k_BT$ a master curve is produced against mean binding energy θ ($\theta =< z > U_m/k_BT$) showing that even in drastically different systems, a similar shift factor is observed to link escape time and gel lifetime, furthermore, the shift factor scales with relative polymer size R_g/a.

The Kramer's escape time is determined by the well depth of the depletion attraction, the range of the depletion attraction and the diffusion of the particles within the gel. Of all the factors contributing to the diffusion of a particle, the viscosity, is the most sensitive to any change in temperature, as the size of the particles and thus the depletion potential will change minimally if at all. Therefore, to fully understand how the Kramer's escape time and thus the rate of coarsening inside a gel is affected by temperature, the temperature dependence of viscosity must be accounted for.

1.6.7 A System of Jammed Particles

One way of rationalising the dynamics of a gel is that of a "jammed" phase transition, in which the strands of the gel network are of sufficient volume fraction with sufficient attraction for their dynamics to become arrested [62]. This high volume fraction in the gel network has been observed previously using confocal microscopy [56], and even low volume fraction gels of $\theta = 0.2$ can have strands of $\theta \sim 0.6$. In many colloidal systems, this out of equilibrium gel comes about through spinodal decomposition [25, 62–64].

Colloidal glasses form at higher volume fraction than gels, with the volume fraction at which a colloidal suspension becomes a glass being called the glass transition. This glass transition is accompanied by a change in the rheological properties of the suspension, usually a change from a viscous fluid to a viscoelastic solid [65]. The relaxation dynamics of a colloidal glass are also significantly slower for a glass than a gel, as diffusive motion is limited by particles forming cages that require cooperative movement to break and allow the structure to relax [66].

As previously stated, whether a system is jammed or not is dependent on the volume fraction and attraction between the colloid particles, however these are not exclusively the factors that control jamming, another important parameter to be considered is applied stress (or strain). As you would expect, applying a stress to

a system suppresses jamming (much akin to how if something is a bit stuck you give it a good shove), this can be seen in the phase diagram made by Trappe et al. [67] in which the jammed regime (yellow) is heavily suppressed by increased stress (σ/σ_0) unless there is a very high volume fraction of colloids for the system to be able to transmit this stress throughout the system without the particles relaxing from a glassy state to a crystalline state.

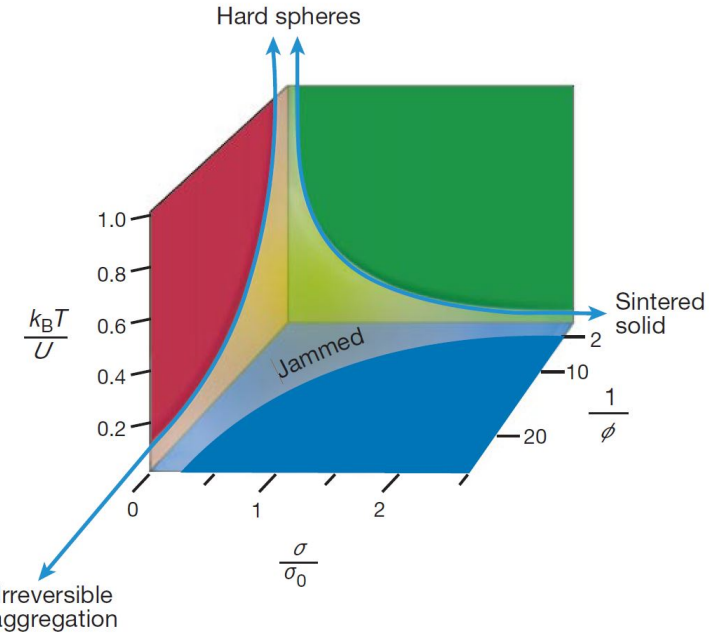

FIGURE 1.21: Composite phase diagram of attractive colloidal particles, showing the jammed phase in yellow, the axes are interaction strength (k_BT/U), applied stress (σ/σ_0) and reciprocal colloid volume fraction ($1/\phi$). Constructed using data from three different colloid systems, carbon black, PMMA, and polystyrene. Reproduced from [67].

Liu and Nagel [68] propose a phase diagram similar to that of Trappe et al. [67] with the major difference being the change of the z axis label to temperature, and the shape of the jammed region being convex rather than concave. From this phase diagram, the effect of increasing temperature is to reduce the level of jamming within the system, eventually completely unjamming the system and a colloidal liquid forming. The temperature vs load axes raise the interesting question of whether an increase in temperature will lower the yield stress of a material, which may cause the acceleration of delayed collapse, or if the reduction is significant enough that the yield stress is below the gravitational stress, a change to creeping sedimentation. With increasing attraction strength in colloidal systems being considered as lowering

the temperature, it remains to be seen whether the potential axis on Figure 1.21 is interchangeable with the temperature axis of Figure 1.22.

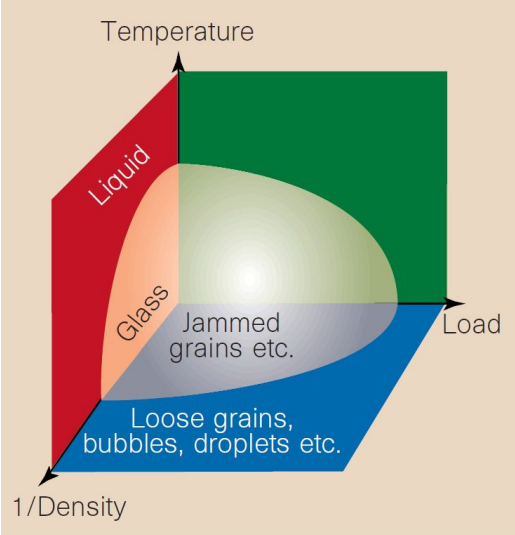

FIGURE 1.22: Suggested phase diagram for jamming as a function of temperature, density and load. Reproduced from [68].

1.7 Polymer Solutions

In this section we will discuss the fundamental behaviours of polymer solutions, such as concentration regimes, and the effects of solvency. We will then summarise the wide range of literature on the specific behaviours of the polysaccharide xanthan, including its interesting conformation behaviour.

1.7.1 General Polymer Solutions

When the polymer concentration is low enough that the polymer coils do not interact with each other, it is defined as a dilute solution, when the polymer coils touch the solution is defined as semi-dilute and when the coils interpenetrate the solution is defined as concentrated. The concentration at which a polymer polymer solution is defined as semi-dilute is the polymer overlap concentration, C_p^*.

As the radius of gyration is defined by both the thermodynamic properties and the conformation of a polymer, any change in temperature is likely to affect the radius of gyration, especially if the polymer temperature is taken above the characteristic melting point t_m for that polymer.

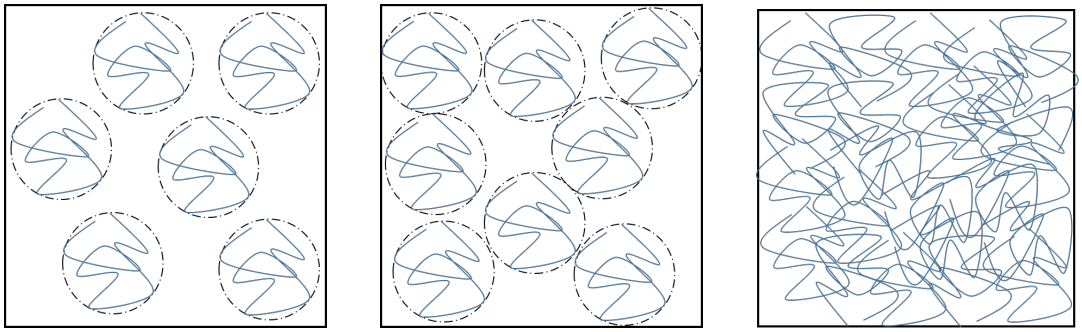

(A) (B) (C)

FIGURE 1.23: Diagrams showing the three regimes of polymer concentration, dilute (A) where polymer chains do not overlap, semi-dilute (B) where polymer chains begin to overlap, and concentrated (C) where polymer chains interpenetrate.

It is possible to calculate the osmotic pressure of a dilute polymer solution using Van't Hoff's Law, where N_p is the total number of depletion polymer coils and V* is the free volume available for the polymer coils to move freely.

$$\Pi_p = \frac{N_p k_B T}{V^*} \tag{1.32}$$

Fleer et al. [69] propose accurate approximations for both the osmotic pressure as a function of polymer concentration as well as the depletion thickness as a function of polymer concentration.

$$\frac{\Pi}{\Pi_0} = 1 + \left(\frac{\varphi}{\varphi_{ex}}\right)^{3\alpha-1} \tag{1.33}$$

$$\left(\frac{\delta_0}{\delta}\right)^2 = 1 + \left(\frac{\varphi}{\varphi_{ex}}\right)^{2\alpha} \tag{1.34}$$

Where Π_0 is the dilute limit, φ is the polymer concentration, φ_{ex} is an extrapolation concentration which is obtained by extrapolating the overlap concentration φ_{ov} towards $\Pi = \Pi_0$. α is the De Gennes exponent, that describes the concentration dependence of correlation length in the semi dilute regime.

1.7.2 Effects of Solvency

Calculating the radius of gyration is important for determining the colloid-polymer ratio as well as the polymer overlap concentration, however it can be affected by the

solvent used in a colloid-polymer mixture. There are three main categories that solvents are placed into. First is a good solvent, in which the interactions between the polymer segments and the solvent are preferable to the segment-segment interactions of the polymer. Therefore the polymer expands to maximise the segment-solvent interactions, in a good solvent the polymer is deemed swollen. The second solvent type is a poor solvent, in which the segment-segment interactions are preferable to the segment-solvent interactions which leads to the polymer shrinking to minimise the solvent-segment interactions. If the segment-segment and segment-solvent interactions are balanced then the solvent is defined as a θ solvent, so the polymer appears in its unperturbed state. Furthermore due to the enthalpy of the interactions being equal, any change to the radius of gyration of a polymer in a θ solvent is purely entropically driven.

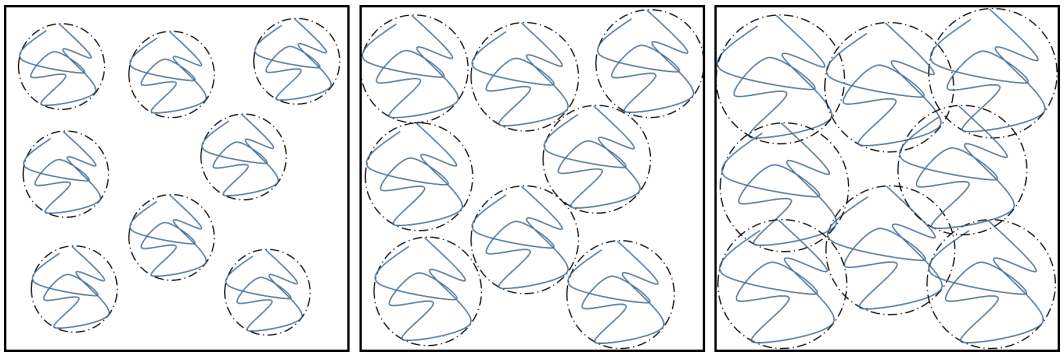

FIGURE 1.24: Three schematics showing the effect of solvency on a polymer solution, with the central picture being the polymer in a θ solvent, the left in a poor solvent, and the right in a good solvent.

1.7.3 Xanthan Conformation Behaviour

Xanthan in solution undergoes a conformational change from a double-helix to an α coil when heated, and then when cooled again it reforms into a hairpin structure (shown in Figure 1.25). This change in ordered structure from double helix "native" to hairpin "denatured", also corresponds to a change in viscosity, as shown by Milas et al. [70], therefore it is important to ensure only either the native form or denatured form of xanthan are used throughout a series of experiments.

The temperature at which xanthan undergoes this conformation change has been reported at wide variety of temperatures, some as high as 100 °C [70], and others as low as 45 °C [72]. Milas and Rinaudo explored the dependence of this transition on the

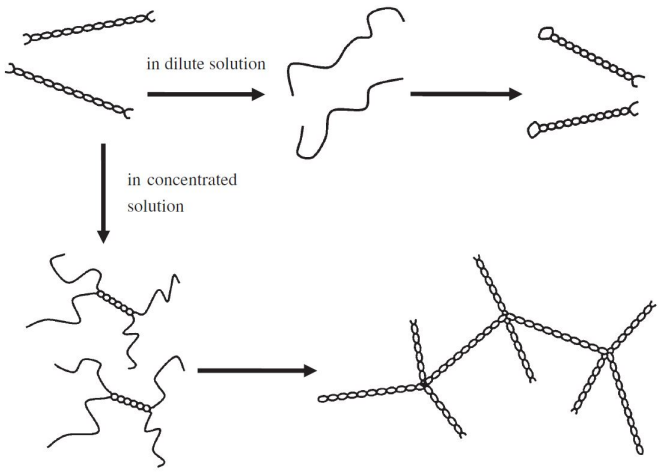

FIGURE 1.25: Schematic of denaturing and renaturing of xanthan molecule. Reproduced from [71].

ionic strength in the xanthan solution [73] and found that as ionic strength increases so does the melting temperature (T_m) of xanthan, this melting point was defined as the mid-point in the transition between the two conformations of xanthan. This relationship is plotted in Figure 1.26a with melting temperatures obtained using both optical rotation, polarising microscopy and circular dichroism. They also found that melting point of xanthan is independent of concentration (once its own contribution towards the ionic strength of the solution is accounted for). This dependence on ionic strength is also shown by Pelletier et al. [72] reporting a transition temperature of 45 °C in a 0.008 M (8 mM) NaCl solution, and Liu et al. [74] reporting a transition to a disordered state at 80 °C in a 0.01 M NaCl solution.

Figure 1.26b shows the intrinsic viscosity of xanthan in 10 mM NaCl as a function of temperature, as well as molecular weight and radius of gyration measurements at the peak (40 °C) and trough (50 °C). The increase in intrinsic viscosity seen was at T_m value already determined, this response appeared independent of xanthan concentration. Interestingly, they state that "the molecular weight and radius of gyration obtained by light scattering, the sedimentation constant, and the potentiometric behaviour are independent of temperature." suggesting that the size of the xanthan does not change with respect to temperature. However in Figure 1.26b the peak and trough have the same molecular weight but a different radius of gyration, the change is only 10 nm, but as previously shown in Section 1.5 a small change in polymer size can drastically affect the dynamics of a colloid-polymer system. It should also be

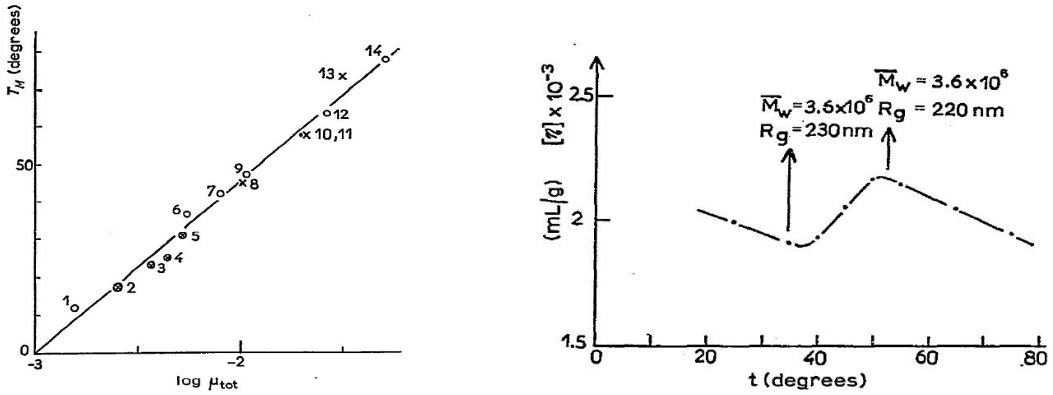

(A) Melting temperature of xanthan plotted against log of total ionic strength.

(B) Intrinsic viscosity as a function of temperature for xanthan in 10 mM NaCl.

FIGURE 1.26: Graphs showing the temperature responses of xanthan. Reproduced from [73].

noted no errors are given with these sizes.

Liu et al. [74] investigate the conformation change of xanthan in 0.01 M NaCl for a range of sonicated samples, giving molecular weights between 10.4 x 10^4 and 2.5 x 10^6. They performed polarimetry on samples across a range of temperatures also and found that for $[\alpha]_{300}$ there was one slope at low temperatures corresponding to an ordered structure (double-helix) and a different one at high temperatures corresponding to a disordered structure (coil), this can be seen in Figure 1.27. The straight line labelled $[\alpha]_{helix}$ corresponds to previous measurements of xanthan in 0.1 M NaCl, at this salt concentration no conformational change was observed.

Whilst the behaviour of xanthan has been much studied, often characterisation data such as size and melting temperature cannot be easily used in lieu of our own experimental characterisation, due to the wide variety of preparation techniques, molecular weights of xanthan, as well as the sensitivity of xanthan's size to ionic strength. Therefore we will characterise the size of xanthan at each temperature studied in this thesis, which is presented in Section 3.5.

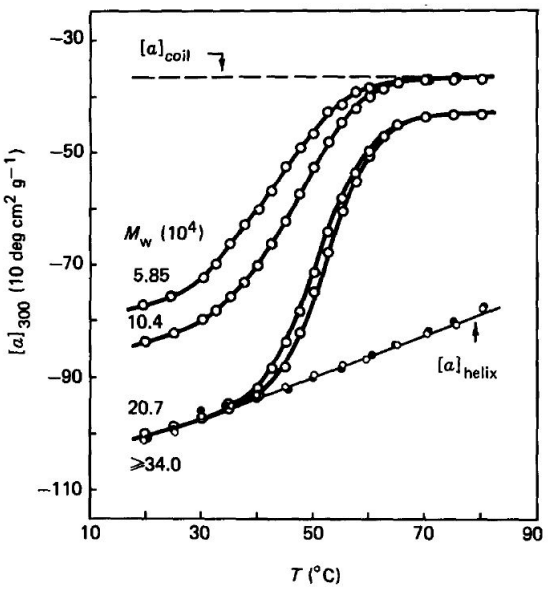

FIGURE 1.27: Curves of $[\alpha]_{300}$ as a function of temperature for various xanthan molecular weights. Reproduced from [74].

1.8 Conclusions and Thesis Questions

In this chapter we have discussed the challenges facing industrial formulation development. Currently it is difficult to predict the stability of a new formulation, and methods to measure stability are laborious and slow, taking months or even years. Temperature is often used to accelerate the collapse of formulations, but the effect temperature has upon the formulation is poorly understood.

Depletion gels arise in colloid-polymer mixtures due to the formation of a space-spanning network of particles, because of the depletion of a polymer from the surface of the colloids, giving an imbalanced osmotic pressure that causes the attraction. The phase behaviour of colloid-polymer systems can be accurately predicted using the Free Volume Theory of Lekkerkerker [32] and the semi-dilute behaviour of colloid-polymer mixtures by the Generalised Free Volume Theory of Fleer and Tuinier [24]. Colloidal gels appear deep into the phase diagram, at high polymer concentrations, where the depletion potential is sufficient to arrest phase separation. The effect of temperature on colloid-polymer systems has been little studied, with the phase diagram only changing with temperature when the size of the depletant and thus the range and strength of the depletion potential is changed.

There are two main mechanisms of gel collapse observed, creeping sedimentation

and delayed collapse. In systems that exhibit delayed collapse, a link between the microscopic dynamics occurring within the gel and the delay time before collapse τ_d has been found. An example of this relationship is the average lifetime of a particle-particle bond τ_{esc} being a similar multiple of τ_d for a system across multiple orders of magnitude. The difference between particle movement time-scale and the macroscopic collapse time-scale is attributed to the evolution of the space-spanning network within the gel gradually coarsening. Strain has been used to accelerate the ageing of colloidal gels, but no systematic work on the effect of temperature has been done, so the effect of temperature on the stability and structural evolution of gels remains to be seen.

The main motivation of this work being the understanding the factors affecting the lifetime of colloid-polymer gels, and how their collapse can be reliably accelerated, as well as identifying any early warnings of impending gel collapse. Therefore in Chapter 4 we will begin by studying the stability of a model colloid-polymer gel at ambient conditions, whilst controlling the temperature to a higher degree than previously used for the system.

In Chapter 5 we will explore the effect of temperature on the delay time τ_d on colloid-polymer gels, to find if and how reliably delayed collapse can be accelerated through elevating the temperature, much in the way industrial formulations are stored at higher temperature to accelerate collapse. This will allow us the opportunity to find if the acceleration of collapse seen in complex industrial formulations is a fundamental behaviour of colloid-polymer gels or only a behaviour exhibited by more complex systems.

Rheology is often used in industry to assess the robustness and stability of a new formulation, as measurements can be made very early in a gel's lifetime. Chapter 6 will focus on the effect of temperature on the rheological properties of freshly made gels, allowing us to probe both the structure formed at each temperature as well as the attractions present within a gel.

In Chapter 7 we shall use the technique Particle Tracking Velocimetry to probe mesoscopic changes in a gel before and during collapse, with an aim to explore how temperature changes the way the structure of a gel evolves over time, as well as allowing us to look for early warnings of gel collapse.

Chapter 2

Methods

In this chapter, we summarise the experimental methods used throughout this thesis. This includes the methods of controlling the temperature during the collapse experiments, as well as the image analysis performed to accurately determine τ_d. We also briefly discuss the rheology methods used to explore the rheological properties of both xanthan solutions and the PDMS-xanthan gel system. Finally, we describe how Particle Tracking Velocimetry (PTV) is performed, including the choice of tracer bead, how image tracking is performed, and how data is processed and analysed.

2.1 Introduction

In this chapter we discuss the practical considerations and methods used to collect the data presented later in this thesis. Firstly, we will summarise the development of a method to precisely control the temperature of gel collapse experiments for an extended period of time, as well as the techniques used to design and build the appropriate apparatus to achieve this. After this, we will discuss the image analysis performed to consistently and accurately determine the delay time before collapse τ_d of colloid-polymer gels. Whilst this is a key time-scale and gives insight into the effect of both polymer concentration and the temperature on the life-time of colloid-polymer gels, it does not give yield information on the underlying processes occurring within a gel. With this in mind, we expand the scope of methods used to include rheological measurements of both components within the gel and the gel as a whole. Finally, we will discuss the development of the method Particle Tracking Velocimetry (PTV), including imaging, the effect of the tracer beads on the gel, as well as image analysis and processing.

2.2 Design of Temperature Controlled Cell-Holder

In order to study the effect of temperature on a colloidal gel, a method of maintaining a stable and controllable temperature, which did not obstruct or interfere with any imaging techniques needed to be developed. Therefore, it was decided to use a recirculating water bath (Haake DC3) as it would provide excellent temperature control ($\pm$ 0.1 °C) and would allow a wide range of temperatures to be studied.

The key objectives of the cell-holder were to allow multiple samples to be imaged at once whilst retaining a high degree of temperature control. Therefore, the holder was initially designed to hold four samples at once, giving high throughput but still retaining sufficient resolution of each sample. The samples had to be illuminated from the rear to allow an interface to be reliably detected and tracked, so the rear of the cell-holder was made from clear perspex to allow the addition of a back light or laser. To minimise distortion of the images, there could be no obstruction in front of the samples. This meant the water jacket used to control the temperature was restricted so as not to go in front of the samples. However, this brought about another consideration. As the vials were sealed into the wall of the holder, finding the balance between a good seal without restricting the viewable portion of the sample (especially at the bottom of the vial where the interface appears at τ_d) was also very important.

An initial design based on a cell-holder design by Dixon [75] was made using perspex, rubber sealed windows and an aluminium lid. This design meant that no water passed in front or behind the cell, meaning imaging would not be obstructed, and also that the cells could easily be replaced and cleaned. Unfortunately, the rubber seals were very difficult to cut accurately and the window frames leaked. Also, the aluminium gasket lid, chosen to keep as much of the cell viewable, proved too flexible to seal fully. Due to the limitations of machined parts, and the relatively slow turn around, it was decided 3D printed parts would be advantageous, as they could be more rapidly made and improved. How these parts were designed and the software used is explain in Subsection 2.2.1.

The first change to be made was to print a lid and base, in which the cells would be held, to ensure proper sealing at the top of the cell-holder, whilst still maintaining

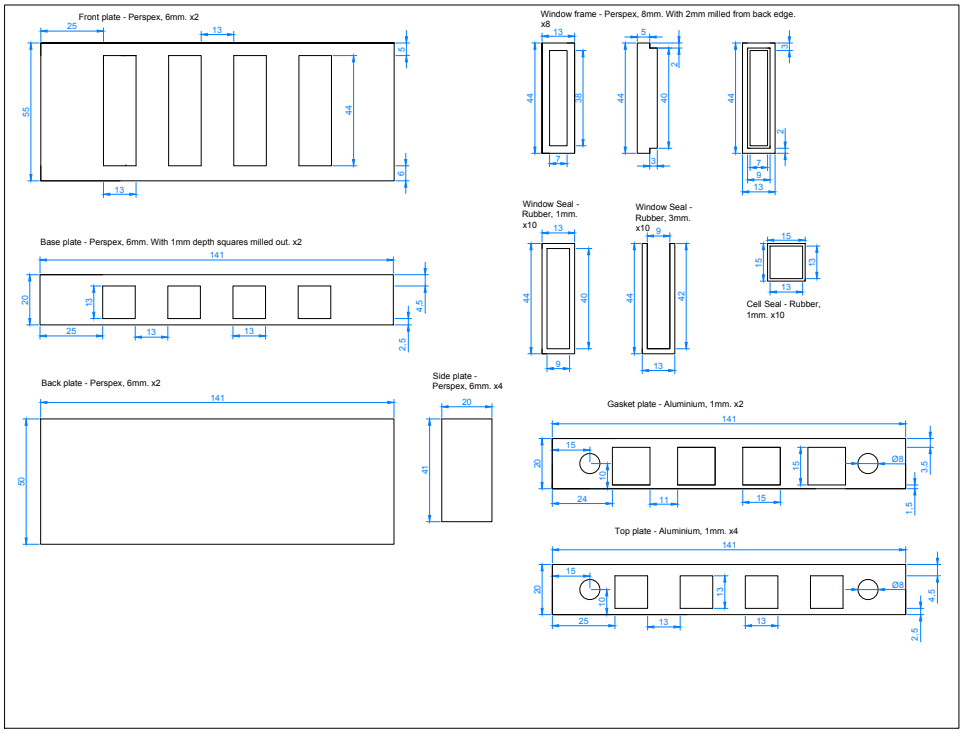

FIGURE 2.1: CAD file for components of initial temperature cell-holder design.

the ability to remove cells for cleaning. This can be seen in Figure 2.2b. Whilst this design improved sealing, the windows surrounding the cells could not contain water under pressure as it was pumped through the cell.

2.2.1 3D Printing

After success with 3D printed parts it was decided that the entire cell-holder would be 3D printed. 3D designs were generated using AutoCAD. The main holder was simplified to a single piece, which is shown in figure 2.1, with the cells now being permanently sealed in place to prevent leaking through the front. This was deemed necessary as any water leakage would obscure the bottom of the cell, preventing detection of the interface formed during gel collapse. Further to this, removal of the windows allowed for a smaller edge around the cell, maximising the area viewable through the holder.

The 3D printer chosen was a RepRapPro Ormerod 2 [76], which is shown in Figure 2.2a, and allowed designs to be produced to an accuracy of 0.1 mm. The Ormerod

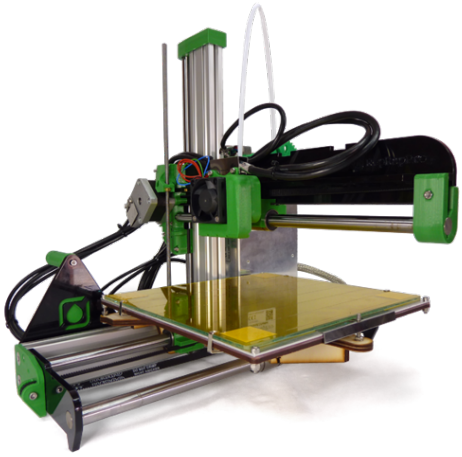

(A) Ormerod 2 3D printer reproduced from [76].

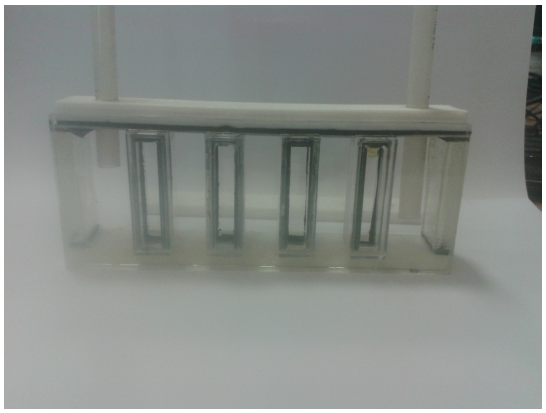

(B) First 3D printed cell-holder design assembled.

FIGURE 2.2: Overview of first 3D printed cell-holder design. Cell dimensions are 141 x 55 x 32 mm.

2 is a hot end extruder 3D printer, which uses polylactic acid (PLA) as a print material. With a melting point of around 160 °C, it would be more than resistant to temperature to use as a material for the cell-holder.

The high level of precision using AutoCAD and a 3D printer allowed the cells to fit snugly, and the bottom lip to be made the same thickness as the glass cell's base. The lid design became larger and more robust to minimise the effect of warping due to temperature as well as to prevent any leakage of water into the cells, as this would undoubtedly ruin any experiment. The water level would rise up to the lid as the pump was turned on due to the high throughput of the water bath, so foam was added to the lid, and the lid clamped down, to give a tight seal around the glass. In testing, it was obvious if water leaked into the cells as they would fill completely with water. The high pressure of the water pump was initially a hindrance in getting a sufficiently sealed system but once this problem was overcome, it afforded excellent temperature stability during the experiments.

To convert a CAD drawing to a printable design, it was first exported as a stereolithography (STL) file format and loaded into a g-code generator called Slic3r. G-code determines the position and speed of the print head, allowing for the solid thickness and infill of the 3D printed part to be adjusted, to balance print speed and final part quality.

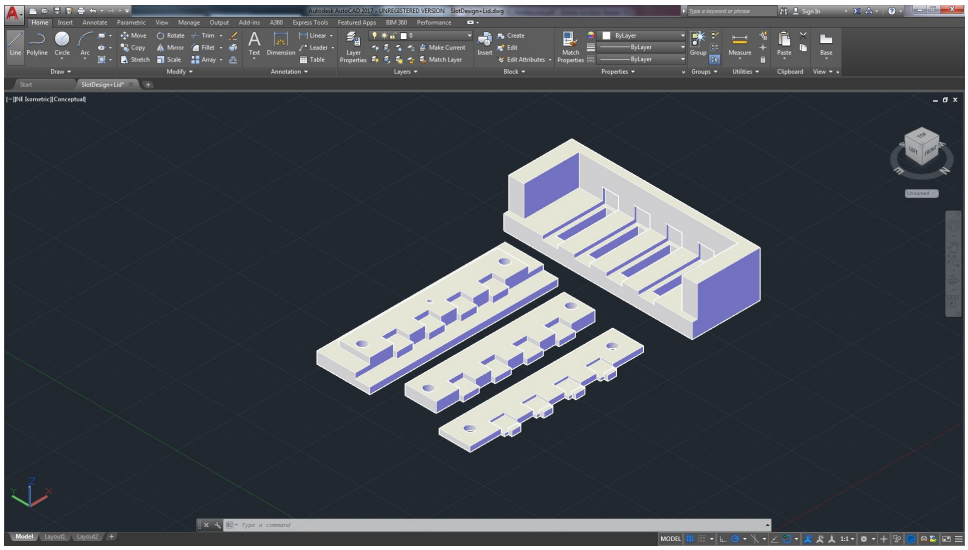

FIGURE 2.3: AutoCAD screenshot showing the evolution of the lid design (right to left) and the final cell-holder design.

2.3 Fluorescence Time-Lapse Microscopy

To study the evolution of colloid-polymer gels as they aged, a time-lapse camera was used to image the gels before, during, and after collapse. The camera used was an AVT Guppy F080B (Allied Vision) charge coupled device (CCD) camera, which had an image size of 1032 x 778 pixels. To improve contrast between the two phases formed as the gel collapse, an LED back light was also used. The rhodamine B dye in the aqueous phase was excited using a 532 nm beam-expanded laser (Laser Genetics ND3 x50), so that only fluorescent light is captured by the camera, a 550 nm long-pass filter (Thorlabs) was used.

The camera was mounted securely and could be adjusted up and down, as well as moved closer or further away from the samples. This ensured it was perpendicular to the cells and was adjustable up and down to ensure the samples were near the centre of the image to minimise any parallax errors. The cell-holder was clamped in place and pushed back against two supporting bars, firstly to allow the lid to be held tightly, and secondly to ensure the cell-holder was at 90 degrees to the camera, with all cells being the same distance away from the camera.

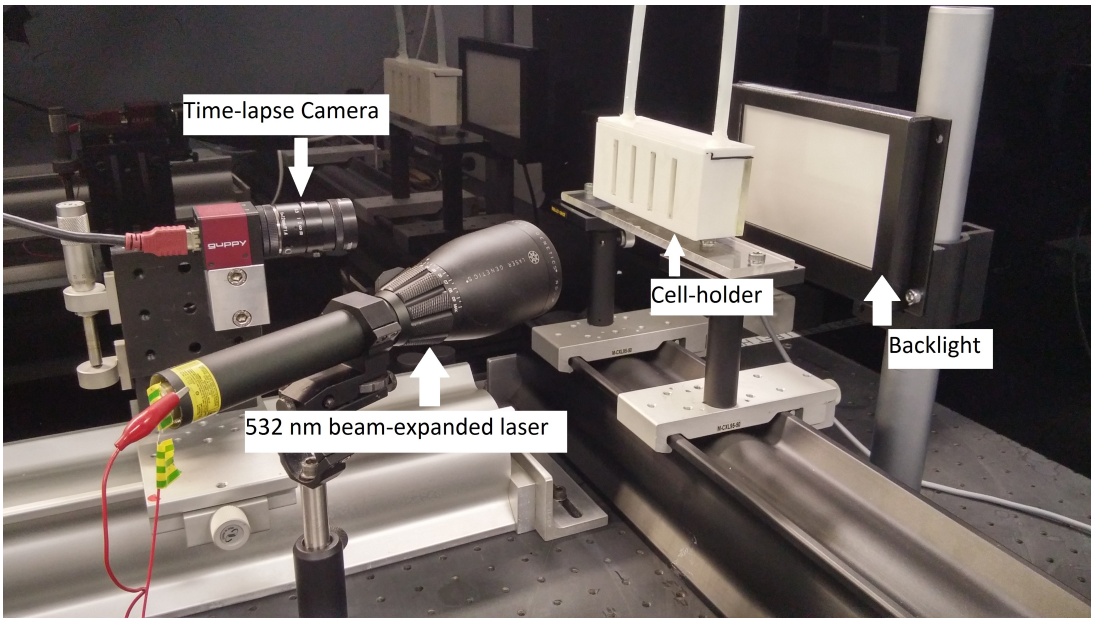

FIGURE 2.4: The set-up used to collect images during the gel collapse process.

2.3.1 Temperature Control

The temperature inside the cell holder was monitored using a platinum resistance data logger (PT-104, Pico Technology) and a 1/10 DIN accuracy platinum probe (PT100, SE012, Pico Technology). The data logger accuracy was 0.015°C and the probe accuracy ranged from 0.045 °C to 0.08 °C dependent on the temperature measured. Figure 2.5 shows just how stable the temperature of this set up was, with the temperature in the water bath being barely higher than that in the cell-holder, which is as to be expected, due to heat loss through the tubing to the cell-holder. The temperature is slightly higher ($\sim$ 0.2 °C) than the set temperature due to the desired temperature being close to the temperature of the lab, and both the heating element and refrigeration unit being used to achieve a stable temperature. Without the refrigeration the temperature would creep upwards as the experiment progressed. Variation during an experiment after the water bath reaches temperature was less than 0.1 °C. The standard deviation of the temperature was calculated to be 0.075 °C, with with a variation of less than 0.01 °C per minute. The desired temperature is reached in only a matter of minutes, with higher temperatures also being very quick to stabilise.

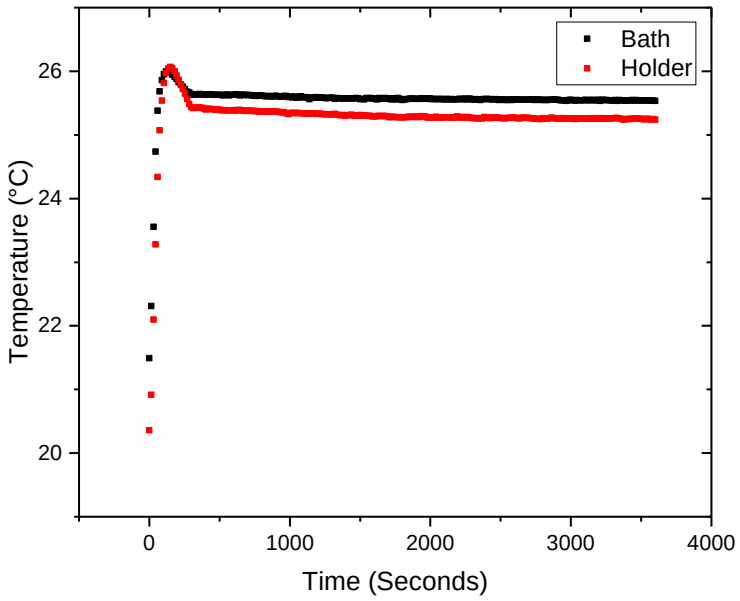

FIGURE 2.5: Graph showing the temperature measured when set to 25 °C.

2.3.2 Image Processing

Once time lapse videos had been captured, a reliable and consistent method to determine the delay time (τ_d) was required. Therefore, a LabVIEW image analysis code previously used by Teece et al. was used [25]. This allowed the interface to be detected (the time of detection thus determined as τ_d) and then tracked as the sample phase separated.

Image analysis was performed in three main steps, calibration, interface detection, and interface tracking. Calibration, is performed before data collection, where the region of interest is established and thresholded, alignment of the x and y axes is done, and pixel size is calculated. Calibration is carried out before an experiment is performed, and only needs to be redone if there is a change to the experimental set up. Interface detection, is where the interface between the two phases of a gel is determined, when a sufficient light-intensity gradient is detected between the fluorescent dyed phase and the non-fluorescent dyed phase. Interface tracking detects an interface in each image and calculates the height of the interface for each image of the time-lapse taken.

The main aim of the calibration is to convert the pixel size into millimetres, as

well as minimise the chance of any small distortions within the image affecting the results collected. Figure 2.6 shows the LabVIEW VI (Visual Interface) with which the calibration was carried out. A clear acetate, with a grid of dots 10 mm apart, was placed in front of the camera at the same distance as the samples, and an image taken. Then selecting "Align Co-ordinate Axis", a horizontal row of dots were selected, and then "Fix Co-ordinate Axis" was selected to calculate any slight tilt in the image. The image was then thresholded, yielding the red and black image on the right of the VI. The thresholding level could be adjusted to ensure only the dots on the acetate were red (the surrounding bench top could be ignored). Finally, "Calibrate Grid" was selected and an area with at least four dots were highlighted to calculated the pixel size in millimetres. Due to the design of the cell-holder and how it was held in place, the samples were always at a fixed distance so a calibration did not need to be carried out for each experiment.

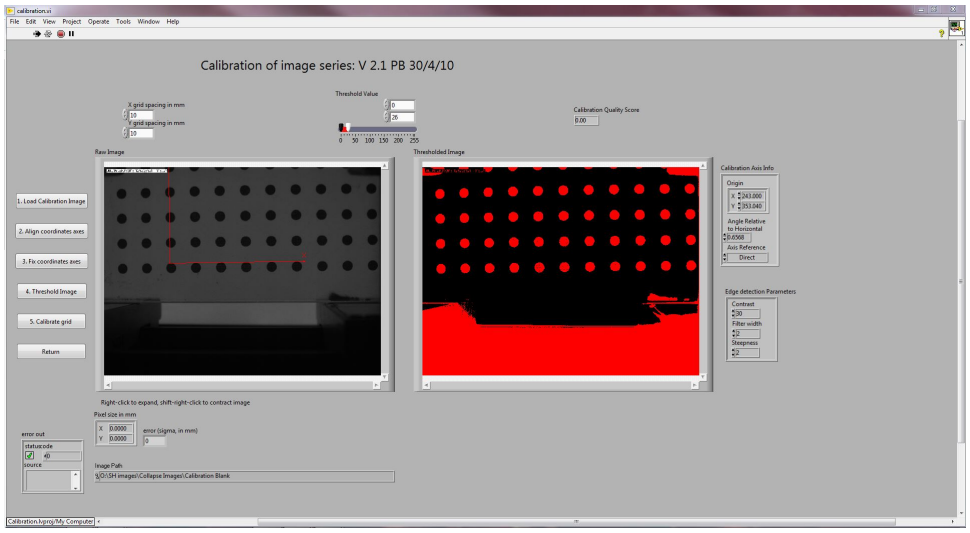

FIGURE 2.6: Screenshot of the calibration VI used to calibrate the camera used in the time-lapse video experiments.

Figure 2.7 shows the VI used to identify and track the interface in a gel sample. The width of the interface and light-intensity gradient could be adjusted to improve identification or to remove erroneous interfaces. A region of interest (ROI) was selected which covered as much of the viewable sample as possible, ensuring the bottom of the cell was included. A second ROI was also selected to measure the height of the meniscus, this also allowed us to look for any sample evaporation during a high temperature experiment as the height of the meniscus would move if any of the sample

was evaporating. There was a clear interface of dark to light which can be seen in the sharp peak in the intensity gradient generated. Figure 2.8 shows the sample at a later point, with the interface between the two phases significantly higher, clearly observed by the intensity gradient. There is also an example on an erroneous interface detected due to slight variations seen in the graph at the bottom right.

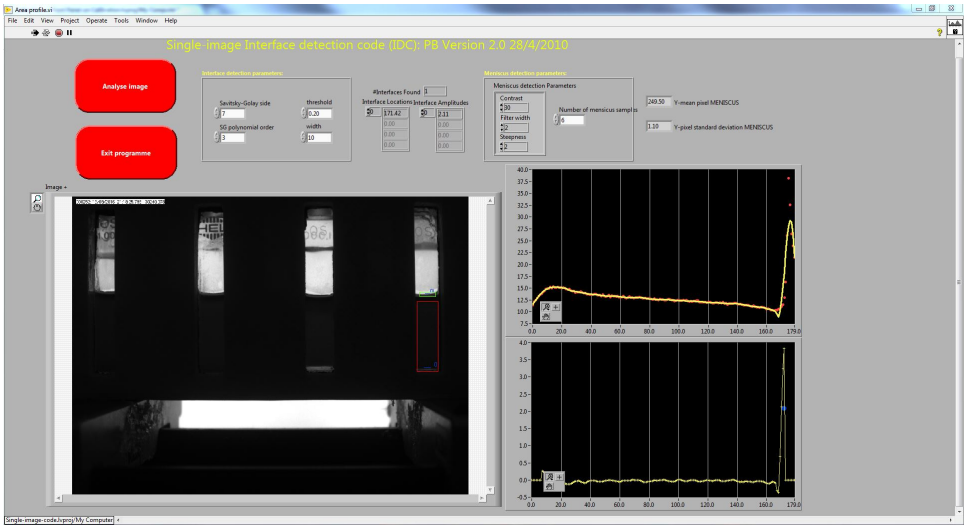

FIGURE 2.7: Screenshot of the VI used to process an image, with the interface and meniscus highlighted, shortly after τ_d.

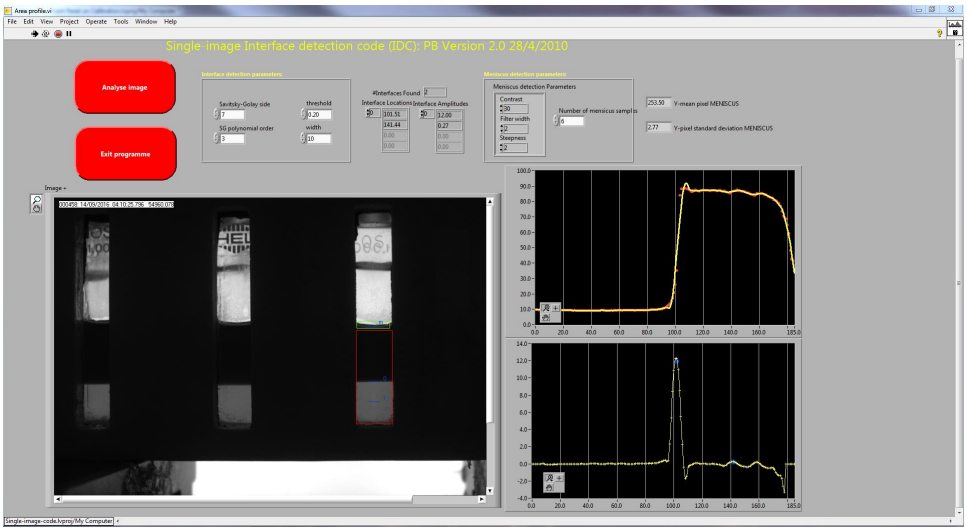

FIGURE 2.8: Screenshot of the VI used to process an image, with the interface and meniscus highlighted, significantly after τ_d.

Once the image analysis had been performed, a graph similar to that shown in Figure 2.9 was generated. This shows the initial delay time in which no interface was seen, the emergence of an interface at τ_d, which then moved rapidly up the sample, and then a slower pace as the sample compacts. To ensure the interface was being

detected at formation, image stacks were also compared by eye, due to the cell-holder being dark the interface was clear by eye as well as the code being easily able to identify it. So only minimal discrepancy was occasionally found, and was at most in the hundreds of seconds for the largest measured delay times, which were at least an order of magnitude greater. This slight uncertainty was also significantly smaller than the variation between samples of the same xanthan concentration so was statistically insignificant when analysing the data collected.

2.3.3 Generated Interface Height Profile

Highlighting the three main phases of delayed collapse, (delay, rapid-collapse, and compaction) was possible even without extra manipulation of the data. Previous work by Bartlett [46] plotted the interface height above the bottom of the cell (h/h_0) but due to the nature of the cell holder being dark is was not possible to reliably and accurately select this for image analysis. Despite this short coming, the key time-scales during delayed collapse were consistently observable.

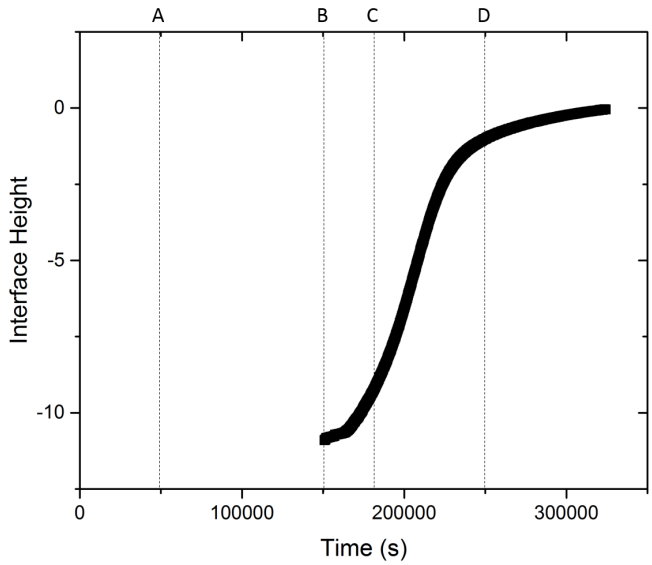

FIGURE 2.9: Height profile during the lifetime of a gel, with an interface appearing at around 150000 seconds, determined as τ_d. Letters A to D relate to the structure diagrams shown in Figure 2.10.

Figure 2.10 shows schematics of the gel structure at the snapshots labelled in Figure 2.9. A shows the structure when the sample is stable and phase separation has not begun, B shows the emergence of an interface also defined as τ_d, C shows

how the the interface moves up rapidly through the sample as the gel continues to phase separate, and finally, D shows how the interface moves at a slow rate during the compaction stage as the particles are already at a high volume fraction in the colloid-rich phase.

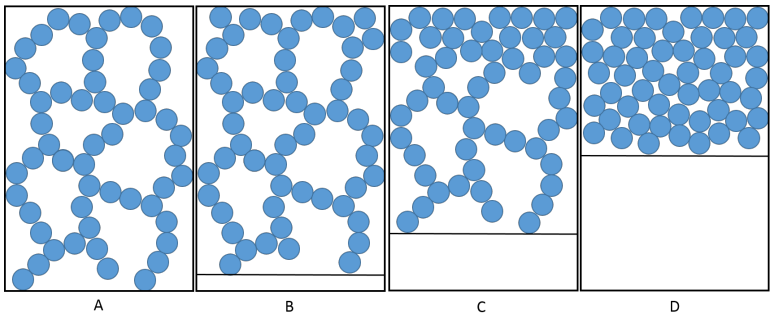

FIGURE 2.10: Four schematics showing the structure of a gel at different stages of its lifetime.

2.4 Rheology

A material falls into one of three broad rheological categories. It is either a solid (elastic), liquid (viscous), or is a mixture of the two, viscoelastic. When stress is applied to a solid, the deformation (strain) on the material is instantaneous and reversible, so when the stress is removed the material returns to its original shape. With a liquid, the strain increases gradually with time but is not reversible, so after the removal of the stress the material remains deformed. With a viscoelastic material the strain is not instantaneous and once the stress is removed some of the deformation is recovered, but not entirely. To determine whether a material is elastic, viscous, or viscoelastic, the common method used is a creep experiment, in which a step stress is applied to a sample and the strain measured during the application of stress, and then also after the stress is removed. This allows the strain response of the material to be observed, allowing the determination of whether it is elastic, viscous or viscoelastic.

Stress (σ) is defined in Equation 2.1, where F is the force applied and x and y are the dimensions over which this force is applied. Strain is defined in Equation 2.2, where Δx is change in x dimension, and z is the height. Here, we see that stress is a definite value (with units of Pa) and strain is a relative value, the amount of deformation (usually with units of %).

$$\sigma = \frac{F}{xy} \tag{2.1}$$

$$\gamma = \frac{\Delta x}{z} \tag{2.2}$$

Rheology measurements were carried out using an Anton Paar MCR 501 rheometer with a double gap geometry, and a Malvern Kinexus Pro rheometer with a cone and plate geometry (CP4/40). Each sample was sheared at 100 s^{-1} for 5 minutes and then allowed to recover for 15 minutes before each amplitude sweep was performed, to minimise load effects. Samples were refreshed by shearing at 100 s^{-1} for 5 minutes, and then allowed to resettle, comparison of data from fresh and refreshed gels showed this did not impact the data collected.

(A) (B)

FIGURE 2.11: Cross sections of the two geometries used, a cone and plate geometry (A) and a double gap geometry (B).

Figure 2.11 shows cross sections of the two different geometries used for rheology measurements. The advantage of using a double gap geometry, whilst more laborious to clean and load the sample precisely, is that due to the significantly greater surface area of the geometry in contact with the sample, it is much more sensitive, detecting both smaller changes in materials as well as allowing much weaker materials to be studied.

2.4.1 Steady Shear Viscometry

The first type of rheology experiment performed was a shear rate sweep, in which the viscosity of the sample is probed at different shear rates. For a Hookean solid, the relation between stress and strain is $\sigma = G\gamma$, and for a Newtonian liquid it is $\sigma = \eta\dot{\gamma}$ [77]. Therefore, by rearranging this to Equation 2.3, it can be seen that applying a known shear stress at a known shear rate allows the calculation of the viscosity of a liquid.

$$\eta = \frac{\sigma}{\dot{\gamma}} \tag{2.3}$$

This method was used to determine the low shear viscosity of xanthan solutions by performing a table of shear rates on a xanthan solution and extrapolating the plateau seen at low shear rates (where η is independent of shear rate) back to zero.

2.4.2 Oscillatory Rheology

Oscillatory rheology is used to measure a material's resistance to deformation, either by applying a stress or strain, measuring a complex modulus (G^*), which is the overall resistance to deformation of a material, and comprises of an elastic (or storage) modulus G' which represents a solid-like response and a viscous modulus G'' which represents a fluid-like response. Equations for how these are calculated as shown below[77].

$$G^* = G'\omega + iG''(\omega) \tag{2.4}$$

$$G'(\omega) = \frac{\sigma}{\gamma}cos(\delta) = G^*(\omega)cos(\delta) \tag{2.5}$$

$$G''(\omega) = \frac{\sigma}{\gamma}sin(\delta) = G^*(\omega)sin(\delta) \tag{2.6}$$

This method is used to identify the Linear Viscoelastic Regime of a complex material, the LVER is determined as the regime in which the properties of a material are unchanged by the applied strain. In Figure 2.12, the magnitude of G' and G''

remain unchanged up to 1 % strain, before G′ begins to decrease, therefore for this sample, the LVER would be determined as up to 1 % strain.

Figure 2.12 shows a strain sweep at 25 °C, with the elastic (G′) and viscous (G″) moduli on the left hand axis and the phase angle on the right. Initially the sample is weakly gelled with G′ being greater then G″ but with a phase angle of around 40°. However, as the strain is increased, the elastic modulus eventually begins to drop, at 1 % strain, which signals the breakdown of the internal structure of the gel. Then at 14 % strain, the elastic modulus becomes lower than the viscous modulus, at this point the sample begins to behave as a visco-elastic fluid rather than a solid.

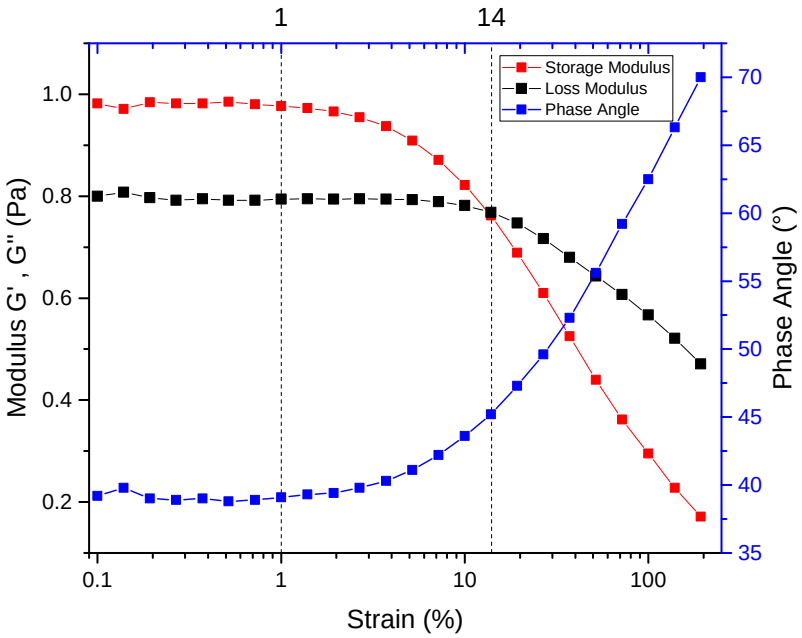

FIGURE 2.12: Strain sweep of a 1.0 g L^{-1} Xanthan and PDMS gel.

The critical strain (or stress if measuring as a function of stress) is determined as the strain at which the elastic modulus begins to decline, below which the structure of a sample is intact [78]. So in Figure 2.12 this would be at 1 % strain as shown. It can also be defined as the strain at which G′ becomes lower than G″, indicating the change from solid-like behaviour to fluid-like behaviour. Again, for Figure 2.12 this would be determined as 14 % strain.

Figure 2.13 shows how G′ and G″ evolve after the sample is loaded into the rheometer, with the sample being given no recovery time. The magnitude of G′

increases from 1.0 Pa to 1.1 Pa and then levels off at around 1200 seconds, and G″ does not change after the sample is loaded, therefore as previously stated the samples were left for 15 minutes before performing rheology measurements to minimise any variation in the measured value of G′.

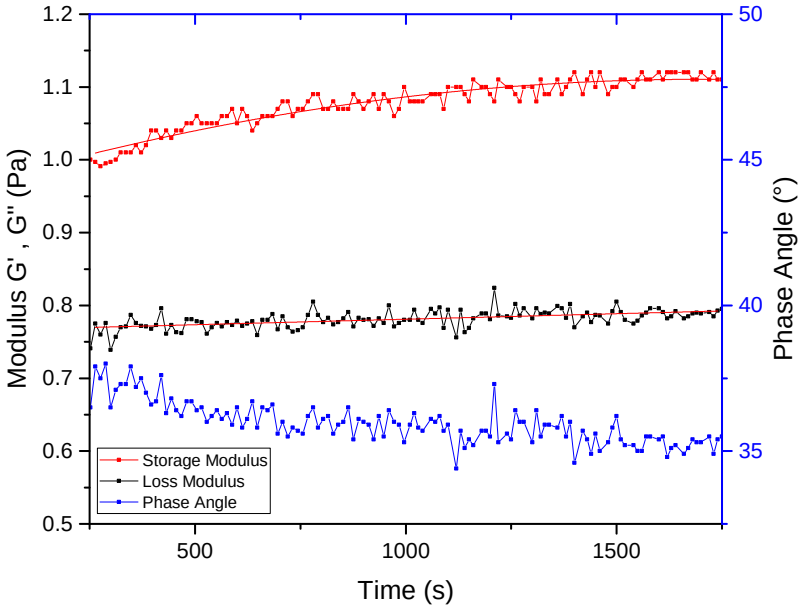

FIGURE 2.13: Oscillatory Rheology with fixed 0.2 % strain for a 1.0 g L^{-1} gel at 25 °C.

2.5 Particle Tracking Velocimetry

To study the dynamics of a gel before collapse, Particle Tracking Velocimetry (PTV) was used, which has been extensively used for tracking fluid flows [79–81]. This involves seeding fluorescent tracer beads within the gel and then tracking the position of these beads as the gel ages. This allows the velocity and displacement of the beads to be calculated from their positions, hopefully giving insight into the dynamics of a gel before macroscopic collapse is seen.

2.5.1 Tracer Size

In PTV, each particle is individually tracked, frame by frame, therefore the number of particles used in the technique is relatively low, minimising any disruption to the

gel network. The selection of a suitable tracer particle to use is key, as the stress it exerts on the sample, the level of fluorescence, and the ability to image the particle must all be considered.

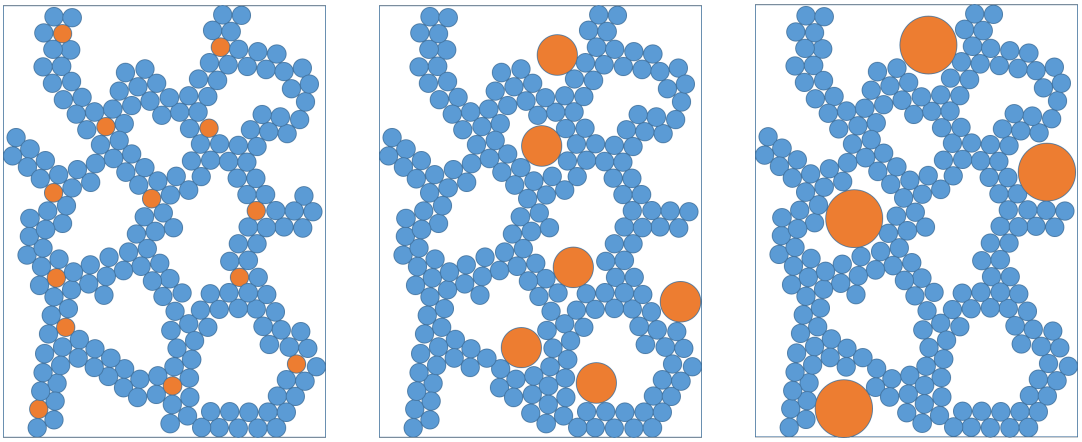

(A) (B) (C)

FIGURE 2.14: Schematics showing three different tracer particle sizes and how they might be incorporated into the gel structure.

Figure 2.14 shows schematics of three different tracer particles and how they might be incorporated into a gel. 2.14a shows beads that are of order the size of the network particles, and are incorporated into the structure of the gel. If the particles were this size, you would expect to be able to observe individual particle movement within the strands, so would see significant movement at even initial time-scales. 2.14b shows where the particles are significantly larger than the particles making up the network of the gel, and are thus not part of the network, but are smaller than the pores within the gel. Therefore, you may expect initial movement as some particles may be able to move freely within pores before becoming trapped either at strand junctions or in smaller pores. 2.14c shows a schematic of tracer particles similar in size to the pores in the gel network. In this case you would expect very little movement as the particles are embedded in the network and will only be free to move once the structure of the network around the particles has changed as the samples ages.

Whilst 2.14a would be advantageous as it would allow direct measurement of single particle dynamics, the practicality of this in our experimental system would be effectively impossible, as the PDMS droplets forming the space-spanning network are around half a micron and are too small to image with a confocal microscope, so similarly sized tracer particles would not be visible using a conventional CCD

camera. Plus at this size, it would be difficult to accurately track particles due to the significant movement, even when the sample as a whole is stable. 2.14b and 2.14c, however, would work well as they would be of sufficient size to image and track successfully, and give an indication of local strand dynamics of the gel, due to them being partially or initially trapped in the pores of the gel (previously measured as up to 45 μm [56]), which could be reasonably imaged and tracked.

With these considerations in mind, the particles selected were FluoroMax (Thermo Scientific) 36-11 fluorescent polystyrene divinylbenzene particles, of two sizes, 100 $\pm$ 7 μm and 26 $\pm$ 7 μm, both with a density of 1.05 g cm^{-3}.

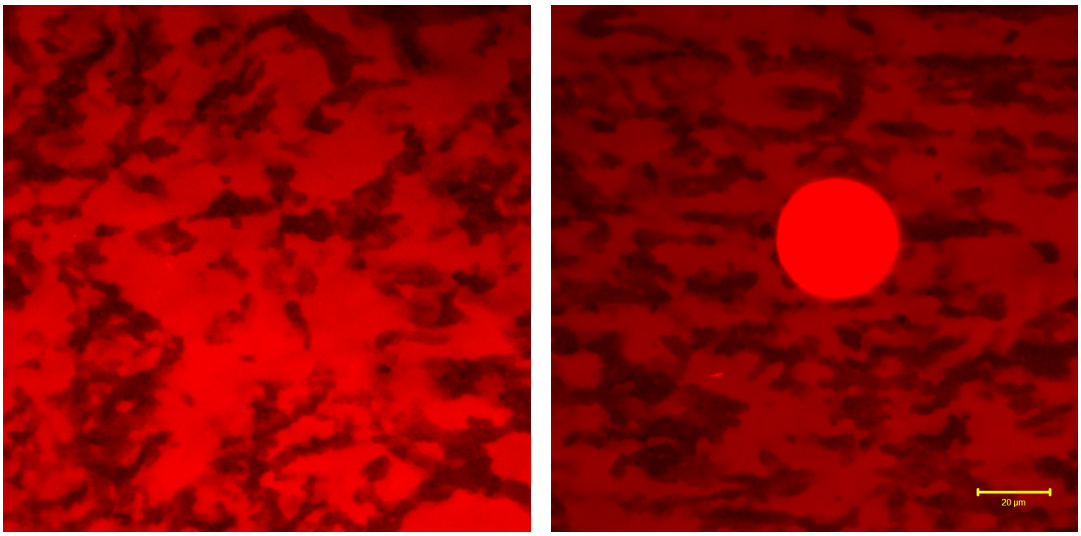

(A) Confocal microscope image with no tracer beads in sample.

(B) Confocal microscope image with tracer beads in sample.

FIGURE 2.15: Confocal images of 0.8 g L^{-1} xanthan-PDMS gels, with the black portions being the strands of the gel network, the red being the continuous phase, and the large red circle in B being a tracer bead.

2.5.2 Stress Exerted on the Gel Network

Another important consideration with the selection of particles, is whether they are of sufficient size and density to damage the network around it. This would leave to the particle's movement not being dictated by the dynamics of the gel network but merely it smashing its way through the gel. Previously, the yield stress of the gel has been estimated to be $\sim$ 0.1 Pa [46].

To estimate the stress exerted on the gel by a tracer particle, the buoyant force was calculated using Equation 2.7, where r is the particle radius, ρ_{tracer} is the particle density, and ρ_{fluid} is the density of the fluid phase. Then using Equation 2.8, the surface area over which this force is applied is calculated, with Equation 2.9 giving the pressure/stress exerted on the gel by the particle.

$$F_{buoy} = \frac{4}{3}\pi r^3(\rho_{tracer} - \rho_{fluid}).g \tag{2.7}$$

$$A_{tracer} = 2\pi r^2 \tag{2.8}$$

$$P = \frac{F_{buoy}}{A_{tracer}} \tag{2.9}$$

Table 2.1 summarises the values calculated for both the 100 μm and 26 μm particles, with the stress for the 100 μm being lower than the yield stress of the gel, therefore, the possibility of the particles stripping through the gel is quite low. Moreover, the 26 μm particles have an even lower stress, an order of magnitude lower than the nominal yield stress of the gel. However the smaller the size of the tracer reduces the chances of particles disrupting the gel. The less the particles disrupt the gel, the more likely they are to be a true "tracer" particle.

Particle Size	100 μm	26 μm
F_{buoy}	6.07 x 10^{-10} N	9.49 x 10^{-12} N
A_{tracer}	1.57 x 10^{-8} m^2	9.82 x 10^{-10} m^2
P	0.04 Pa	0.01 Pa

TABLE 2.1: Calculated stress exerted on the gel network by the tracer particles.

The ensure the tracer particles did not affect the gel in a significant way, strain sweeps were performed on gel with and without tracer beads, and can be seen in Figure 2.16. The addition of the beads does not change either the elastic or viscous modulus of the gel (the slight variation between the two is expected and a similar degree of variation can be seen in Chapter 6), as well as the response of the gels to strain. If the particles were having a significant impact on the structure of the gel,

we might expect the elastic modulus to be lowered or the response to strain to be shifted, due to the particles adding an internal stress to the gel.

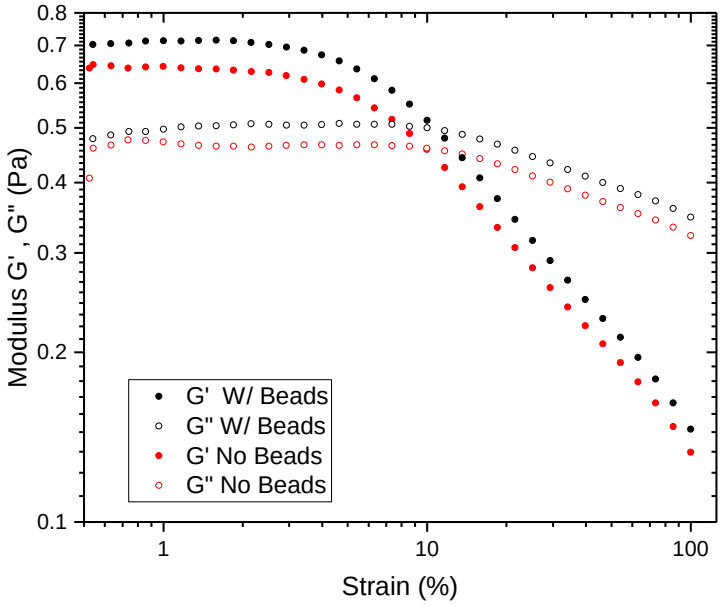

FIGURE 2.16: Strain Sweeps of two 0.8 g L^{-1} xanthan-PDMS gels with and without tracer beads added.

2.5.3 Imaging and Tracking

The gel samples were prepared in the same way as described in Chapter 4, only with tracer beads added to the PDMS stock emulsion before mixing. The sample was then loaded into the cell-holder and the sample illuminated from behind with a 532 nm beam expanded laser (Laser Genetics ND3 x50). The camera used was a Guppy Pro F-503 (Allied Vision) CCD with an image size of 2588 x 1940 pixels. Once set up and focused, the pixel size was determined to be 15 x 15 μm. This would mean that, a tracer bead would occupy multiple pixels at once, minimising the error in both identify and tracking particles.

To track the particles, a Python package called Trackpy was used [82], which uses the Crocker-Grier tracking algorithms to locate features and track them within an image stack [83]. The previously written code consisted of two parts, the first to identify and track the tracer beads, and the second to calculate and plot various outputs, such as: speed, x and y velocities, displacement, and features present [84].

Tracking and identifying features are obviously key in gaining useful data, as if features are not reliably tracked throughout the experiment, then either movement that is present will not be identified or anomalous features that are not tracer beads will be identified. The parameters used in determining the features to track are: feature_size, feature_minmass (minimum integrated brightness), feature_maxsize, and feature_separation (allows very close features to be differentiated.)

Figure 2.17 shows the same sample but with different identification parameters used, mainly the minimum brightness parameter. In A, only the very brightest beads are identified as features, with this few tracer beads, any movement identified may not be representative of the sample as a whole.

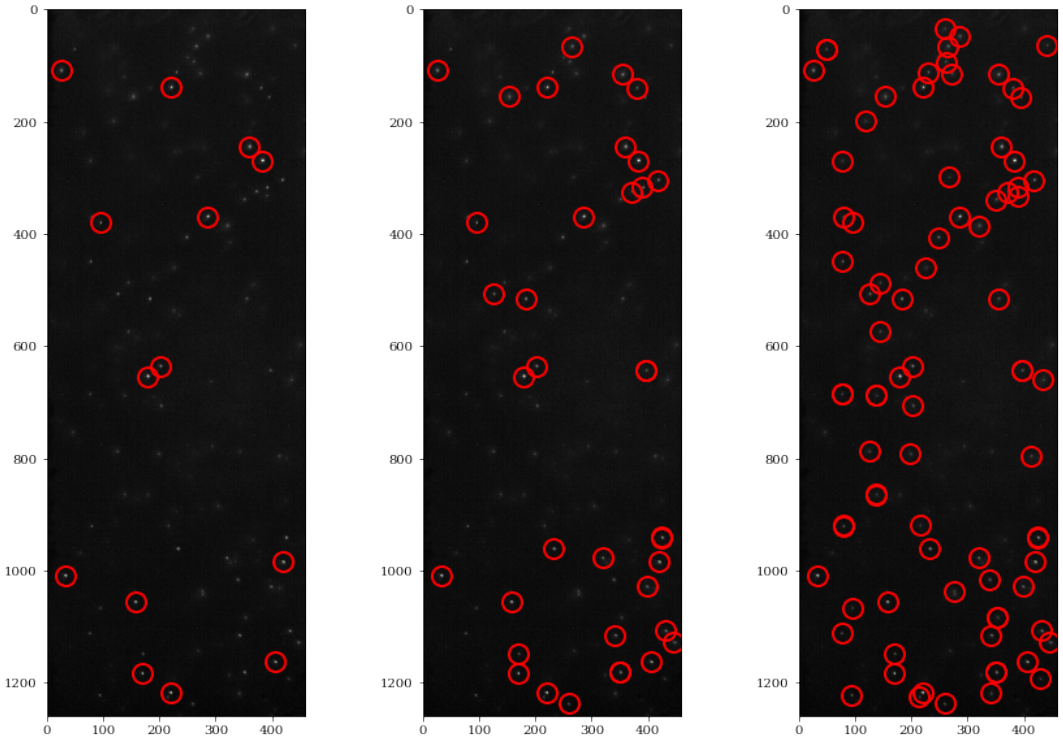

(A) (B) (C)

FIGURE 2.17: Three PTV images where the minimum brightness parameter has been decreased from left to right, meaning more particles are detected as features by the tracking code.

Figure 2.18 shows the particle trajectories for three different time frames early in a gel's lifetime, here we see the ability to track multiple complex trajectories over time, giving an element of spacial resolution, as we can see a failure in the top-left of the sample gradually propagate throughout the sample.

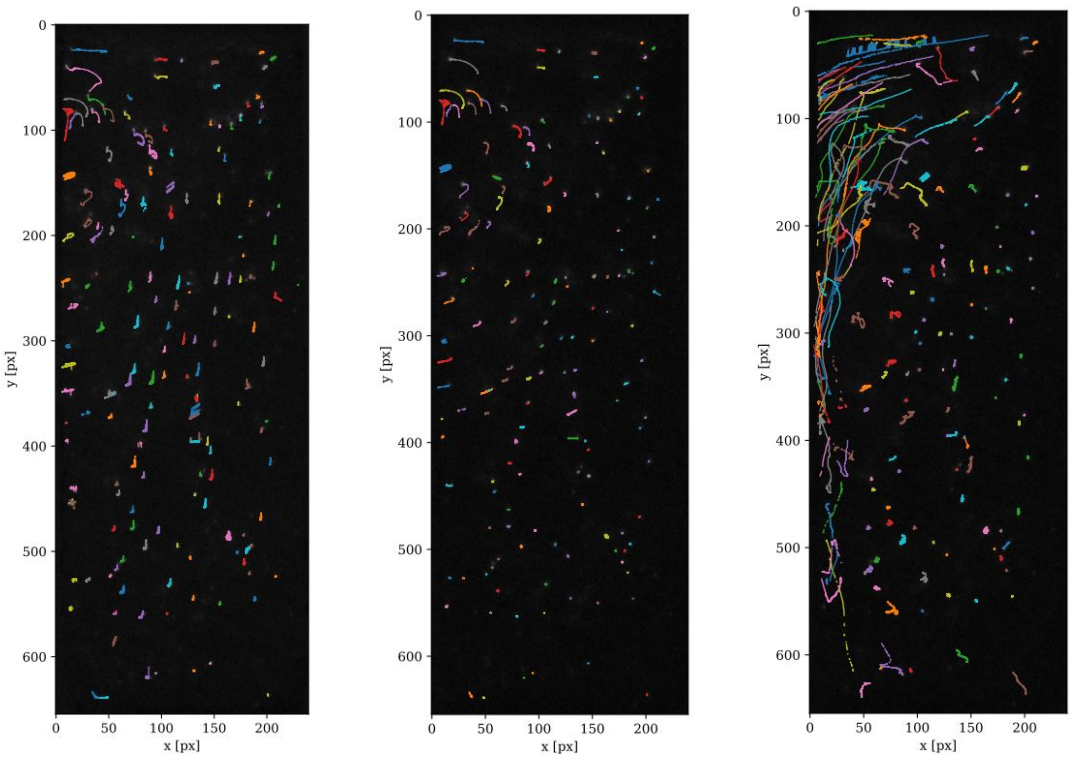

(A) (B) (C)

FIGURE 2.18: Particle trajectories tracked for three different times before collapse,(A) 0-500, (B) 501-1000, (C) 1001-1500 frames, for a 0.7 g L^{-1} at 25 °C.

2.5.4 Velocity Calculations and Errors

Once features have been successfully identified, they can be tracked throughout the sample as it ages, which then allows x and y velocities as well as displacement to be calculated. The x and y velocities are then combined to give a dimensionless speed using the equation below.

$$v(f) = \sqrt{v_x(f)^2 + v_y(f)^2} \tag{2.10}$$

These individual velocities are calculated using Equation 2.11. Where $v_x(f_n)$ is the particle's x component velocity of frame n. $x(f_n)$ is the particle's x position in frame n, and $x(f_{n-l})$ is the x position in the $(n-l)$th frame. l is the frame look-back value, and t_i is time (s) between frames. To convert from pixels to metres, the conversion factor MPP (Metres Per Pixel) is used.

$$v_x(f_n) = \frac{x(f_n) - x(f_{n-l}) \times MPP}{l \times t_i} \tag{2.11}$$

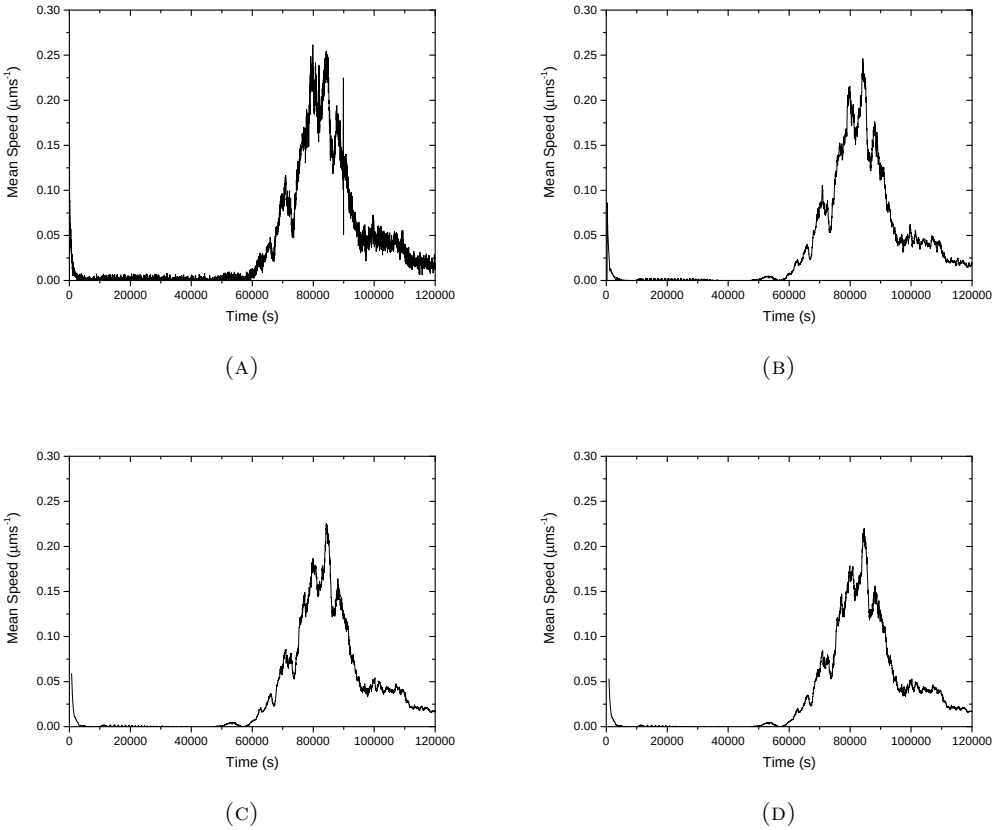

FIGURE 2.19: Mean speed of tracer particles for a 0.8 g L^{-1} gel at 25 °C calculated using different values of l. (A) 1 frame, (B) 10 frames, (C) 25 frames, and (D) 30 frames.

Figure 2.19 shows the mean speed for a sample calculated using Equation 2.10. However, each graph uses a different value for l when calculating the velocities using Equation 2.11. With only a 1 frame look-back (A) to calculate velocity, there is a large amount of noise in the mean speed, making it very difficult to ascertain when key features occur during the experiment, for example, the time at which the peak speed occurs (τ_{max}), also errors in either the particle tracking or a change in illumination of the sample yield significant fluctuations ($\sim$ 90000 s). When the frame look-back is increased to 10 frames (B), the noise is reduced significantly, and single image errors are no longer seen, however the velocities (and thus speed) calculated are reduced due to this increased look-back time. This is also observed when the look-back is increased further to 25 and 30 frames. This decrease in magnitude of both velocity

and speed is expected as the velocity calculation does not take into account every frame of the look-back window, but at two frames separated by l number of frames. Therefore, as the movement of tracer particles within the sample have a Brownian component and do not move in a perfectly straight line, larger look-back windows effectively smear out some particle movement. Therefore, a balance between time resolution and data noise must be struck.

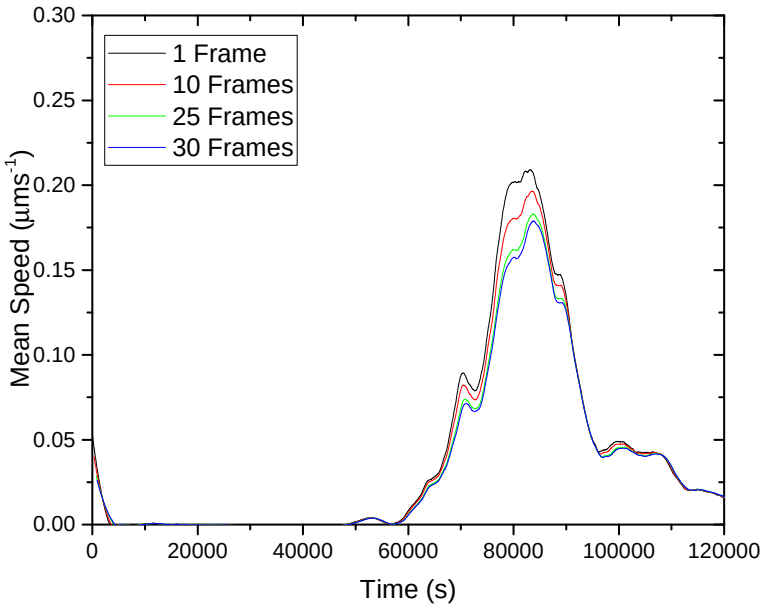

FIGURE 2.20: Mean speed of tracer particles for a 0.8 g L^{-1} gel at 25 °C calculated using different values of l (1, 10, 25, and 30 frames). Then all were smoothed as described in Section 2.5.5, using a 250 POW.

Another consideration when looking at the optimum look-back window is the error associated with the calculated velocity. The maximum error with this has previously been calculated in Equation 2.12. Where, Δt is the time across which the velocity is calculated, and ϵ is the error associated with the particle position [84].

$$\delta v = \frac{4\sqrt{2\epsilon}}{\Delta t} \tag{2.12}$$

2.5.5 Data Processing and Smoothing

Despite the velocity calculations and errors being optimised, some of the data plots showed significant noise, which made comparing the shapes of curves as well as determining key time-scales, such as the time of peak velocity τ_{max}, difficult. An example of this is shown below in Figure 2.21a, where multiple peaks appear to have a similar velocity, so τ_{max} could only be reasonably estimated between 140000 and 160000 seconds. Therefore, the decision was made to smooth the data to remove this noise in a consistent and statistical manner.

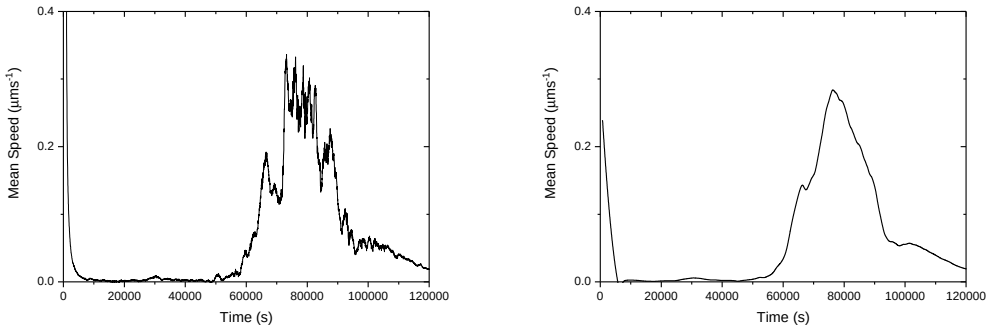

(A) (B)

FIGURE 2.21: Mean speed of tracer particles for a 0.8 g L^{-1} gel at 30 °C, (A) being the raw data, and (B) being the data smoothed using a Savitzky-Golay filter with a 250 POW.

Multiple techniques to smooth the data were considered, including a simple to apply percentile filter, to a more complex and involved method of performing a Fourier transform to remove high frequency values. However, the method of smoothing used was the Savitzky-Golay filter [85, 86], as it could be easily adapted to the data sets and was simple to perform using Origin. A Points of Window (POW) value is selected, over which a least-squares polynomial fit is performed, therefore selecting an appropriate POW to minimise noise but still preserve the underlying data is key.

Figure 2.22 shows smoothed data using four different POWs, 100, 250, 500, and 750 data points, the raw data used for this is shown in Figure 2.19c. Using 100 POW retains most of the jaggedness of the raw data whilst removing significant amounts of noise, but despite this still leaves three peaks around τ_{max}, furthermore, the slope to τ_{max} is difficult to quantify due to the jaggedness being retained. 250 POW combines these three peaks into one with only slight bumps, and maintains an

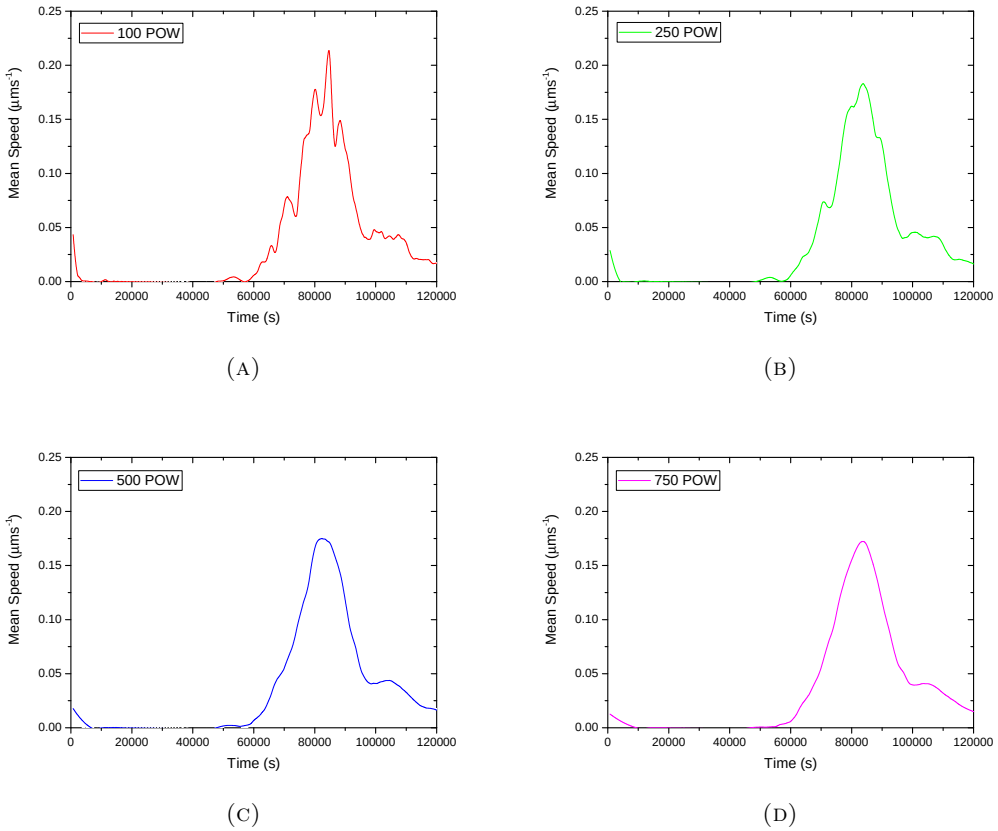

(A) (B)

(C) (D)

FIGURE 2.22: Four different smoothing POW values used for a 0.8 g L^{-1} gel at 25 °C.

element of sharpness to the point of τ_{max}, the slope to τ_{max} is significantly smoother also. POWs of both 500 and 750 make the peak almost completely smooth with only a single peak, which is rounder than both 100 and 250.

Another consideration with data smoothing is how the magnitude of the data is affected. To better understand this, in Figure 2.23 the four different POWs used are overlaid and the maximum speed v_{max} is compared. Here, it is clear to see that as the POW is increased, v_{max} decreases, with the biggest jump being from 100 to 250 points, with 500 and 750 only decreasing slightly.

After consideration, 250 points was decided to be the best balance between removing noise, but still retaining some resolution of the jaggedness and variability of the particle speeds, as overly smoothing the data may lead to homogenising all the results. However, in some cases the POW is adjusted to smaller values for high temperature experiments performed over a short time or when comparing more localised timeframes within an experiment.

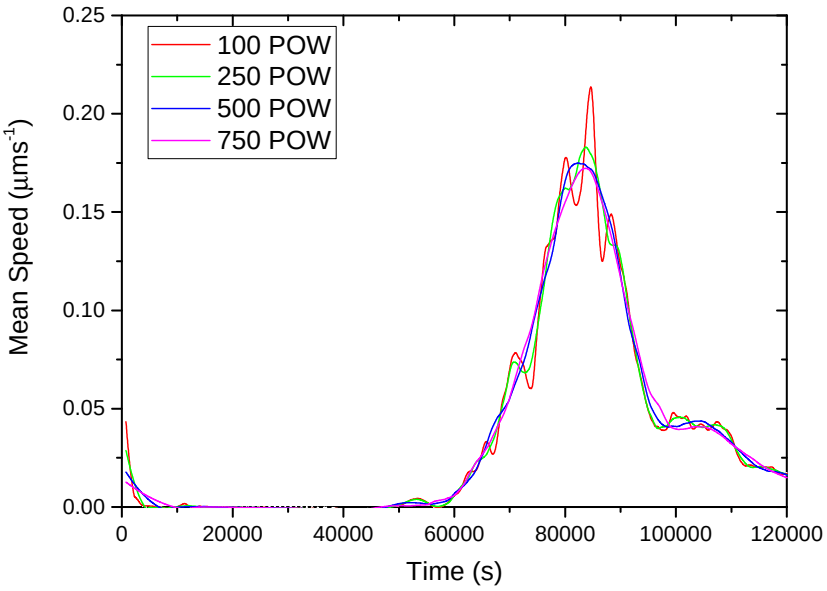

FIGURE 2.23: Four different smoothing POW values used for a 0.8 g L^{-1} gel at 25 °C.

Chapter 3

Materials

In this chapter, we summarise the experimental materials used to form the colloid-polymer gels studied, including the PDMS droplets, the two polymer depletants xanthan and HEC. We also characterise the ethylene glycol/water solvent and how both the density and viscosity of it change with temperature. We then summarise the gel composition and preparation methods used for the data presented throughout this thesis.

3.1 Summary of Gel Composition and Preparation

The gel studied is an emulsion formed of PDMS (polydimethylsiloxane) droplets ($a = 316 \pm 11$ nm and a polydispersity index of 0.18) dispersed in a mixture of ethylene glycol (1,2-ethanediol) and water. The PDMS droplets were stabilised using a combination of surfactants: synperonic PE/P103, tristyrylphenol ethoxylate (TSPE) and Na-AOT. The mass fraction of ethylene glycol was 0.61 to achieve refractive index matching with the PDMS droplets to allow vision into the sample for imaging.

A small amount of potassium chloride (3 mM) was added to the samples to screen any long-range electrostatic repulsions, Sudan black dye was added to the oil-phase and rhodamine B dye added to the aqueous phase to improve contrast when imaging. A depletion interaction was induced between the PDMS droplets through the addition of xanthan gum ($M_w = 4.66$ x 10^6 g mol^{-1}, $R_g = 194$ nm), giving a colloid-polymer ratio of 0.62 ± 0.04, a long-range but weak attraction between the droplets [25].

A second gel was studied using hydroxyethylcellulose (Natrosol 250 HHX) as the depletant, keeping all other components the same as the xanthan gel shown in Table

3.1. The molecular weight of the HEC was measured as 1.3 x 10^6 with a radius of gyration of 126 nm, giving a colloid-polymer ratio of 0.40, a strong but intermediate-range attraction.

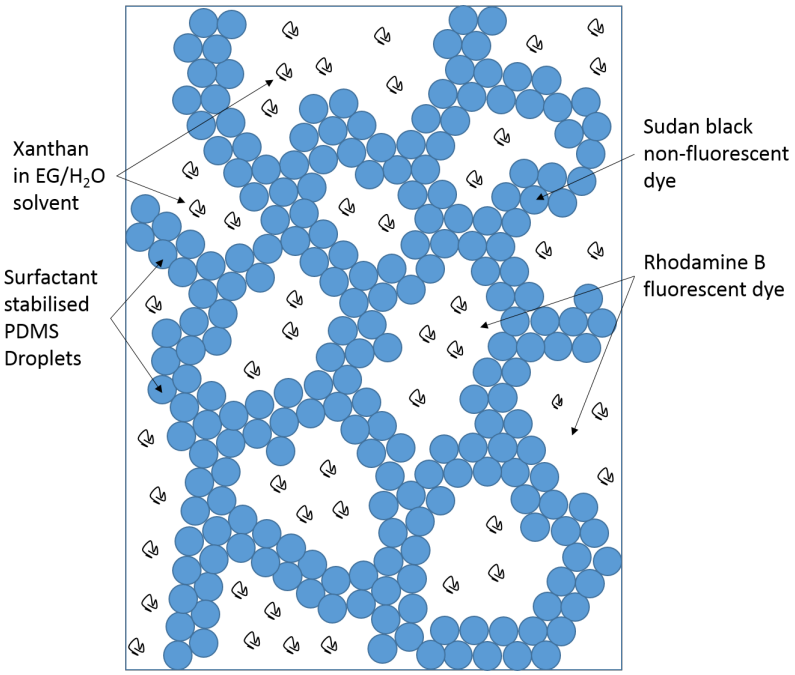

FIGURE 3.1: A diagram summarising the composition of a gel with labels showing the dyed components, the two phases present within the gel, and the space-spanning network formed by the PDMS droplets.

The samples were gently mixed in a 16 mm diameter cylindrical glass vial using a magnetic stirrer for 5 minutes, this was to ensure all samples were thoroughly mixed. Once a gel was mixed, it was transferred to a 10 x 10 mm square glass cell using a needle and syringe to minimise variation in gel heights, each gel height was approximately 20 mm.

Component	Concentration	Role
PDMS (polydimethylsiloxane)	0.2 Volume fraction	Oil Phase
EG/H_2O (61:39)	0.8 Volume fraction	Aqueous phase
Xanthan gum	0.4 - 1.0 g L^{-1}	Non-adsorbing polymer/depletant
HEC HHX	2.0 g L^{-1}	Non-adsorbing polymer/depletant
Potassium chloride	3 mM	electrostatic screening

TABLE 3.1: Gel components summary.

The phase behaviour of the xanthan-PDMS system has been previously studied by Teece et al. [25], and it was found that experimentally observed phase boundaries agreed well with the generalised free volume theory (GFVT) for colloid-polymer mixtures in the semi-dilute regime, the value for q_R used in these calculations was 0.62. The gas-crystal and gas-liquid-crystal phases were not observed experimentally, this was attributed to the polydispersity of the particles suppressing crystallisation. It was determined that with a sufficient quench into the two-phase region, gelation occurred with all samples.

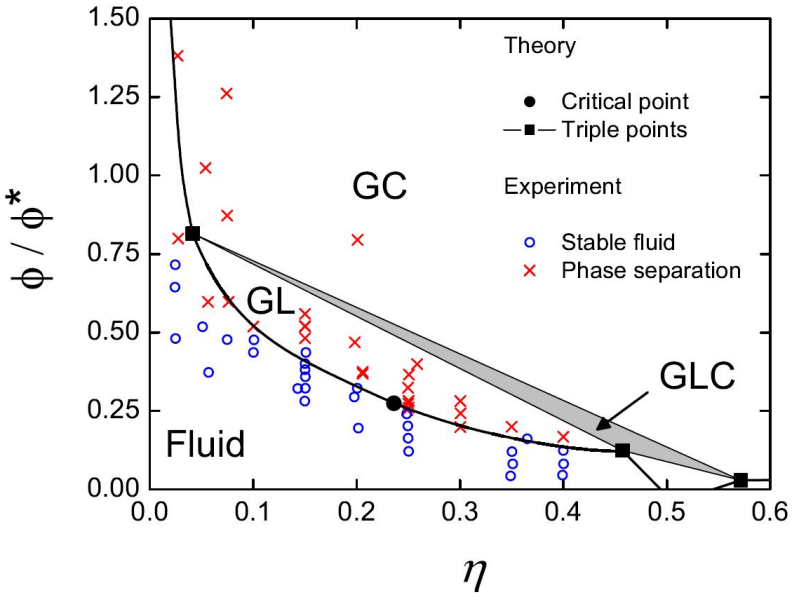

FIGURE 3.2: Phase diagram comparing experimental phase boundaries at for the xanthan-PDMS system at 20 °C, to those calculated from GFVT for $q_R = 0.62$, reproduced from [25]. With gelation occurring in samples deep within the GC region.

3.2 PDMS Droplets

The colloid chosen to form colloid-polymer gels was PDMS (polydimethylsiloxane) emulsion droplets, in an ethylene glycol and water solvent. The ethylene glycol was chosen to refractive index match to the PDMS droplets, which allowed imaging deep into the sample, the ratio of ethylene glycol to water used is 61:39 % w/w. This system was chosen as it is a well understood and simple system to model the effects of temperature on colloid-polymer gels [25, 46, 56, 87].

The PDMS used to form the droplets is silicone oil (DC200, Dow Corning) with the droplets stabilised using a combination of surfactants: PEO-PPO-PEO, M_w 4950 30 % PEO (Synperonic/Pluronic PE/P103), tristyrylphenol ethoxylate (TSPE, Tanatex) and sodium bis(2-ethyl, 1-hexyl) sulfosuccinate (Fluka, Na-AOT). The method of preparation for these PDMS droplets is detailed by Teece [25]. This mixture of surfactants is used to stabilise droplets both sterically with Synperonic, and electrostatically with Na-AOT. This high level of stabilisation gives a shelf-life of years, meaning that multiple syntheses and re-characterisation is not required. It is also prevents the xanthan polymer used from adsorbing to the droplet surface and causing a bridging interaction rather than a depletion interaction.

The droplets are prepared in a $\phi = 0.6$ stock with 10 mM of potassium chloride added to screen any electrostatic interactions between the droplets, due to the Na-AOT giving each droplet a slight negative charge. In this form, the stock solution is stable for many years. The droplets have been previously sized using Dynamic Light Scattering (DLS) and the hydrodynamic radius was found to be $a = 316 \pm 11$ nm with a polydispersity index of 0.18 [25].

3.3 Ethylene Glycol/Water Solvent

The viscosity of the ethylene glycol/water solvent was measured using capillary viscometry (as described in Section 3.5). Three measurements were made every 5 °C from 25 °C to 60 °C. This method proved extremely consistent and even at high temperatures the long elution times resulted in a small variation in the measured times, also minimising any experimental error.

To convert the measured kinematic viscosity (v) to the dynamic viscosity (η), the density of the material must be known, so the density of the EG/H_2O mix must be known to accurately calculate the viscosity at each temperature. Due to experimental limitations, there was no way to measure the density as a function of temperature, so the density was measured at approximately 23 °C using a pycnometer, giving a value of 1.0761 g cm^{-3}. In Figure 3.3a this value is compared to an interpolation of literature data [88] for 25 mol % (55 % w/w) and 50 mol % (78 % w/w) ethylene glycol and water, and is shown to be in excellent agreement.

Therefore to calculate the temperature dependence of the 61 % w/w EG/H_2O solvent, the literature data for 40 and 60 °C was interpolated to give a value for 61 % w/w. These interpolated values are fitted with a polynomial fit in Figure 3.3b to allow for a density to calculated for each temperature studied, these densities are summarised in Table 3.2. The viscosities measured for the EG/H_2O solvent are shown in Figure 3.4 and summarised in Table 3.3.

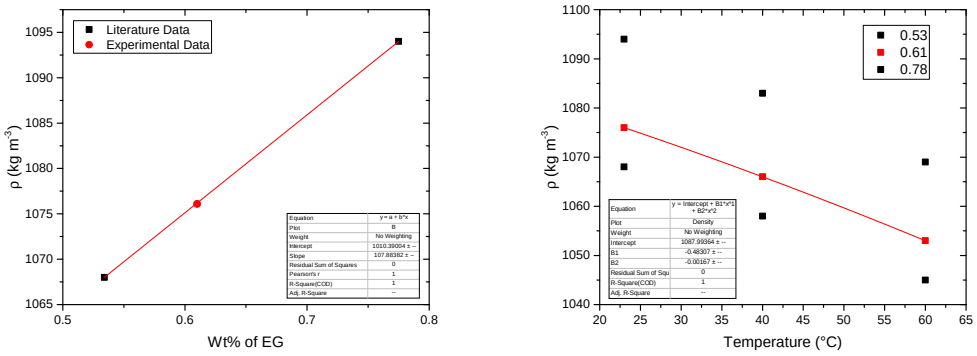

(A) (B)

FIGURE 3.3: Comparison between experimental and literature data. Literature data from [88].

Temperature (°C)	25	30	35	40	45	50	55	60
Density (g cm^{-3})	1.0749	1.0720	1.0689	1.0658	1.0626	1.0593	1.0559	1.0524

TABLE 3.2: Calculated densities from fitting in Figure 3.3.

Temperature (°C)	25	30	35	40	45	50	55	60
Viscosity (mPa.s)	4.322	3.666	3.165	2.750	2.415	2.127	1.898	1.693

TABLE 3.3: Calculated viscosities shown in Figure 3.4.

3.4 Xanthan

Xanthan gum is a large polysaccharide biopolymer named after the bacterial strain that produces it, *Xanthomonas campestris* [89]. It has a wide variety of uses in many commercial products, including a thickener/stabiliser for food stuffs (such as low fat mayonnaise), in toothpaste as a rheology modifier [90], and as a binder in glass 3D printing [91].

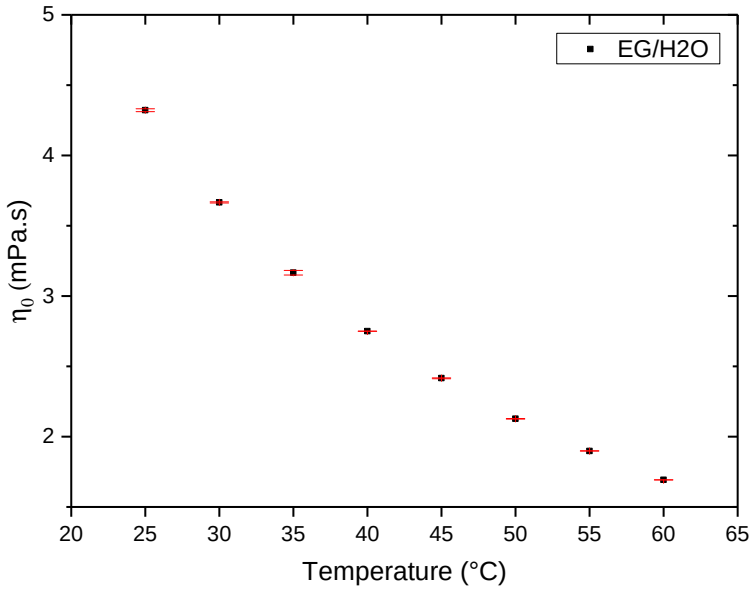

FIGURE 3.4: Calculated dynamic viscosities for a 61:39 EG/H2O solvent mixture.

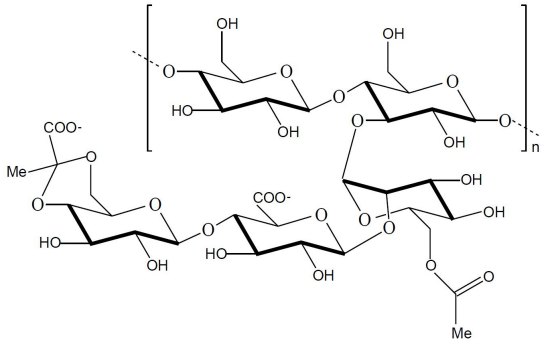

FIGURE 3.5: Chemical structure for the repeating unit of xanthan gum. Reproduced from [92].

The reason for xanthan's widespread industrial use is that only a very small amount is required to drastically change the rheological properties of a material, with many products using between 0.05 and 1 % w/w [89]. The viscosity of xanthan solutions also decrease with increasing shear-rates [93], making it well suited for stabilising gel-like products than need to retain the ability to be poured. These interesting rheological properties come about due to xanthan significant size (for a polymer), with it forming a double-helical structure similar to that of DNA [71]. This structure gives each molecule a high degree of stiffness and xanthan tends to be modelled as a worm-like chain.

Xanthan comes in a wide range of purities, molecular weights and compositions, with them varying between supplier and batch. Therefore to remove any variation between samples, one brand and batch of xanthan powder is used, namely Kelzan. This has been previously characterised by Teece et al. [25], with a molecular weight M_w of 4.66 x 10^6 g mol^{-1} and a radius of gyration R_g = 194 nm.

3.5 Xanthan Size at Different Temperatures

As previously discussed in Chapter 1, xanthan behaves in a peculiar way when heated, in that it does not gradually expand or contract like other polymers such as polystyrene [37, 94]. But it undergoes a conformation change from an ordered state to a disordered state [71], with the temperature at which this occurs depending on a wide number of factors such as salt concentration [73], molecular weight[74], and solvent.

3.5.1 Viscometry of Xanthan Solutions

With the radius of gyration of xanthan being a key factor in determining the strength of the depletion potential in our system, investigation if and how it changed with temperature was important in understanding the underlying attractions with the gel.

The capillary viscometer used (Ubbelohde, size 0B Sigma Aldrich) was calibrated using literature data on water at all temperatures studied [95]. This allowed a constant of 0.0051 mm^2 s^{-1} to convert elution time to kinematic viscosity (v) to be calculated.

The flow time of the pure solvent (t_0) was measured and then the flow time of the polymer solution (t) was measured. From this it is possible to calculate the relative viscosity η_r and the specific viscosity η_{sp}.

$$\eta_r = \frac{t}{t_0} \tag{3.1}$$

$$\eta_{sp} = \frac{t - t_0}{t_0} \tag{3.2}$$

The viscosity of xanthan polymer solutions at 20, 30, 40, 50, 60 and 80 mg L^{-1} to create a graph showing η_{sp} with respect to concentration. Using this data it is possible to estimate the intrinsic viscosity of xanthan by extrapolating the gradient of the graph back to zero.

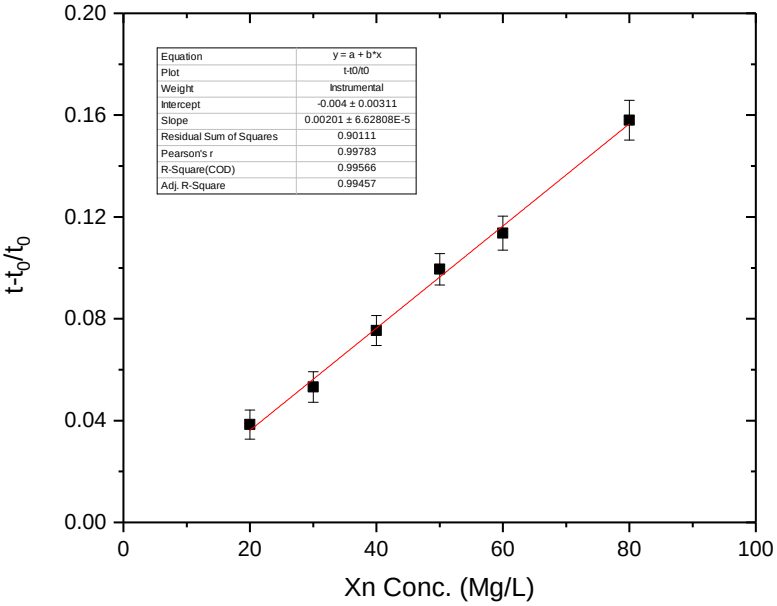

FIGURE 3.6: Plot of η_{sp} for xanthan solutions at 25 °C, with a linear fit giving the intrinsic viscosity $[\eta]$ as the gradient of the fit.

Temperature (°C)	Intrinsic Viscosity (cm^3 g^{-1})
25	2010 ± 66
30	2170 ± 75
35	2050 ± 46
40	2150 ± 139
45	2130 ± 120
50	2170 ± 63
55	2650 ± 32
60	2850 ± 41

TABLE 3.4: Measured intrinsic viscosity $[\eta]$ using capillary viscometry for each temperature studied.

Table 3.4 summarises the measured intrinsic viscosity of xanthan in EG/H_2O for each temperature studied, calculated from a plot of η_{sp} against xanthan concentration (Figure 3.6 shows this at 25 °C, other temperatures can be found in Section 3.7). Comparing just the intrinsic viscosities, there is a slight fluctuation with temperature,

up to 50 °C, once the error in the value of $[\eta]$ is accounted for, there little to no change. However at 55 and 60 °C there is a significant increase in $[\eta]$.

3.5.2 Theory for R_g Calculations

In this section we summarise the calculations performed to convert the measured intrinsic viscosity $[\eta]$ of xanthan to a radius of gyration R_g between 25 and 60 °C. We will use the intrinsic viscosity measured to calculate a Kuhn length (λ^{-1}), which then will be used to calculate a persistence length and a radius of gyration R_g for xanthan at that temperature. The assumptions in these calculations are that the mass per unit contour length M_L is unchanged with solvent and temperature due to it depending on the chemical structure of the xanthan backbone. Also, that the changing temperature will not affect the interactions between xanthan chains due to $[\eta]_0$ being in the infinitely dilute regime.

$$[\eta] = \lim_{c \to 0} \frac{\eta_{sp}}{c} \tag{3.3}$$

The unreduced intrinsic viscosity of a worm-like chain in a Θ solvent (so that the polymer conformation is unperturbed) is given below in Equation 3.4 [96].

$$[\eta]_0 = \frac{\Phi_0 L_r^{\frac{3}{2}} (\lambda^{-1})^3}{M} \tag{3.4}$$

Where $[\eta]_0$ (in $cm^3\ g^{-1}$) is the intrinsic viscosity of a configuration unperturbed by excluded volume effects. Φ_0 is the viscosity function, which is dependent on L_r, the reduced contour length, and d_r, the reduced diameter. When $L_r = \infty$, $[\eta]_0$ becomes $[\eta]_\infty$ and is independent of d_r and equal to 2.87 x 10^{23}. Which can be rearranged into the form shown below, where $F_1 = \Phi_0/\Phi_\infty$.

$$[\eta]_0 = \left[\Phi_\infty M^{\frac{1}{2}} \frac{1}{(\lambda M_L)^{\frac{3}{2}}} \right] F_1 (L_r, d_r) \tag{3.5}$$

The radius of gyration for a monodisperse polymer of molecular mass M modelled as a wormlike chain can be calculated using Equation **??** [97]. Where $x = L/q$ and q

is the persistence length calculated from $q = \lambda/2$.

$$R_g^2 = q^2 \left[\frac{x}{3} - 1 + \frac{2}{x} - \frac{2}{x^2}(1 - \exp(-x)) \right] \tag{3.6}$$

However many polymers are not monodisperse, so the polydispersity of a polymer must be taken into account when calculating the radius of gyration, as neglecting the polydispersity of the polymers tends to lead to an overestimation of chain stiffness. The polydisperse radius of gyration is given below in equation 3.6 [98].

$$\langle R_g^2 \rangle = \frac{m+2}{6y\lambda} - \frac{1}{4\lambda^2} + \frac{y}{4(m+1)\lambda^4} - \frac{1}{8m(m+1)\lambda^4} \left(y^2 - \frac{y^{m+2}}{(y+2\lambda)^m} \right) \tag{3.7}$$

Here $y = (m+1)/L$, with L being the contour length of the chain and using $L = M/M_L$ m can be equated to $m = 1/(M_w/M_n - 1)$.

By using Equation 3.5 and a measured intrinsic viscosity it will be possible to calculate the Kuhn length λ^{-1} which can then be inserted into Equation 3.6 to calculate the radius of gyration. By performing the measurements of the intrinsic viscosity at different temperatures and then calculating the radius of gyration from these intrinsic viscosities we are able to gain insight into how the radius of gyration of xanthan changes with respect to temperature.

Temperature (°C)	Intrinsic Viscosity (cm^3g^{-1})	Radius of Gyration (nm)
25	2010 ± 66	182 ± 3
30	2170 ± 75	189 ± 3
35	2050 ± 46	184 ± 2
40	2150 ± 139	188 ± 5
45	2130 ± 120	187 ± 4
50	2170 ± 63	189 ± 2
55	2650 ± 32	206 ± 1
60	2850 ± 41	213 ± 1

TABLE 3.5: Measured intrinsic viscosity $[\eta]$ using capillary viscometry for each temperature studied, with the R_g calculated from the corresponding intrinsic viscosity.

When the values for $[\eta]$ are used to calculate a value for R_g at that temperature, it

is clear that firstly, the errors in the measurement are very good, as they only equate to a few nm, and also that the fluctuations below 55 °C again are only of order a few nm, which due to the nature of xanthan, and the time taken to collect all the elution times, indicate no expansion or contraction caused by changing temperature. Whilst it appears that at 55 °C xanthan begins to expand, this may not necessarily be the case. As Milas et al. [73] show that when the conformation of xanthan changes there is an increase in intrinsic viscosity but the radius of gyration decreases despite this (shown in Figure 1.26). This suggests that at 55 °C the conformation of xanthan begins to change, but further characterisation is required to ascertain the size of xanthan at 55 and 60 °C, as the current model assumes that xanthan is a wormlike chain.

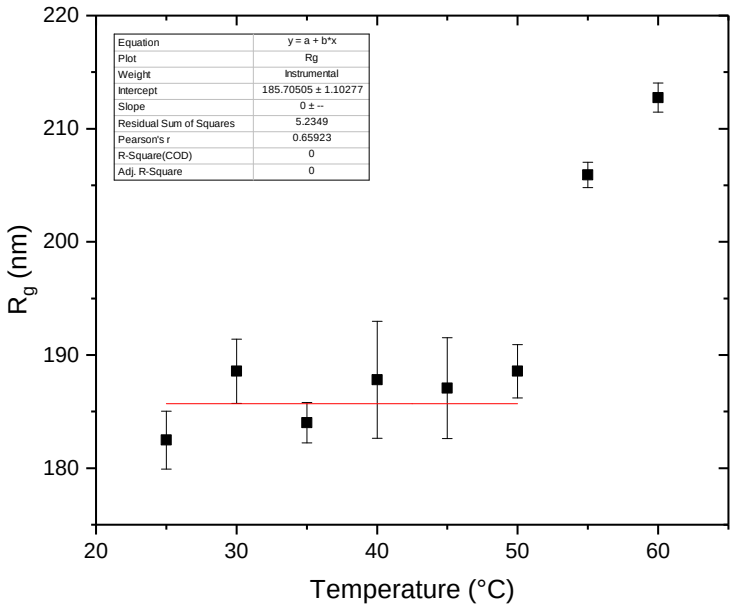

FIGURE 3.7: Plot calculated xanthan R_g for each temperature from the capillary viscometry data shown in Section 3.7.

When the average of all sizes from 25 - 50 °C is calculated a final number of 186 ± 8 nm is found (shown in Figure 3.7). Which is within the error for the value 194 ± 10 previously calculated by Teece et al. [25]. As the value given by Teece takes into account both viscometry and light scattering, that value was used for calculating both the depletion potential and Kramer's escape time.

3.6 Hydroxyethylcellulose (HEC)

The second polymer depletant used is Hydroxyethylcellulose (HEC), specifically Natrosol 250 HHX, so will be referred to as HEC HHX. The molecular weight of HEC HHX has been previously measured by Zhang, and determined to be 1.3 x 10^6 [87], as well as the radius of gyration, with R_g = 126 nm. When paired with the PDMS droplets described above this gives a colloid-polymer ratio of 0.40, a shorter but stronger depletion attraction when compared to using xanthan.

3.7 Capillary Viscometry Graphs and Fits

In this section the capillary viscometry data used to calculate R_g for xanthan at each temperature is summarised.

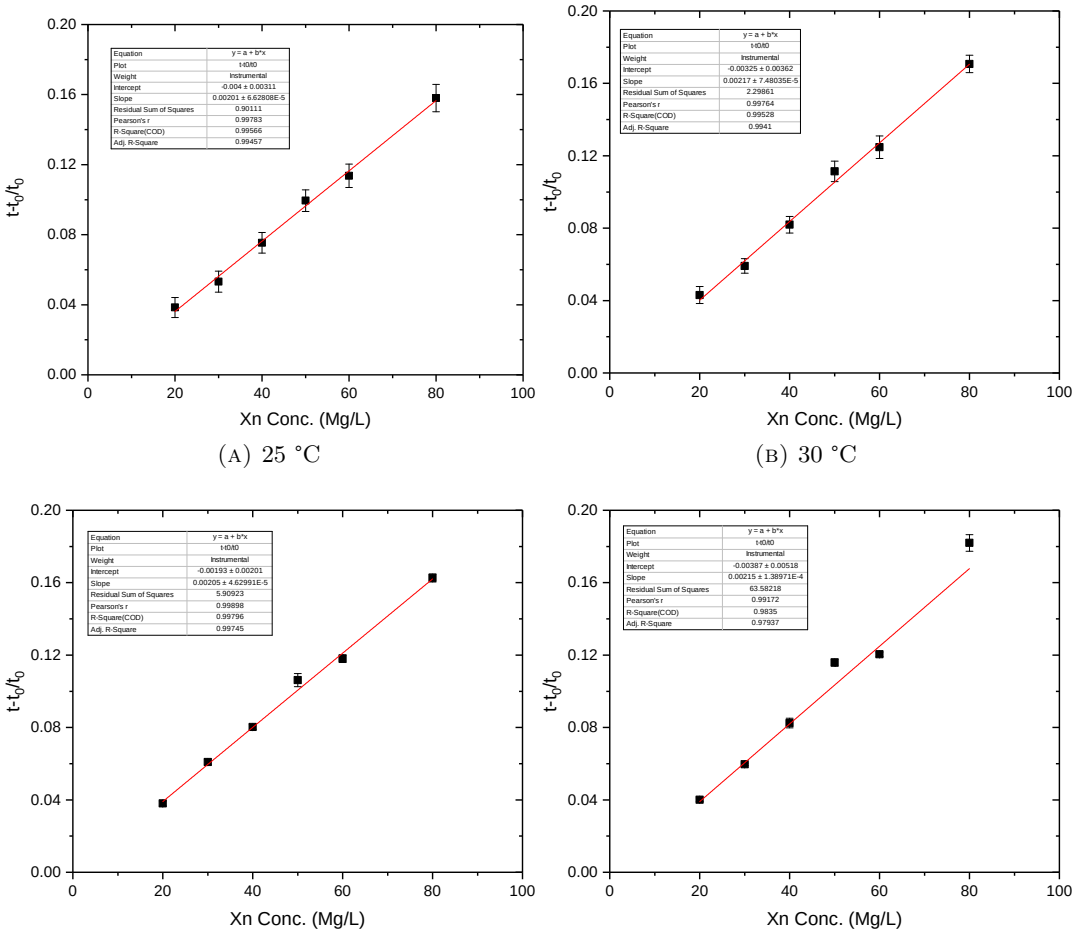

(A) 25 °C (B) 30 °C

(C) 35 °C (D) 40 °C

FIGURE 3.8: Capillary viscometry data of xanthan solutions in EG/H_2O between 25 and 40 °C.

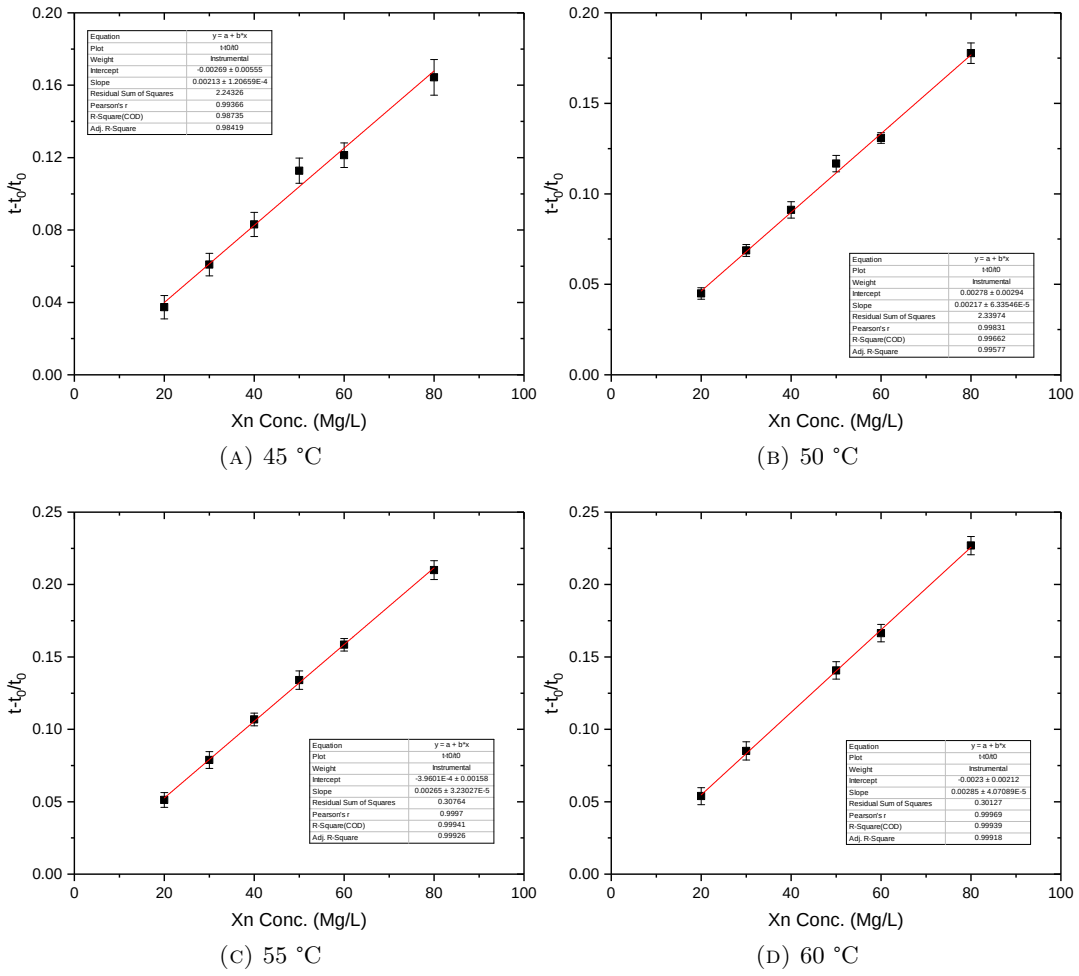

(A) 45 °C (B) 50 °C

(C) 55 °C (D) 60 °C

FIGURE 3.9: Capillary viscometry data of xanthan solutions in EG/H_2O between 45 and 60 °C.

Chapter 4

Delayed Collapse at Ambient Temperature

In this chapter, we discuss literature on studying colloid-polymer gels at room temperature, such as various methods used, different collapse mechanisms as well as industrial challenges faced with the stability of formulations. We then present delay time data on a model colloid-polymer gel, studied at a single temperature, and explore the effect of increasing polymer concentration on the gel lifetime. We compare the macroscopic behaviours of a gel to the bond lifetime τ_{esc}, in an attempt to bridge both long and short time-scales present in colloid-polymer gels.

4.1 Introduction

When studying a formulation's shelf life, there are many things to consider when answering the question of "is this product stable enough?" with the enough definitely being a key caveat of that question. As why over-engineer a product to be stable for years when it is used a week after production? Some key things to consider are:

- How long a formulation is stable for?
- How consistent is the formulation stability?
- How robust is the formulation with respect to environmental conditions? Such as temperature or vibration/movement.
- What is the mechanism of collapse?
- How slowly does the formulation sediment?

- Can a formulation be re-suspended after collapse?

A way of measuring the stability of a formulation is to measure the time taken for it to macroscopically change, for example in the system used for this work, for the gel to phase separate, but in other systems both academic and industrial other forms of collapse have been observed. Such as Ostwald ripening of emulsion droplets, sedimentation of a suspended medium or the significant thickening of a liquid based product. Understanding the mechanism of collapse is also of great importance, with the main two mechanisms seen in colloidal gels being delayed collapse, in which no macroscopic movement is observed before catastrophic collapse occurs, and Buscall-White sedimentation [99], in which there is no delay period, but a gradual (or less so) consolidation of particles in a suspension or gel.

Once the mechanism of collapse is understood then the question of how long the sample takes to collapse can be answered, as if it slowly sediments akin to that seen by Buscall and White, this may be in fact a more useful time-scale to determine a shelf-life of a product, where as with delayed collapse, it is less important as the formulation has already failed.

Finally, if a formulation can be re-suspended easily and to a good level of dispersion, then perhaps the drive for a longer shelf-life may not be as critical as first thought. However this is not often the case, as some formulations can form a dense sludge at the bottom of the container than no matter how hard you shake, either cannot be dislodged, or the material cannot be equally dispersed, which is somewhat less than ideal if your active ingredient is the dispersed medium. Nobody wants to wants to kill one field of crops with pesticide, only to lose the other field of crops because you sprayed it and there was little to no active ingredient in the second half of your pack. Therefore in this chapter we endeavour to discuss some of the methods used to answer some of these questions surrounding formulation stability, before exploring how changing temperature can affect one of more of these factors in determining a formulations lifespan.

4.2 Review

4.2.1 Studying Delayed Collapse

The most common method used to study the lifetime of a colloid-polymer gel involves observing for any macroscopic change using a digital camera [25, 55, 62] with a variety of methods used to determine interface height, including a vernier scale, or image thresholding to determine an interface. This technique is valuable in determining two of the questions above, when and how does a sample collapse, as distinct profiles are generated with delayed collapse and so called creeping collapse. How long a sample takes to collapse can also be observed by measuring the interface height after delayed collapse is observed. This would be a viable method for measurements in industry, were it not for the significantly longer time-scales present in industrial formulations, with many products needing to be stable for months not years. Whereas most academically studied systems have a significantly shorter delay time. With some examples being: 2 - 8 hours [55], 6 hours [54], 10 hours [62], 4 - 80 hours [46], and 20 - 100 hours [100]. However with τ_d being only the first major time relevant to the lifetime of a formulation, it is easy to see how full capturing the lifespan of a system could take three or even four times as much time. Which with industrial systems rapidly becomes infeasible. Hence the great interest in accelerating the ageing of formulations as well as looking for early indicators of a gels lifetime before macroscopic collapse is observed.

A method used by Poon et al. [54] is dark field microscopy with a refractive index matched sample, where only weakly scattered light is detected, and unscattered light is filtered out. Examples of which can be seen in Figure 4.1. In Figure 4.1 the images that are taken around τ_d are g and h, with all images before being taken before an interface forms and sedimentation begins. It is here that the advantage dark field imaging has over digital microscopy is see, with the wealth of information collected prior to collapse. In images c, d, and e, it is possible to see the formation and growth of a light line on the left-hand side of the sample, which Poon describes as a channel forming within the gel which allows solvent to travel. Looking further at later images (g, h, and i) it is possible to see how this channel formed at early times in the gels life (approx. 0.3 - 0.5 τ_d) can lead to the total failure of a sample, with significant

channel formation both sufficiently disrupting the space-spanning network of the gel as well as giving sufficient space for solvent to move as the sample collapses.

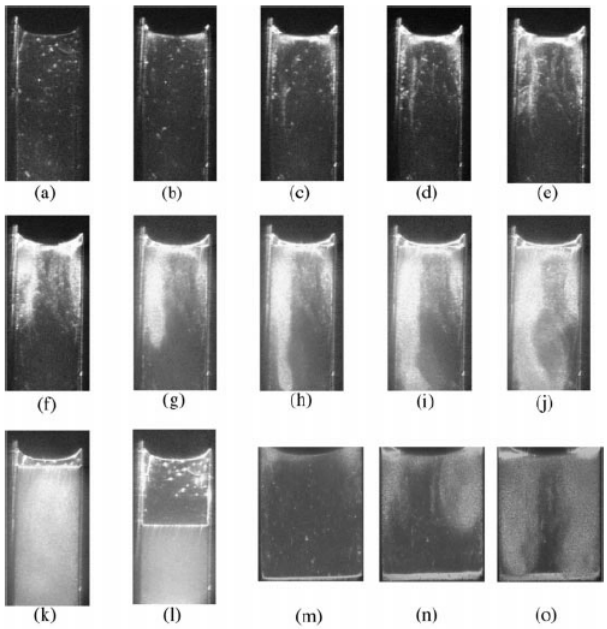

FIGURE 4.1: Dark field images of a colloid-polymer gel (R = 186 nm, $\phi = 0.2$, and $\xi \sim 0.08$). Reproduced from [54].

4.2.2 Studies on Creeping Collapse

Starrs et al. [51] explore gels that undergo creeping collapse, again using dark field microscopy. Figure 4.2 shows dark field images of a sample as it undergoes creeping collapse, so there is delay period before rapid collapse. It is clear to see that when compared to Figure 4.1 there is a dramatic change in mesoscopic features present within the sample (the light areas of the images). There does not appear to be the same channel formation as seen in delayed collapse at early times, however once the gel has begun to sediment (image c) these channels or cracks within the gel appear (images e and f) towards the bottom of the sample, and appear to propagate from the walls of the sample. There is a symmetrical nature to the cracks that form for the creeping collapse sample whereas in the delayed-collapse sample, the main channel appears down the left-hand side.

However, most industrial products are not refractive index matched as shown by the simplified model formulations in Figure 1.1. So dark field microscopy can not be easily applied to explore pre-collapse behaviours of many systems, however

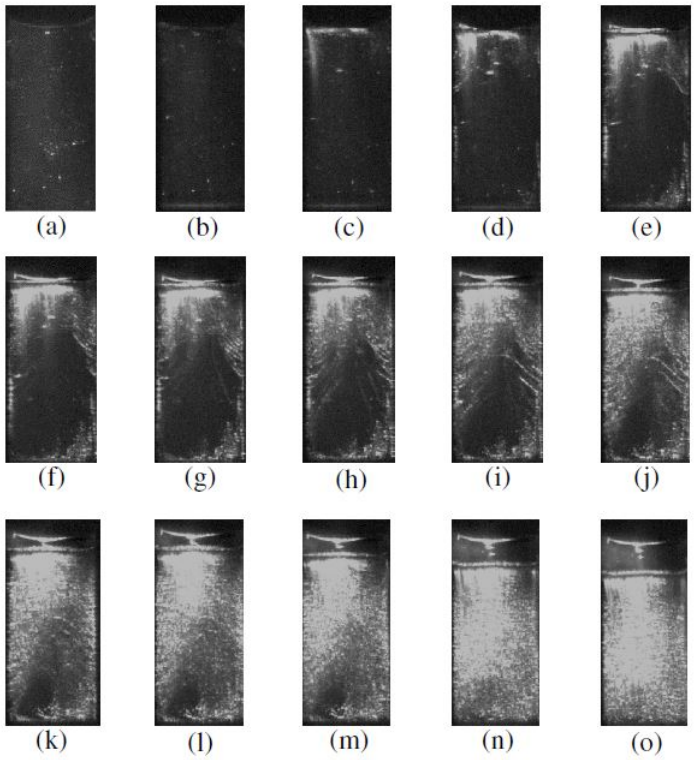

FIGURE 4.2: Dark field images of a colloid-polymer gel (R = 186 nm, $\phi = 0.2$, and $\xi \sim 0.1$). Reproduced from [51].

similar delayed collapse behaviour is found in drastically different systems [101], so one would expect similar pre-collapse features to be present. Despite this limitation, the features seen at early times in a formulations lifetime can be probed using other methods that work in opaque systems such as using x-rays to probe for movement of colloidal particles, or through the use of fluorescent tracer beads.

4.2.3 Settling Dynamics

Returning to the data collectable through digital imaging, a great deal of information has been collated on how quickly a sample collapses after τ_d for delayed collapse, or how quickly a suspension sediments for creeping collapse. Studying height profiles for sedimenting materials is not just relevant to formulation stability but also to a great variety of real world applications such as waste water treatment [102] and separation of nuclear waste sludge [103]. Bartlett et al.[46] find that the settling rate Δh ($\Delta = h_0 - h$) scales well with the fit of $\Delta h \sim \tau^{3/2}$ for both a wide range of gel concentrations as well as different sample heights (h_0). However studying a single concentration at varying sample heights, Bartlett et al. finds that whilst τ_d remains

the same, the rapid collapse portion becomes extended from 3x τ_d at low heights (20 mm) to 5x τ_d at high heights (60 mm), presumably due to the increased amount of solvent and colloids that must move as the gel phase separates.

Kilfoil et al. [100] study the delayed sedimentation of 0.5 μm silica and carboxymethylcellulose (CMC) between C_p = 0.087 wt% and 1.5 wt%, and find a different scaling value to that of Bartlett et al. for the interface height during rapid collapse. They find a similar scaling with polymer concentration to that of Bartlett et al. $\tau \sim \tau_0 \exp(\beta C_p)$, but the rapid collapse portion of collapse varies between 1 and 3 τ. It should also be noted that similar to Starrs et al. [51] there appears to be a crossover to creeping sedimentation, but when all the data present is scaled onto a master curve, there is good overlap of all height profiles, so in fact is it just incredibly slow "rapid" collapse.

4.2.4 Height and Shape Effects

A complex picture arises when assessing the height and width dependence of a gels lifetime, with Starrs et al. [51] finding both width and height dependent regimes, as well as height independent regimes for the same gel system. They attribute this behaviour to when the width and height are above a characteristic length-scale of the network that τ_d becomes height independent. Kim et al. [104] show how controlling the height of a sample can also determine if a delay period before collapse is observed, with tall samples exhibiting delayed-collapse and shorter samples collapsing via creeping sedimentation. Bartlett et al. [46] find no height dependence in τ_d and also find that at all heights studied there is no crossover to creeping collapse as seen elsewhere. This complex and at times contradictory behaviour of different height samples has been attributed to a change in the gravitational stress put onto the network as well as the shape of the meniscus having a large impact upon the sedimentation behaviour of a gel. This dependence on the meniscus may well explain the height independent behaviour found by Bartlett et al. as the gel system studied creams rather than sediments, therefore the "top" of the gel network is actually at the bottom of the sample vial.

With regards to an industrial formulation, the challenges faced due to this height, width and shape behaviour in gel lifetimes can become extraordinary, especially when

you consider the multitude of different ways a product can be delivered. Even with something relatively mundane as hair products, pack size can vary, from larger tubs for greater value to small one-use sachets for samples (arguably the worst situation to have stability problems in). Moving to larger scale products such as pesticides, again pack size can vary to an even greater degree, with some only requiring a small sachet, to 20 L concentrates for spraying, to even tanker loads of product, which touches again on another issue faced by industry, a product must remain stable at every point during production, on top of when it has to sit on a shelf somewhere.

With this in mind, the next sections will focus on understanding the macroscopic characteristics of a model colloid-polymer gel, predominantly the delay time before collapse (τ_d).

4.3 Results - Delay Time Before Collapse

Using the model gel system described in Chapter 3, consisting of PDMS droplets($a =$ 316 nm) suspended in an EG/H_2O solvent, with the polymer xanthan ($R_g = 194$ nm) added to induce a depletion attraction between the PDMS droplets, the macroscopic collapse of gels is measured. Four samples are individually prepared by mixing the PDMS emulsion with a xanthan in EG/H_2O solution to give a final colloid volume fraction of $\phi = 0.2$. Each sample is then loaded into a cell in the cell-holder using a needle and syringe to ensure a consistent height of $\sim$ 20 mm and to minimise bubbles in the samples and at the meniscus.

The image stacks generated were analysed as described in Section 2.3.2 and the delay time identified for each gel at 25 °C, the average of the delay times, and the standard deviation calculated to show the variation in τ_d. An example of the raw data from which this was calculated can be found in Figure 2.9. The standard deviation varied between 5 and 20 % of the average, with most errors being around 10 %, this is similar to the 14 % seen previously in this system [56] as well as other colloidal gels [60].

Figure 4.3 shows the delay times measured for xanthan-PDMS gels at 25 °C. With concentrations between 0.4 and 1.0 g L^{-1}, which gives a range of 1.6 to 4.0 C_p/C_p^*. τ_d varies between $\sim$ 20000 s (5.5 hours) to $\sim$ 70000 s (8 days) showing that a linear

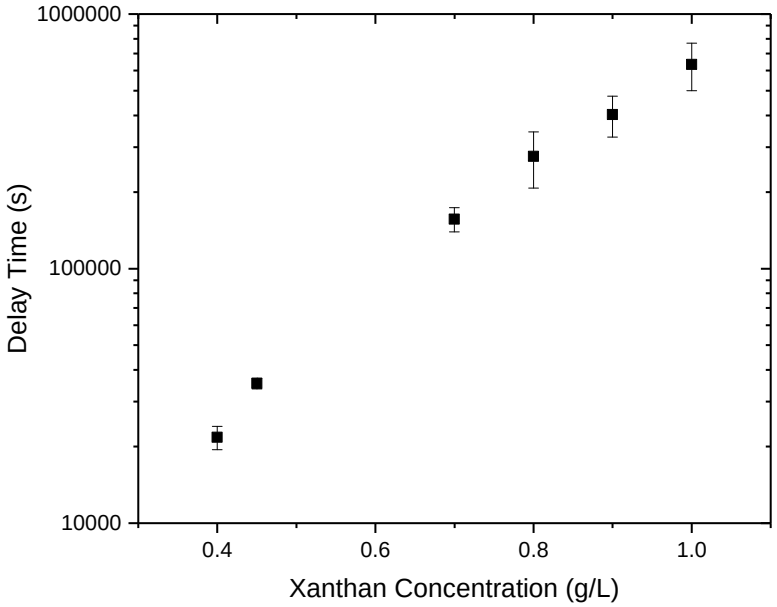

FIGURE 4.3: Delay times of gels with a range of xanthan concentrations, measured at 25 °C.

increase in xanthan concentration gives a substantial increase in gel stability. Each xanthan concentration gives a discrete cluster of τ_d values with only a slight overlap occurring between 0.8 and 0.9 g L^{-1}.

Comparing these delay times to room temperature measurements made previously using the same system, Teece [105] measures lower values, approximately 1/3rd of the values measured here, this significant difference in τ_d is attributed to the different shape of the cell used, with Teece using a cylindrical cell. Despite this difference in τ_d, the same exponential dependence on xanthan concentration C_p is still observed. More recently, Gilligan [106] used the same rectangular cells as used in this work and found delay times again lower than those presented here, despite a similar preparation method. Therefore when considering the reasonable variance previously displayed in the lifetime of colloid-polymer gels, the main difference between the results of Gilligan and those presented here are the level of control of temperature. With the temperature control (air conditioning) used, only giving a temperature stability of 20 ± 2 °C. Using a similar system of HEC HHX and PDMS ($a = 272$ nm) gels, with R_g/a = 0.45, a temperature variation of 0.4 °C [107] gives rise to a log normal distribution with an average of 33000 s and a range of 20000 to 40000 s. This effect from only a 0.4 °C temperature difference gives insight into the drastic effect of temperature observed later in this work. This increase in τ_d coming about due to the decrease variation

in temperature (less than 0.1 °C, as shown in Chapter 3) is due to reduced internal temperature variation within the sample. A higher level of temperature variation within a sample will lead to a greater degree of internal stress, caused by differing levels of coarsening and particle motion.

4.4 Discussion - Particle Dynamics

Previous work has been done exploring the link between the Kramer's escape time (τ_{esc}) and the delay time before gel collapse (τ_d), Bartlett et al. [46] estimated τ_{esc} using the limiting low shear viscosity η_L, and found that τ_d correlated strongly with 240 x τ_{esc} (shown in Figure 1.20). Therefore we will calculate τ_{esc} at 25 °C using the EG/H_2O viscosity and compare these escape times to the delay times shown above.

4.4.1 Calculating Particle Escape

$$\frac{-U_0}{k_BT} = q_s^2\left(q_s + \frac{3}{2}\right)q_R^{-3}y(1 + 3.77y^{1.31}) \tag{4.1}$$

Using Equation 4.1 (previously shown in Chapter 1), the strength of the depletion potential at a range of xanthan concentrations is calculated and is plotted in Figure 4.4. There is a clear linear trend between depletion potential strength and xanthan concentration. These depletion potentials are also summarised in Table 4.1. Using the viscosities of the EG/H_2O solvent shown in Table 3.3, the xanthan size measure by Bartlett et al. [46] and the calculated depletion potentials, the Kramer's escape time for a range of xanthan concentrations is calculated and shown in Figure 4.5.

Xanthan Conc.	0.4 g L^{-1}	0.45 g L^{-1}	0.7 g L^{-1}	0.8 g L^{-1}	0.9 g L^{-1}	1.0 g L^{-1}
$-U_0/k_BT$	4.23	4.68	6.88	7.74	8.59	9.43

TABLE 4.1: Calculated depletion potentials for a range of xanthan concentration.

$$\tau_{esc} = \frac{\delta^2}{D_t}\frac{\exp(-U_0/k_BT) - (1 - U_0/k_BT)}{(U_0/k_BT)^2} \tag{4.2}$$

$$D_0 = \frac{k_BT}{6\pi\eta_L\alpha} \tag{4.3}$$

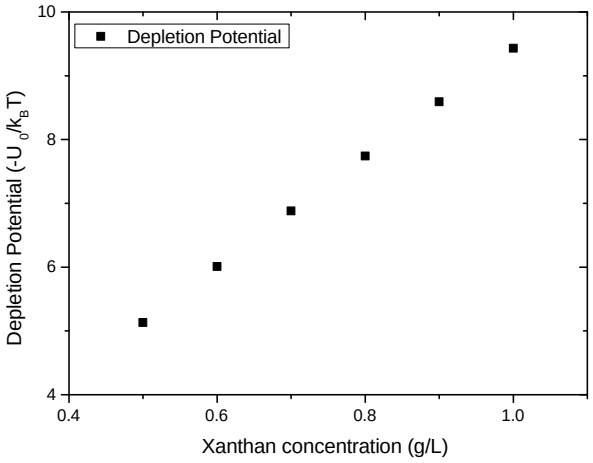

FIGURE 4.4: Calculated depletion potential for a range of xanthan concentrations.

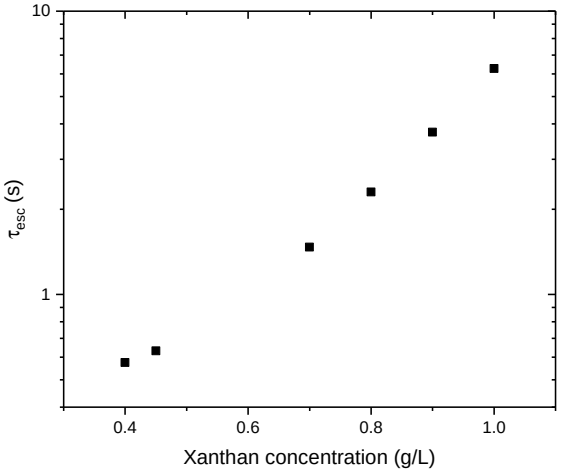

FIGURE 4.5: Calculated τ_{esc} from Equation 4.2, using η_0 in Equation 4.3 (both previously shown in Chapter 1). At 25 °C for C_p 0.4 - 1.0 g L^{-1}.

4.4.2 Comparing Long and Short Time-scales

Figure 4.6 compares τ_d and τ_{esc} for all the xanthan concentrations studied at 25 °C. The strong correlation between τ_d and τ_{esc} previously seen by Bartlett et al. [46] is observed, however there is around three orders of magnitude between τ_d and τ_{esc} compared to $\tau_d \sim 240$ x τ_{esc}. This significant difference in values comes about due to two reasons, with the first being that the τ_{esc} calculated by Bartlett et al. use the polymer viscosity η_L where as the τ_{esc} values calculated in Figure 5.9 use the solvent viscosity η_0, an example of how drastic a difference this choice of viscosity is, for a 1.0 g L^{-1} (4.0 C_p/C_p^*) using η_L gives an escape time of 1000 s whereas using η_0 gives

an escape time of $\sim$ 10 s. The second reason for this is the measurements of τ_d were previously measured in cylindrical vials not rectangular vials, previously the shape of a vial has been found to affect delay time, with a cylindrical vial giving a lower delay time than a rectangular vial [105].

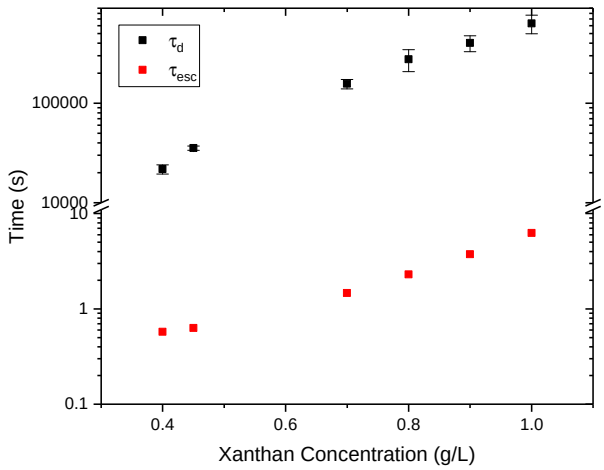

FIGURE 4.6: τ_d and τ_{esc} plotted for gels at various concentrations of C_p at 25 °C.

Table 4.2 and Figure 4.7 summarise the ratio of τ_d/τ_{esc} for each xanthan concentration studied at 25 °C. With the error arising from the standard deviation in the measurements of τ_d due to the stochastic nature of gel collapse, rather than variability in sample preparation. It appears that at low xanthan concentrations, the ratio seems to increase in a linear fashion, seen between 0.4 and 0.7 g L^{-1}, however the ratio of τ_d/τ_{esc} seems to be similar for gels between 0.7 and 1.0 g L^{-1} as it plateaus, suggesting that at a single temperature, (25 °C in this case) delay time does scale strongly with the Kramer's escape time.

Gel Conc. g L^{-1}	0.4	0.45	0.7	0.8	0.9	1.0
τ_d/τ_{esc}	37794	56020	106565	119980	107629	101103
St.Dev (±)	3996	2653	11545	29817	19640	21413

TABLE 4.2: The ratio between τ_d and τ_{esc} at 25 °C.

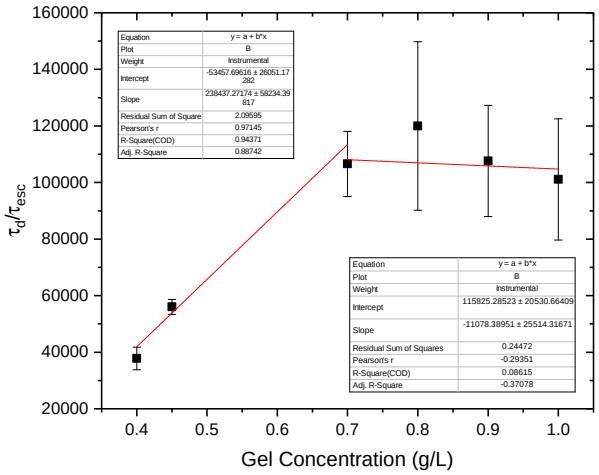

FIGURE 4.7: Ratio between τ_d and τ_{esc} at 25 °C for gels between C_p 0.4 - 1.0 g L^{-1}.

4.5 Summary

In this chapter we have explored the methods of measuring the delayed collapse phenomenon seen in colloid-polymer systems, as well their relevance to studying the stability of industrial formulations. We have also discussed the second type of gel collapse seen, creeping collapse/sedimentation, and some of the parameters that appear to control whether a system exhibits creeping or delayed collapse.

We have then shown data on a model colloid-polymer system, using the polymer xanthan to form a depletion interaction between the PDMS drops. We have compared measurements of the delay time τ_d to others made using this system, and find that the τ_d measurements made in this thesis are consistently higher than those previously made due to a slightly different preparation method and a different shaped vial used to hold the samples when comparing to the work of Teece. When comparing the values of τ_d to those of Gilligan, we find that the higher level of temperature control used with our measurements increases the value of τ_d measured for the same system and vial shape.

By considering previous work linking single bond rearrangements to the lifetime of a gel, we calculate τ_{esc} using the solvent viscosity η_0. We find that τ_{esc} and τ_d scale well, even at very low polymer concentrations, with the ratio τ_d/τ_{esc} being mostly concentration independent. The ratio calculated is significantly larger than that of Teece, due to the lower τ_{esc} value calculated from solvent rather than polymer viscosity, and the larger τ_d we measure.

Chapter 5

The Effect of Temperature on Gel Collapse

In this chapter, we explore the effect of temperature on the delay time τ_d, finding that up to 45 °C, increasing temperature drastically reduces the time before collapse, whilst above 45 °C the effect of temperature is lessened. We compare this change in τ_d to the change in τ_{esc},which arises predominantly due to the effect of temperature on the solvent viscosity, but find that an increased rate of particle-particle bond breakage is not sufficient to explain the trend in τ_d observed. We then explore whether temperature affects the settling dynamic of the gel after collapse, finding little change with temperature. Finally we present preliminary data using a shorter range depletion interaction, finding that despite a drastically different depletion range and strength, increasing temperature still yields a significant reduction in τ_d.

5.1 Introduction

As discussed in Chapter 1, changing the temperature of a formulation is a common method in industry to test the stability of a product. This is often done either through storing the product at a higher temperature, or by cycling the temperature between hot and cold. However, despite this common use in industry, there has been little study of the effect of temperature on colloid-polymer gels in academic research. Most previous research has focused on how changing temperature can affect the phase behaviour of a colloid-polymer system, due to the changing size of the polymer [37, 39].

The phase behaviour change due to changing polymer size can be mitigated by using the polymer xanthan. Xanthan does not gradually expand or contract as temperature is increased (as shown in Chapter 3), so is an excellent polymer to use whilst avoiding the changing phase diagram found with polymers such as polystyrene. Furthermore, as xanthan remains the same size, the depletion attraction generated due to it remains linear in temperature, as the depth and range of the potential remain the same. As the depletion potential is often described in units of k_BT, the linear dependence with temperature is scaled out, meaning that the scaled depletion potential becomes temperature independent.

In this chapter we will present collapse data between 25 and 60 °C, analogous to the way that industrial formulations are stored at higher temperatures to test stability, with an aim to see if the accelerated collapse seen in complex systems is observed in our relatively simple model colloid-polymer gel. We then discuss the response to temperature of the delay time τ_d and interpret the raw data as an Arrhenius like activated process. Following this we begin to add layers of complexity to a model to explain the collapse behaviour observed. We scale τ_d with the two extremes of viscosity that a single particle is exposed to during gel ageing, the solvent viscosity η_0 and the polymer viscosity η_L. Once the appropriate scaling has been found, the relevant viscosity is used to calculate the rate of particle-particle bond breakage at each temperature and gel concentration, allowing the particle dynamics of the system to be scaled out. This gives an insight into whether the previous assertions at ambient temperature, that gel collapse is governed by the rate of particle-particle bond breakage [33, 46, 54, 55, 61] still holds true over a wide range of temperatures.

5.2 Results - The Effect of Temperature on Delay Time

Using the same method as Chapter 4, the samples were prepared by mixing the PDMS emulsion (a = 316 nm) with a xanthan (R_g = 194 nm) in EG/H_2O (61 % w/w) solution to give a final colloid volume fraction of $\phi = 0.2$. Each sample is then loaded into a cell in the cell-holder using a needle and syringe to ensure a consistent height of $\sim$ 20 mm and to minimise bubbles in the samples and at the meniscus. After

the samples are loaded into the cell-holder, the temperature of the circulating water-bath is set to the desired temperature as quickly as possible to ensure consistency throughout all the experiments performed.

The image stacks generated were analysed as described in Section 2.3.2. With the delay time identified for each gel at different temperatures, the average of the delay times at each temperature was taken, and the standard deviation calculated to show the variation in delay times at each temperature. The standard deviation varied between 5 and 20 % of the average, with temperature having no significant effect on the magnitude of the errors observed.

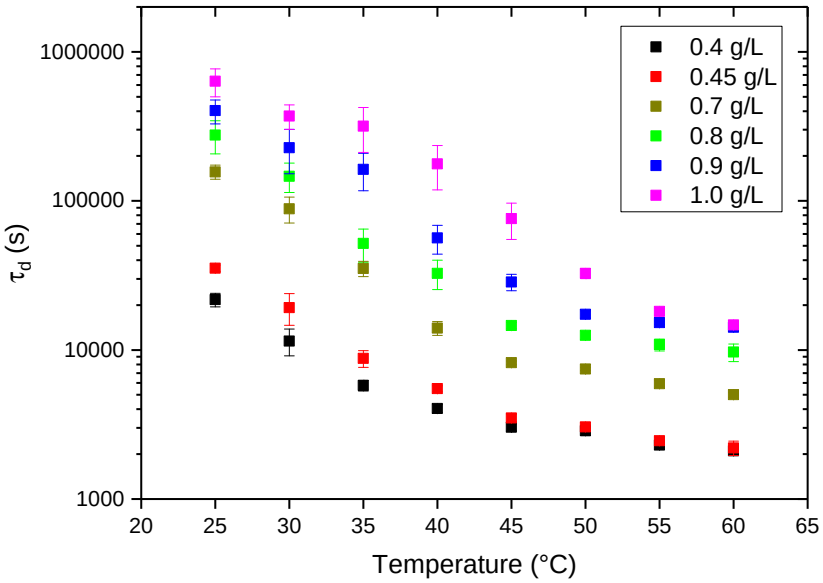

FIGURE 5.1: Delay times of gels with a range of xanthan concentrations, measured at different temperatures.

Figure 5.1 shows the delay times measured for xanthan-PDMS gels between 0.4 and 1.0 g L^{-1}, which gives a concentration range of 1.6 to 4.0 C_p/C_p^*. Each gel concentration gives a discrete cluster of τ_d values with only a slight overlap occurring between 0.8 and 0.9 g L^{-1}. As temperature is increased, there is also minimal overlap between gel concentrations, with 30 °C seeing the greatest amount of overlap, however this appears due to the larger error in the 0.9 g L^{-1} value.

As temperature is further increased, an exponential decrease in τ_d is observed for all gels, appearing to be a similar rate despite the two orders of magnitude difference in τ_d values. With each 5 °C increase decreasing τ_d a similar amount as reducing the xanthan concentration (but keeping the temperature the same).

5.2.1 Discussion - Two Regimes Arising

Above 45 °C, the measured delay time in samples with xanthan concentrations 0.4 - 0.8 g L^{-1} appear to flatten off, with each 5 °C increase in temperature having a reduced effect on τ_d, but nevertheless still ever decreasing the gel lifetime. This lessened response to temperature observed above 45 °C is dubbed the high-temperature regime, and the greater response at lower temperatures the low-temperature regime. Interestingly, the crossover temperature appears the shift, for 0.9 and 1.0 g L^{-1}, to 50 and 55 °C respectively. This is shown in Figure 5.2 where these crossover temperatures are highlighted in red. As seen with the low-temperature regime, the response to temperature in the high-temperature regime appears similar for all gels, with only 1.0 g L^{-1} appearing to have a slight difference, however due to the material used to produce the cell-holder, temperatures above 60 °C were not possible to measure, so only two points of the high-temperature regime could be measured for 1.0 g L^{-1}. If higher temperature measurements were possible, we would expect 1.0 g L^{-1} to follow the same trend as the other five concentrations studied.

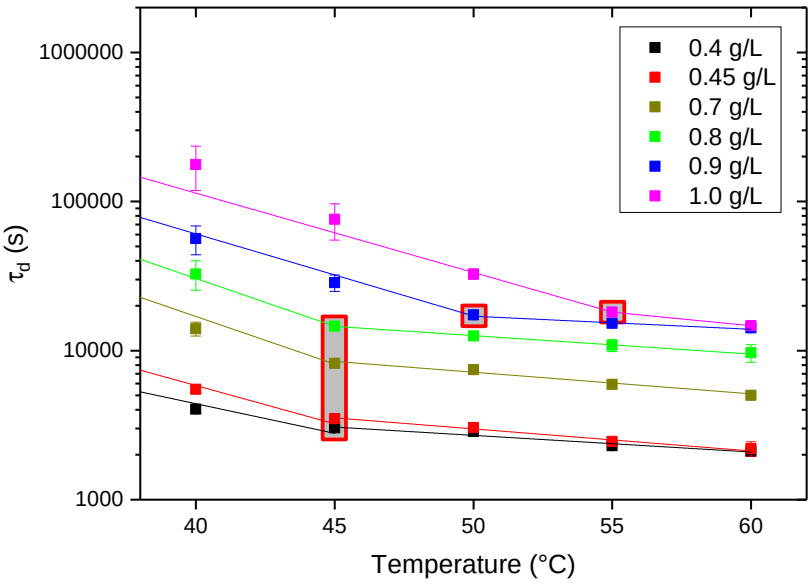

FIGURE 5.2: Delay times of gels with a range of xanthan concentrations, measured at different temperatures. Solid lines are linear fits to the data, showing the two regimes of temperature response, with the temperature at which the crossover occurs highlighted in red.

5.2.2 Regime Crossover Temperature Change

The crossover temperature at which a gel goes from the low to high temperature regime does not equate with the temperature at which the depletant xanthan appears to change its conformation/size, as shown earlier in Chapter 3, with the intrinsic viscosity of xanthan increasing at 55 °C. If these two temperatures were to match up this may give an indication of what is causing the lessened response to temperature, as if xanthan was to expand at 45 °C it would increase the depletion potential and thus τ_d. However the two temperatures do not match up, and even at 55 °C the change in xanthan does not impact the delay times of any gels studied.

For all temperatures delayed collapse is observed and there was no transition into creeping collapse.

5.3 Simple Interpretation - Activation Energy

$$\gamma = \exp(-\Delta U/k_B T) \tag{5.1}$$

To explore in greater detail the relationship between delay time and temperature the data was modelled as an Arrhenius dependent rate, using the Arrhenius equation shown in Equation 5.1, where ΔU is the activation energy. Thus by taking the natural logarithm of the delay time and plotting it against the reciprocal temperature (1/T) in Kelvin, the resulting gradient is equal to -$\Delta U/k_B T$, the well depth in $k_B T$.

$$ln\,(\tau_d) = \frac{\Delta U}{k_B T} \tag{5.2}$$

Figure 5.3 shows very clearly the two-regime response to temperature, especially for 0.7 - 0.9 g L^{-1} where the change in gradient is most pronounced. Fits are made for each individual gel concentration. Table 5.1 summarises the slopes of each concentration and shows that, in the low-temperature regime, that the activation energy is between four and seven times the depletion potential for these xanthan gels. However, in the high-temperature regime, the activation energy is of order the depletion potential ($\sim$ 5-10 $k_B T$ shown in Table 4.1).

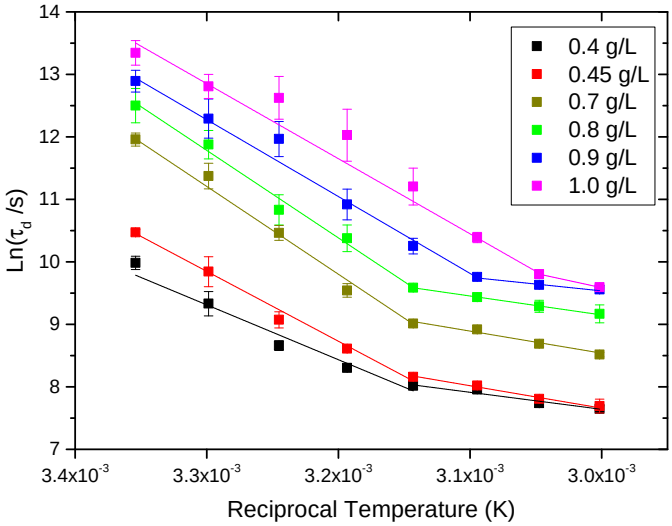

FIGURE 5.3: The natural logarithm of delay time (τ_d) plotted against 1/T. Solid lines are linear fits to the data.

Linear fit	0.4 g L^{-1}	0.45 g L^{-1}	0.7 g L^{-1}	0.8 g L^{-1}	0.9 g L^{-1}	1.0 g L^{-1}
Low T	30 ± 3 kT	38 ± 1 kT	47 ± 2 kT	47 ± 1 kT	41 ± 2 kT	40 ± 2 kT
High T	9 ± 1 kT	12 ± 1 kT	12 ± 2 kT	9 ± 3 kT	7 ± 2 kT	...

TABLE 5.1: Estimated activation energies for fits to the data shown in Figure 5.3.

5.3.1 Strand Thickness

For an area of a gel to rupture, an entire strand must be broken, therefore more than one particle-particle bond must fail as a strand can redistribute the load across it if only one particle becomes detached. With the low-temperature activation energy being multiple times the depletion potential, and the high-temperature regime activation energy being of order the depletion potential, it raises the question of whether the activation energy calculated in the two temperature regimes can give an insight into the gel structure in these regimes.

By considering the activation energies estimated from the fits of Figure 5.3 to be the energy required to break the strands present within the gel structure, and by using the calculated depletion potential between each particle, it is possible to estimate the strand thickness within a gel. Previous work by Bartlett et al. [46] using the same system found that strand thickness varies between 3 and 8 particles, with the strand

thickness gradually increasing as the gel ages (shown in Figure 1.17).

Table 5.2 shows the activation energy, calculated depletion potential for the polymer concentration of the gel, and the estimated strand thickness, calculated by dividing the activation energy by the depletion potential. This gives a strand thickness in the low-temperature regime of between 7 and 4 particles, and that as polymer concentration increases, the mean strand thickness decreases. This would seem to agree with the measurements of Bartlett et al. who find that as polymer concentration increase strand thickness decreases.

Linear fit	0.7 g L^{-1}	0.8 g L^{-1}	0.9 g L^{-1}	1.0 g L^{-1}
Activation Energy	47 ± 2 kT	47 ± 1 kT	41 ± 2 kT	40 ± 2 kT
Depletion Potential	6.9 kT	7.7 kT	8.6 kT	9.4 kT
Strand Thickness	~ 7	~ 6	~ 5	~ 4

TABLE 5.2: Estimated activation energies and associated strand thicknesses.

5.4 Viscosity Scaled Delay Time - Building a Model

As discussed in Section 1.5, the viscosity experienced by a particle in a depletion system can be at one extreme, the viscosity of the polymer solution (η_L), at the other extreme, the viscosity of the solvent (η_0), or a value in between. The simplest model for this possibly complex situation is a two-layer model where no polymer is present in the depletion zone so within the depletion zone η_0 is the value used, and then outside the depletion zone the bulk polymer solution viscosity η_L is used.

5.4.1 Using Solvent Viscosity

By taking the natural logarithm of the measured delay time (τ_d), dividing by η_0, and then plotting it against reciprocal temperature, Figure 5.4 is generated. Here it becomes apparent that once the solvent viscosity has been factored out, the high temperature fits become effectively horizontal, thus suggesting that in Figure 5.3 the slight gradient of the high temperature regime is the effect of the temperature dependent solvent viscosity (shown in Figure 5.5). Interestingly, the low temperature activation energies calculated using η_0 (Table 5.3) appear to be very similar to each

other at each gel concentration. With a gradual steepening of the gradient between 0.4 g L^{-1} and 0.8 g L^{-1}, and once the crossover temperature shifts to higher temperatures, the gradient decreases again slightly. It appears that factoring in the temperature dependence of solvent viscosity is suitable for scaling out the reduced temperature dependence observed in τ_d at high temperatures, but is insufficient to scale out the steep low-temperature dependence observed below 45 °C. Therefore in the next section we will study the scaling of τ_d with the polymer viscosity η_L.

$$ln\left(\tau_d\right) = ln\left(\tau_0\right) + \frac{\Delta U}{k_B T} \tag{5.3}$$

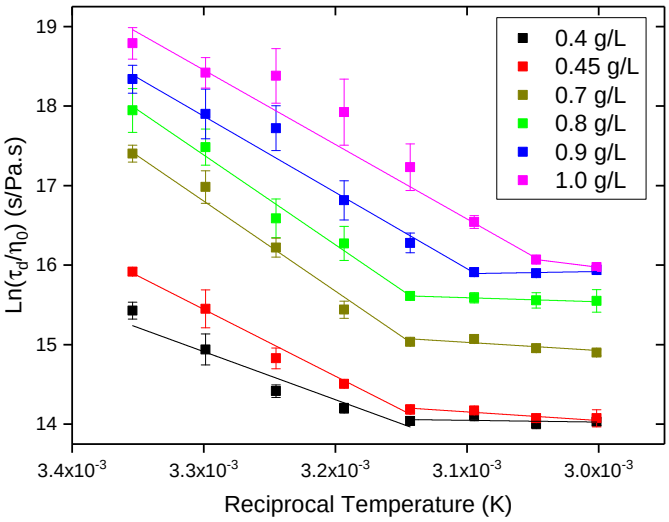

FIGURE 5.4: Ln(τ_d/η_0) for a range of xanthan concentrations. Solid lines are linear fits to the data.

Linear fit	0.4 g L^{-1}	0.45 g L^{-1}	0.7 g L^{-1}	0.8 g L^{-1}	0.9 g L^{-1}	1.0 g L^{-1}
Low T	21 ± 3 kT	29 ± 1 kT	38 ± 2 kT	39 ± 2 kT	33 ± 2 kT	32 ± 2 kT
High T	1 ± 1 kT	4 ± 1 kT	4 ± 2 kT	2 ± 3 kT	-1 ± 2 kT	...

TABLE 5.3: Estimated activation energies for fits to the data shown in Figure 5.4.

5.4.2 Using Polymer Viscosity

The viscosity of the polymer solution was measured by performing a table of shear rates on a xanthan solution in EG/H_2O solvent with 3 mM potassium chloride. As

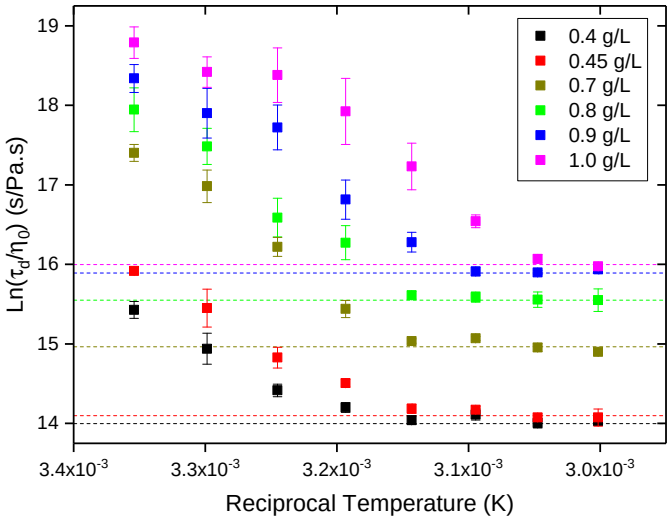

FIGURE 5.5: Ln(τ_d/η_0) for a range of xanthan concentrations. Dashed line is a guide to the eye.

xanthan is shear thinning, at low-shear rates the viscosity plateaus. This can be extrapolated to zero shear rate to give the viscosity η_L. Figure 5.6 shows the table of shear rates for a 0.8 g L^{-1} xanthan solution, where increasing the temperature reduces the viscosity of the solution, and the change with temperature becoming more significant at low shear rates. The data is cut off at an earlier point for higher temperatures, as the rheometer struggled to reach steady state measurements as a result of the viscosities measured being very low.

In Figure 5.7 the estimated values of η_L are shown for two xanthan concentrations, with the viscosity of the 0.9 g L^{-1} solution being higher than that of the 0.8 g L^{-1} solution at all temperatures apart from 55 and 60 °C, the viscosities may be similar at these high temperatures either due to error arising from the difficulty in making measurements due to the rheometer not being sensitive enough at such low viscosities, or that the viscosity of xanthan has been so greatly reduced that the 0.1 g L^{-1} concentration difference is no longer noticeable. Only a single value has been chosen, without error bars, to aid in simplifying the calculations for Figure 5.8 whilst including the error in τ_d. As including an error in η_L would make the errors too great to gain a reasonable fit. Also for the sake of simplicity, η_L was not calculated using the Martin equation shown in Equation 1.31.

There appears to be no obvious change in temperature response for the xanthan

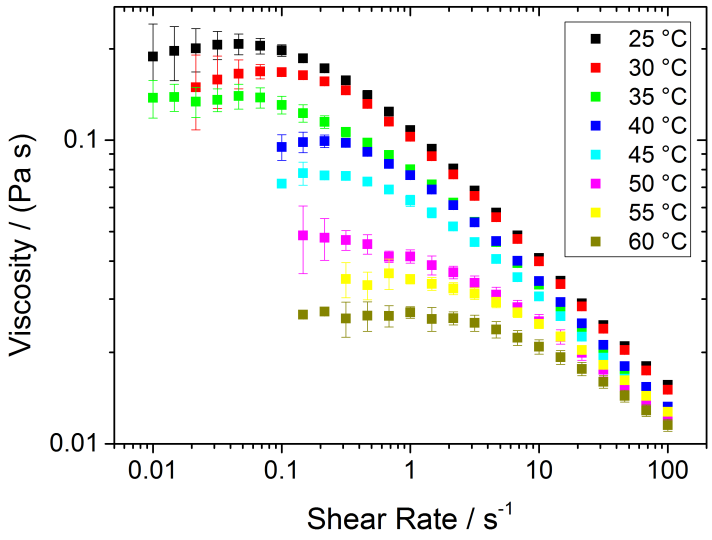

FIGURE 5.6: The shear rate dependent viscosity for a 0.8 g L^{-1} xanthan solution in EG/H_2O solvent, between 25 and 60 °C.

solutions that matches the crossover temperature for the delay time data, with no dramatic change in viscosity at 55 °C, the temperature at which capillary viscometry has shown the intrinsic viscosity begins to increase. This again lends credence to the argument that throughout the temperature range studied, the size of xanthan remains unchanged.

Figure 5.8 shows the natural logarithm of τ_d, divided by η_L for 0.8 and 0.9 g L^{-1} xanthan gels, measured between 25 and 60 °C (but plotted against 1/K). In the low temperature regime there is still a significant slope similar to that seen in Figure 5.3, and also Figure 5.4. The activation energy calculated and summarised in Table 5.4 is lower than both, as expected and a greater value is seen for η_L than for η_0. The fact there is still a significant downward slope in the value of $\ln(\tau_d/\eta_L)$ shows that even the greatest extreme of polymer viscosity change is not sufficient to explain the decrease in τ_d at temperature increases. One striking difference at low temperatures is that when η_L is factored out, the 0.8 and 0.9 g L^{-1} data more or less overlaps, whereas with η_0 (Figure 5.4) none of the data overlaps and each gel concentration has a discreet trend. This is presumably due to the fact that all of the data at each temperature has a single solvent viscosity value being factored out, whilst polymer viscosity scales with polymer concentration.

However, the seemingly good fit of η_L completely breaks down in explaining the

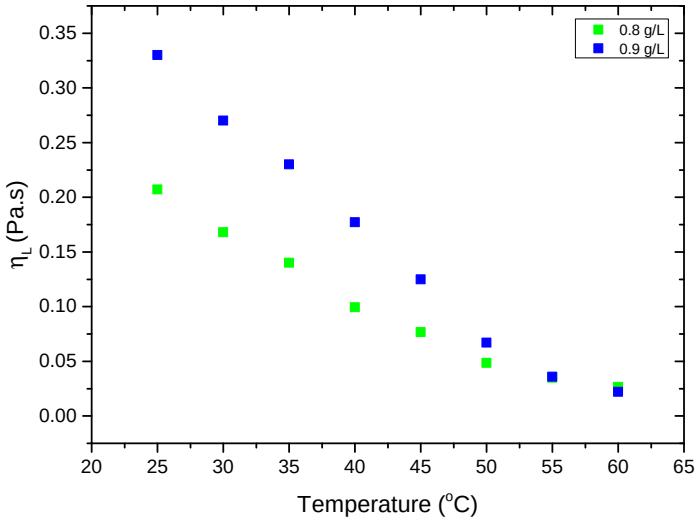

FIGURE 5.7: Polymer solution viscosity η_L for 0.8 and 0.9 g L^{-1} xanthan solutions in EG/H_20, between 25 and 60 °C.

high temperature regime above 45 °C, in which a large change in sign of the activation energy is observed. Whilst the 0.9 g L^{-1} activation energy is possibly overestimated due to the rheology data used to estimate η_L, but despite this even the 0.8 g L^{-1} activation energy is -18 ± 5 kT, which is not a physically realistic value. This coupled with the radical change in sign shows that scaling τ_d with η_L at high temperatures does not work.

Linear fit	0.8 g L^{-1}	0.9 g L^{-1}
Low Temperature	30 ± 2 kT	27 ± 2 kT
High Temperature	-18 ± 5 kT	-30 ± 5 kT

TABLE 5.4: Estimated activation energies for fits to the data shown in Figure 5.8.

5.4.3 Comparing the Use of Polymer and Solvent Viscosity

Therefore it appears that this extreme of using the polymer viscosity η_L is not suitable for exploring the temperature response of these gels, and therefore going forward the solvent viscosity η_0 will be deemed the relevant viscosity consider, and will be used in calculations such as the Kramer's escape time τ_{esc}.

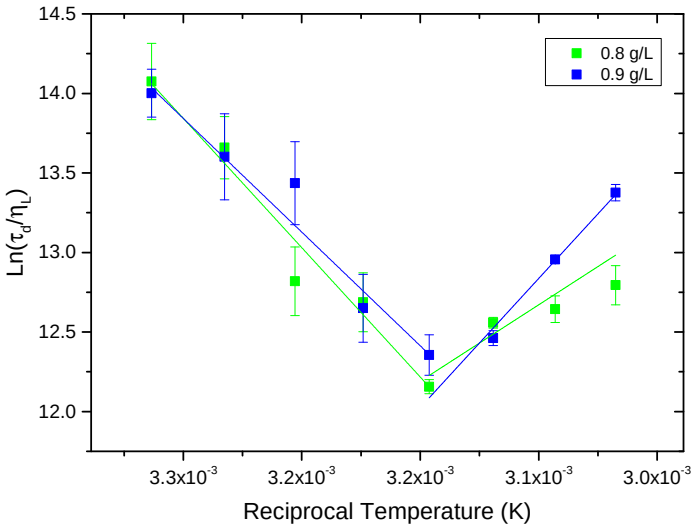

FIGURE 5.8: $\mathrm{Ln}(\tau_d/\eta_L)$ for 0.8 and 0.9 g L^{-1} xanthan-PDMS gels plotted against the reciprocal temperature 1/K.

5.5 Discussion - Particle Dynamics

Previous work has been done exploring the link between the Kramer's escape time (τ_{esc}) and the delay time before gel collapse (τ_d), Bartlett et al. [46] estimated τ_{esc} using the limiting low shear viscosity η_L, and found that τ_d correlated strongly with 240 x τ_{esc} (shown in Figure 1.20). Therefore we decided to compare how the Kramer's escape time is affected by temperature, assuming that the range and depth of the depletion remains unchanged across this range of temperatures (due to no structural rearrangement of the xanthan structure). This means that the only component dependent on temperature in the Kramer's escape time is the diffusion constant D_t.

5.5.1 Effect of Temperature on Particle Bond Lifetime

Using the viscosities of the EG/H_2O solvent shown in Table 3.3, the xanthan size measure by Bartlett et al.[46] and the calculated depletion potentials, the temperatures for which the Kramer's escape time is calculated is extended from just 25 °C, to 60 °C. All of which are shown in Figure 5.9.

It is clear to see in Figure 5.9 that the Kramer's escape time decreases with temperature in a smooth manner, due to the decrease in solvent viscosity. It is interesting to note that an increase of around 15 °C from 25 to 40 °C, to reduce τ_{esc}

to a similar value for the xanthan concentration below, such as 1.0 to 0.9 g L^{-1}, however across the temperature range studied, there is not sufficient change in τ_{esc} to cross two gel concentrations, such as 1.0 to 0.8 g L^{-1}.

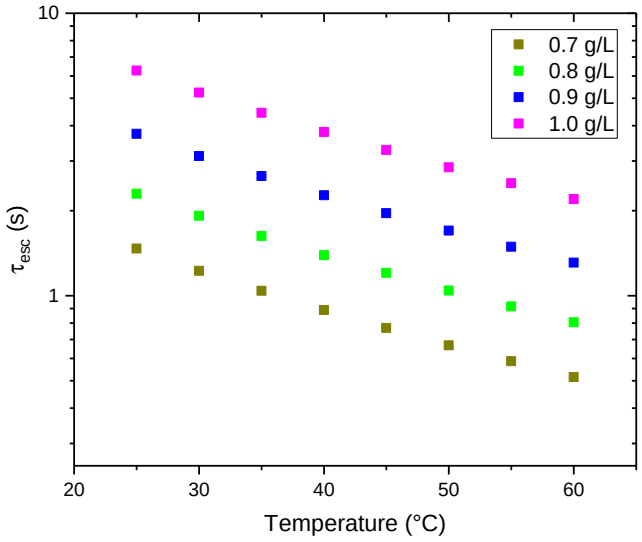

FIGURE 5.9: Calculated τ_{esc} from Equation 5.4, using η_0 in Equation 5.5 (both previously shown in Chapter 1). At 25 - 60 °C for C_p 0.7 - 1.0 g L^{-1}.

$$\tau_{esc} = \frac{\delta^2}{D_t} \frac{\exp(-U_0/k_BT) - (1 - U_0/k_BT)}{(U_0/k_BT)^2} \tag{5.4}$$

$$D_0 = \frac{k_BT}{6\pi\eta_L\alpha} \tag{5.5}$$

5.6 Linking Long and Short Time-scales

Figure 5.10 shows $\ln(\tau_d/\tau_{esc})$ between 25 and 60 °C, for 0.7 to 1.0 g L^{-1} gels, with the ratio between the two being concentration independent apart from very low polymer concentrations, indicatiing scaling of τ_d and τ_{esc} at a single temperature . Here, the two-regime dependence becomes even more apparent, in the similar way that it does when η_0 is accounted for in Figure 5.4. However when accounting for τ_{esc} all ratios at a given temperature overlap, with the ratio of τ_d/τ_{esc} decreasing as temperature increases, before in the high temperature regime, the ratio plateaus for all concentrations.

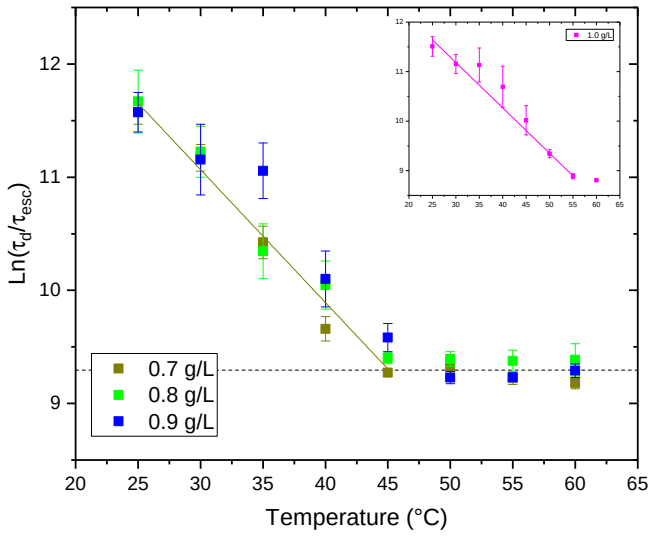

FIGURE 5.10: Ratio of τ_d and τ_{esc} from 25 to 60 °C, for C_p 0.7 - 0.9 g L^{-1} and 1.0 g L^{-1} (inset) xanthan-PDMS gels ($\phi = 0.2$).

This shows that even once the temperature-dependent particle dynamics have been accounted for, it is still insufficient to explain the observed change in delay time with temperature. This may come about due to 2 competing processes within the gel, such as strand breakage and healing, changing with temperature, and the crossover regime signifying where the rate-determining process switches. Much akin to the stress response seen by Sprakel et al. [60] where at low stress strand healing dominates and then at high stress, strand breakage dominates. It could also be interpreted, similar to the activation energies above, that the gel structure is changing with temperature, namely the average strand thickness. At lower temperatures, the strands becoming thinner as temperature increase. The plateau seen in τ_d/τ_{esc} would then signify a strand thickness of one particle, and the plateau being caused by the fact you can't have a strand thinner than one particle and still have a space-spanning network form (and thus a gel).

Linear fit	Low Temperature	High Temperature
τ_d/τ_{esc}	38 ± 2 kT	2 ± 1 kT

TABLE 5.5: Estimated activation energies for fits to the data shown in Figure 5.10.

5.7 Results - Settling Dynamics

With such a drastic response to temperature observed in the delay time τ_d, it stands to reason that perhaps there will also be a change in the way the gel collapses, that may shed insight into the cause of the temperature behaviour observed.

5.7.1 Height Profiles

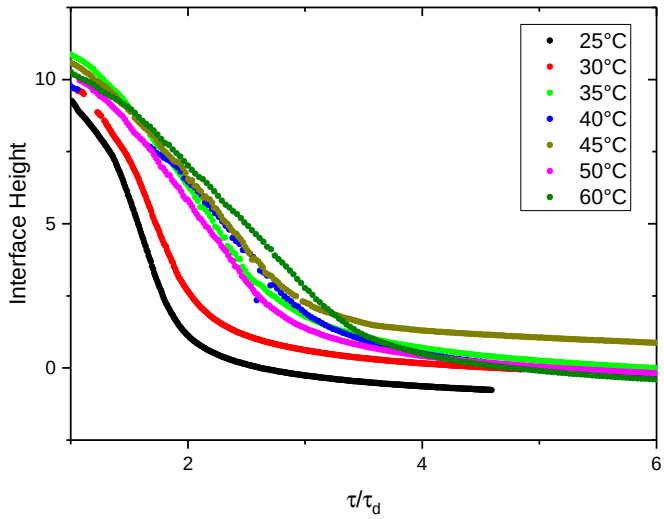

(A) 0.4 g L^{-1} xanthan-PDMS gel.

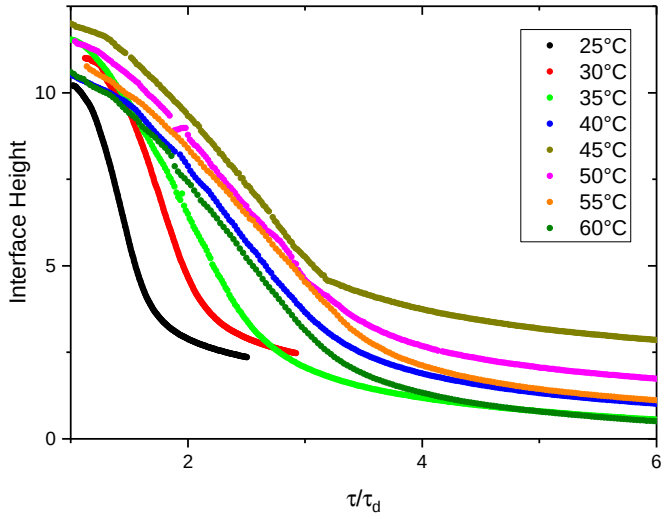

(B) 0.45 g L^{-1} xanthan-PDMS gel.

FIGURE 5.11: Height profiles $(1/h)$ plotted against τ/τ_d from 25 - 60 °C.

As shown in Figure 5.11 the height profiles all show a period of rapid collapse before compaction. At all temperatures it appears that the rapid collapse occurs of a similar multiple of τ_d, with there appearing to be a slight trend, with higher temperatures appearing to take slightly longer with respect to τ_d but not to any great degree. There appears to be no significant trend above 40 °C, with both gel concentrations showing similar rates of collapse, not yielding any insight into the change in τ_d response to temperature at high temperatures. The 0.45 g L^{-1} gels show a larger variation in height than the 0.4 g L^{-1} gels due to the samples being added to the cell holder from left to right, but this larger variation does not seem to affect the gel collapse.

5.7.2 Viscosity Adjusted Height Profiles

To explore how the viscosity of the solvent can affect the height profile of a gel at different temperatures the time was divided by the solvent viscosity (η_0), as the particles will be moving through sample as they cream to the top, rather than normalising τ against τ_d, it is normalised against η_0. The interface height of each sample (h) has been normalised against the height of the interface at collapse (h_d), to remove the variation seen in Figure 5.11.

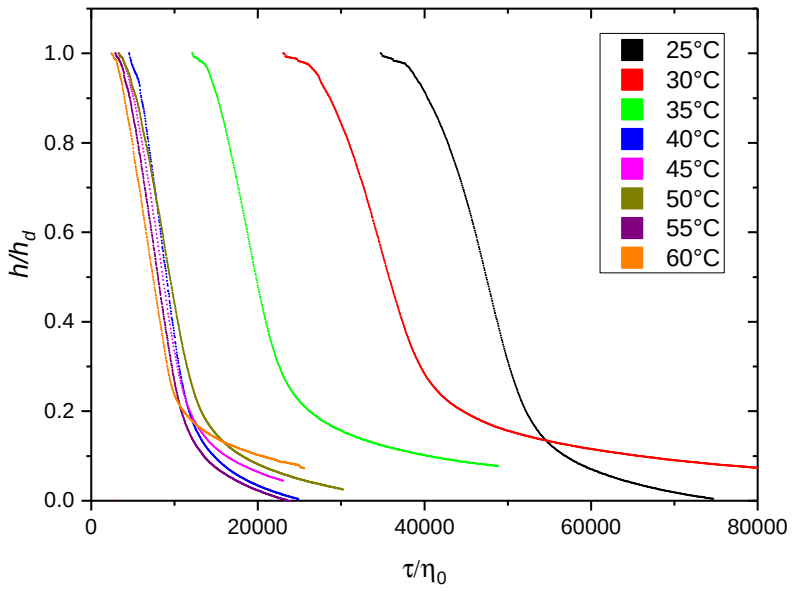

FIGURE 5.12: Normalised height plotted against τ/η_0 for 0.7 g L^{-1} Xanthan Gels.

Figure 5.12 shows the solvent adjusted collapse profiles for a 0.7 g L^{-1} respectively. This graph is interesting as it encapsulates the height profile, the solvent accounted delay time, and how the shape of the height profiles compare. As the temperature increases, the delay time decreases, so the height curve moves to the left, until at 45 °C they begin to overlap, this corresponds to the regime change seen in Figure 5.4. After a slight initial curve to the height profile, just after delay time, the majority of the rapid collapse period becomes more of less linear, presumably as the gel structure has yielded, and the sample begins to behave as a fluid. At all temperatures the slope appears to be the same, unlike in Figure 5.11, where the slope decreases as temperature is increased. This is most likely due to the greater effect temperature has on the delay time compared to the rapid-collapse portion of a gel's lifespan.

By plotting the interface height against τ/η_0 it shows the strength in comparing different time-scales and factors can give insight to the broader picture in both the effect of gel composition and temperature. Another interesting way to plot this data is shown in Figure 5.13, where both the factors that determine delay time being plotted on separate axis, breaking down the competition between increasing depletion potential and increasing temperature.

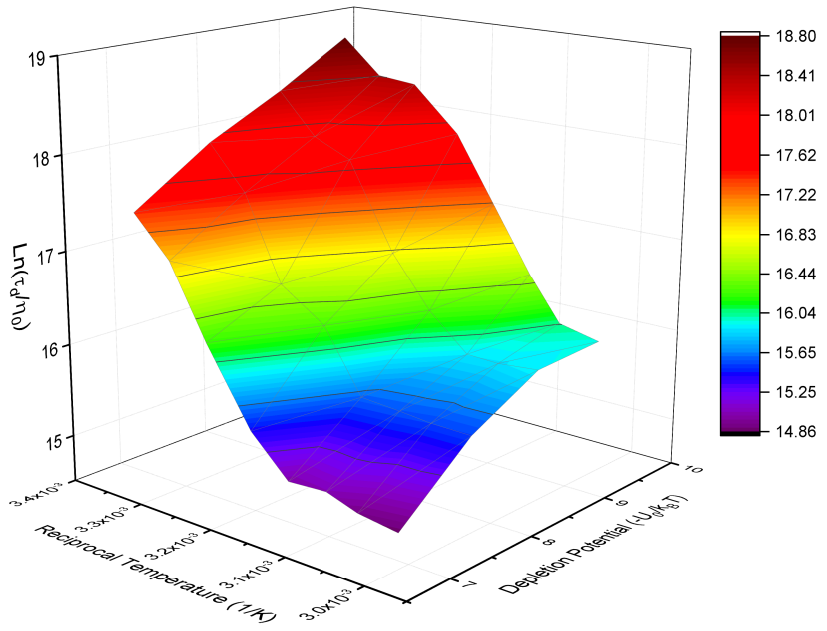

FIGURE 5.13: 3D plot of $\ln(\tau_d/\eta_0)$ against reciprocal temperature (1/K) with depletion potential ($-U_0/k_BT$) for 0.7 - 1.0 g L^{-1} xanthan-PDMS gels.

5.8 Results - Changing Depletant

To see if this response to temperature seen in the xanthan-PDMS gels is a more universal feature of colloid-polymer gels, or perhaps just a quirk of a xanthan based gel (which even if it was, would still be highly industrially relevant due to xanthan's large scale use) the xanthan depletant was exchanged for a cellulose derivative. The polymer chosen was hydroxyethylcellulose (HEC) Natrosol 250 HHX, with a M_w = 1.3 x 10^6 and a R_g of 126 nm, and by using the same size PDMS droplets as the xanthan gels, a size ratio q_r of 0.40 is achieved, a system previously used by Zhang [87]. Despite a similar overlap concentration (0.26 g L^{-1}) to that of xanthan (0.25 g L^{-1}) a significantly larger amount of polymer is required to achieve gelation, with up to 1.4 g L^{-1} only showing slow phase separation not gelation. Therefore the concentration presented is 2.0 g L^{-1} of HEC HHX, the delay times of which are shown in Figure 5.14.

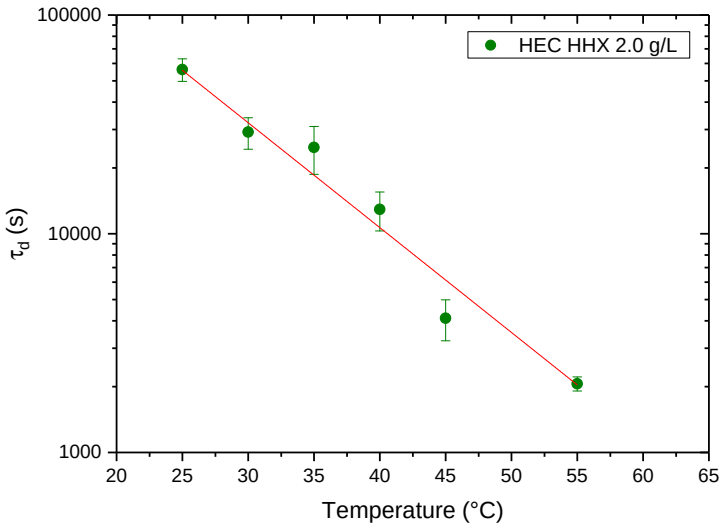

FIGURE 5.14: τ_d for 2.0 g L^{-1} HEC-PDMS Gels, between 25 and 55 °C.

At 25 °C, τ_d is $\sim$ 60000 s, approximately double the value measured by Zhang [108], a similar discrepancy to the delay times previously measured in the xanthan system due to the changing sample shape (cylindrical vials to rectangular vials). As temperature increase τ_d decrease as a exponential rate similar to that seen in the xanthan-PDMS gels. However over the temperature range covered no obvious change in temperature response is observed, and already at 55 °C the value for τ_d ($\sim$ 30

minutes) is lower than any measured for the xanthan-PDMS system, making higher temperature measurements unfeasible.

Due to the higher polymer concentration, the depletion potential is much greater than that of the xanthan-PDMS system, with 1.0 g L^{-1} of HEC generating an attraction of 15 k_BT, and 2.0 g L^{-1} generating an attraction of 30 k_BT. Despite this increase in depletion potential, that would normally be classed as a strong gel and exhibit creeping collapse, due to the still long range of the potential delayed collapse is still observed. Whilst a xanthan based gel is stable at 2.0 g L^{-1} for well over a month, a 2.0 g L^{-1} HEC HXX gel is stable for less time than a 0.7 g L^{-1} xanthan gel.

This reduced gel lifetime despite a greater depletion potential, causes times that are highly relevant in the xanthan-PDMS system, such as the Kramer's escape time τ_{esc}, to have no relevance to τ_d in this system. With τ_{esc} for a 2.0 g L^{-1} HEC gel being $\sim$ 500 days (a 2.0 g L^{-1} xanthan-PDMS gel is $\sim$ 1 hour). However as shown above, this response to temperature is not due to merely accelerated particle dynamics, but due to a change in the space-spanning network of the gel, and as the the volume fraction of PDMS has been kept the same in both the xanthan and HEC systems, one might expect a similar bi-continuous structure to form in both systems, but the rate and mechanism through which they age to be distinctly different.

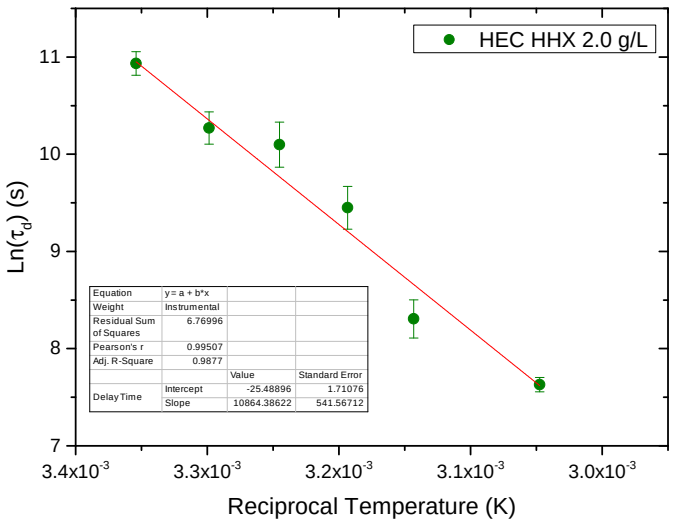

FIGURE 5.15: Ln(τ_d) for 2.0 g L^{-1} HEC-PDMS Gels, between 25 and 55 °C.

Again, as with the xanthan-PDMS system, the natural logarithm of delay time is plotted against reciprocal temperature (1/K) in Figure 5.15 and then an activation energy calculated from the gradient, the activation energy for the HEC-PDMS gel is calculated to be 36 $\pm$ 2 k_BT. This value sits between the activation energies of the 0.4 g L^{-1} xanthan gel, and the 0.7/0.8 g L^{-1} xanthan gels, and is roughly that of the 0.45 g L^{-1} xanthan gel, although for all of these xanthan gels the crossover temperature to the high-temperature regime occurs at 45 °C, whereas with the HEC gel there appears to be no crossover up to 55 °C. It is interesting to note that the activation energy is roughly the same as that of a the 0.45 g L^{-1} xanthan gel, as seen in Figure 5.16 that this is also where the delay time τ_d sits also with respect to the xanthan system.

This activation energy is of order the depletion potential for the HEC-PDMS system, which may suggest that there are only single particle strands present within the gel at all temperatures, however measurement of the structure of HEC-PDMS gels has been limited, with Gilligan [106] performing confocal microscopy on 0.4 - 0.7 g L^{-1} HEC-PDMS gels, he found that over this concentration range, the bi-continuous structure of the network does indeed become finer as HEC concentration is increased, but whether at 2.0 g L^{-1} the strands would only be one particle thick is unclear.

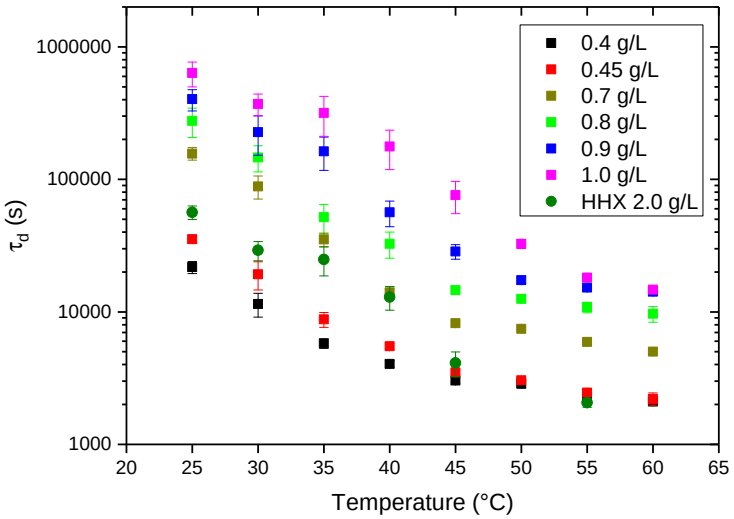

FIGURE 5.16: All measured delay times τ_d for both the xanthan-PDMS system and the HEC-PDMS system between 25 °C and 60 °C.

Figure 5.17 shows the height profiles of a 2.0 g L^{-1} HEC-PDMS gel between 25 and 55 °C, with interface height (h) normalised against the collapse interface height (h_d),

and time normalised against delay time τ_d for each temperature. All gels display the three main regimes of delayed collapse, even at high temperatures, where the delay time is less than an hour. There does not appear at first to be the same gradual stretching of collapse portion as seen in the xanthan gels but when comparing to the delay time, 35 and 40 °C sit above the general fit (Figure 5.14). Overall the rapid-collapse portion of the gel's lifetime (2 - 3 x τ_d) is similar that observed in the xanthan system.

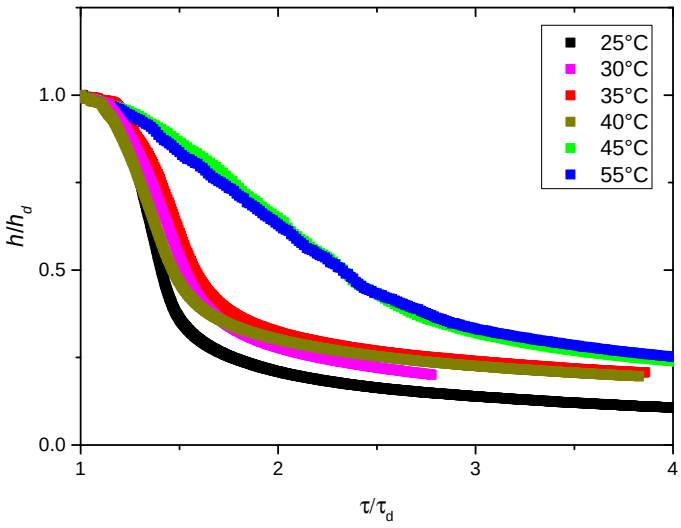

FIGURE 5.17: Height profiles for 2.0 g L^{-1} HEC-PDMS Gels.

As the solvent for both the xanthan-PDMS and HEC-PDMS gels are the same, the height profiles are normalised against the solvent viscosity η_0 in Figure 5.18. Here again we see a similar slope at all temperatures, and a shift to the left as temperature increases. The initial portion of each height profile (h/h_d = 1.0 - 0.95) appears the get steeper as temperature increases, with the 25 and 35 °C profiles showing a suppressed interface movement compared to 45 and 55 °C, suggested that even though an interface has formed, the network of the gel has become to some extent jammed again as solvent leaves the gel and strands begin to move. This "hanging on"is also seen in the xanthan-PDMS system (Figure 5.12).

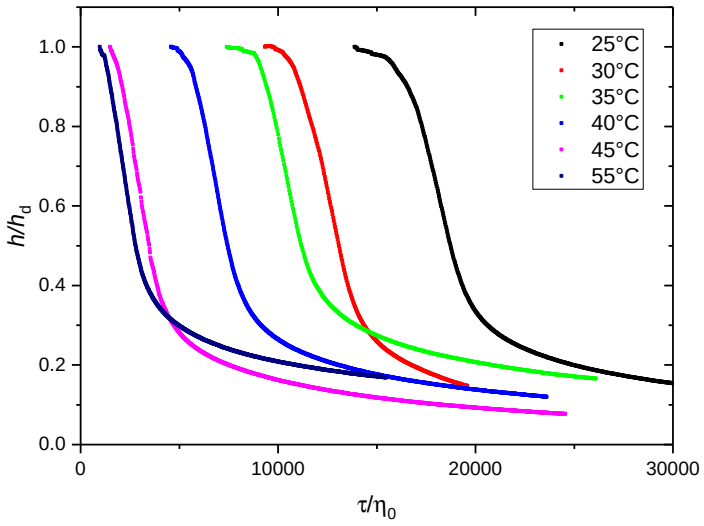

FIGURE 5.18: Normalised height plotted against τ/η_0 for 2.0 g L^{-1} HEC HHX Gels.

5.9 Summary

In this chapter we have shown data on a model colloid-polymer gel, using the polymer xanthan to form a depletion system, and how increasing the temperature of the gel causes a significant reduction in gel stability, quantified by the delay time before collapse τ_d. We see two regimes of temperature response in Figure 5.1, between 25 and 45 °C we see a sharp decrease in τ_d, the low-temperature regime, and then above 45 °C a muted decrease in τ_d as temperature is increased further to 60 °C. The crossover between these two regimes seems to shift to higher temperatures with increased polymer concentration, which is shown clearly in Figure 5.2, but further work is required to ascertain the cause of this shift.

By comparing τ_d to measured properties of the system known to change with temperature, such as polymer and solvent viscosity we deduce that firstly solvent viscosity is a more relevant property when considering the dynamics of a depletion system, and that this changing viscosity is insufficient to explain the reduction in τ_d recorded. Whilst temperature has a large impact on τ_d it appears to only have a slight impact on the height profiles after collapse, with all samples showing delayed collapse.

We present preliminary data in Figure 5.14 on a second system using a smaller polymer HEC-HHX, and also find a steep decrease in τ_d but no regime change is observed before the delay time becomes incredibly short. Due to the nature of this

system, the Kramer's escape time seems to not have any correlation with the gel lifetime, but the height profiles appear similar to those of the xanthan-PDMS system. At the very least, the data shows that the response to temperature is not just a quirk of using xanthan as a depletant.

By considering previous work linking single bond rearrangements to the lifetime of a gel, we calculate the Kramer's escape time τ_{esc} for the xanthan-PDMS system at all the temperatures studied. We show in Figure 5.10 that the ratio τ_d/τ_{esc} at all temperatures and for the gel concentrations studied, is independent of the xanthan concentration, building upon previous work carried out at ambient temperature using this system. We find that in the low-temperature regime, the ratio τ_d/τ_{esc} decreases as temperature increases, and then at ~ 45 °C the ratio remains the same as temperature is increased further. This changing relationship between single-particle dynamics and the lifetime of a gel suggest that the previous assertion that a gel's stability is wholly determined by its particle-particle dynamics is not sufficient. Whilst single-bond breakage does indeed play a key factor in determining the lifetime of a gel, there is another as-of-yet undetermined factor playing a vital role in determining the stability of a colloid-polymer gel. As such, in the next chapter we will endeavour to uncover what this may be.

Chapter 6

The Effect of Temperature on Network Formation

In this chapter, we characterise the rheological properties of a PDMS-xanthan gel at 25 °C, such as its shear-thinning behaviour, as well as the level of gelation in G' and G''. We compare the rheological properties of different strength gels, comparing both 0.7 and 1.0 g L^{-1} xanthan gels, finding that increasing polymer concentration increases the magnitude of G' and G''. We explore the effect of temperature on the level of gelation, as well as the samples' response to an applied strain, finding that even up to 70 °C, no change in the rheological properties of freshly prepared gels is found. However the rheological ageing of the gels studied is significantly affected by temperature, with G' increasing dramatically with age at higher temperatures.

6.1 Introduction

Testing the rheological properties of a formulation is a common method used in industry to give an indication of long-term stability. This is mainly because of the relative simplicity and speed with which a measurement can be made when compared to a long-term stability experiment. If key rheological properties can be related to a more stable formulation, such as the stiffness of a gel or the level of gelation in the formulation, then this would allow early characterisation of a new formulation to give an insight into the feasibility of the formulation as a product.

6.2 Results - Gelation at Ambient Temperature

Using the model gel system described in Chapter 3, and used for the collapse experiments of Chapters 4 and 5, a sample is prepared identically by gently stirring the PDMS emulsion ($a = 316$ nm) with a xanthan solution at the appropriate concentration to give the correct gel concentration and colloid volume fraction. For rheological experiments no dye is added to either the PDMS or EG/H_2O phase. Once a gel is prepared, it is sheared at 100 s^{-1} for 5 minutes and then allowed to recover for 15 minutes before the experiment is carried out. Further details on the geometries used for these rheology experiments can be found in Section 2.4.

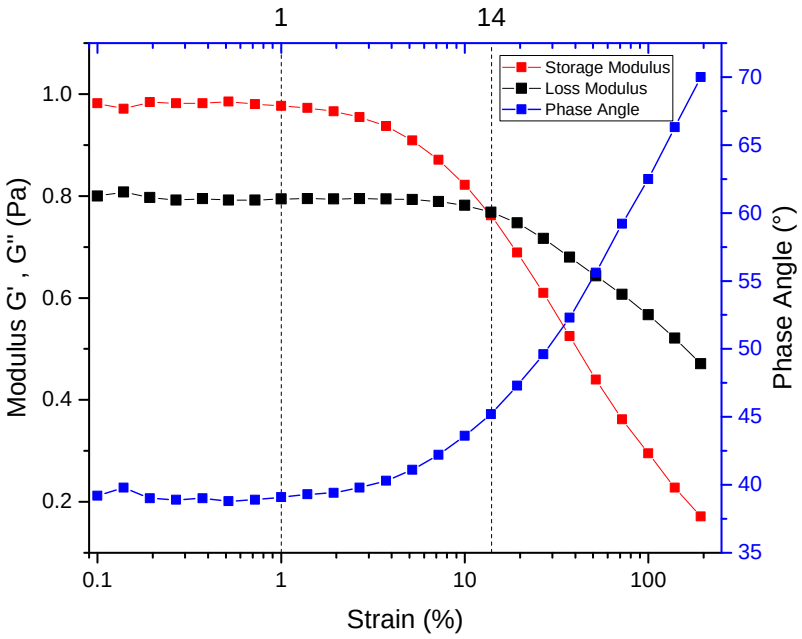

FIGURE 6.1: Strain sweep of a 1.0 g L^{-1} xanthan and PDMS gel.

Figure 6.1 shows a strain sweep performed on a 1.0 g L^{-1} xanthan-PDMS gel at 25 °C. At low strain the sample is gelled, as G′ is greater than G″. The linear regime for the gel is from 0.1 to 1 % strain, in which the sample properties are independent of the applied strain. At 1 % strain, the elastic modulus G′ begins to decrease and at 14 % strain the viscous modulus G″ becomes greater than G′ signifying a change from solid to fluid-like behaviour. The modulus G′ has a magnitude of $\sim$ 1.0 Pa, whilst G″ has a magnitude of 0.8 Pa, with the resulting phase angle being 40 °. This indicates that the gel formed is a very soft gel, as G′ is not much higher than G″,

usually a more rigid gel would have a G′ value an order of magnitude greater than G″.

Figure 6.2 shows shear stress and shear rate for a 1.0 g L^{-1} gel at 25 °C. The measurement is repeated to ensure there was no thixotropy, by performing one sweep from high to low shear rates, and then a second from low to high shear rates. A concatenated fit was used to fit to a power law, giving an exponent of 0.566, indicating that the gel is pseudoplastic in nature (shear-thinning) as expected.

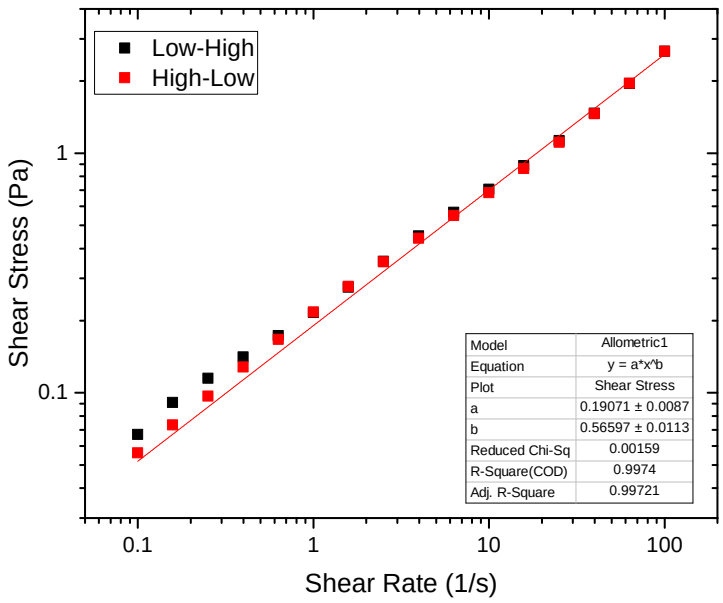

FIGURE 6.2: Shear Stress plotted against Shear Rate for a 1.0 g L^{-1} gel at 25 °C, with a power law fit.

6.2.1 Changing Gel Strength

Here we will compare the response to strain of two different PDMS-xanthan gels, one with 1.0 g L^{-1} of xanthan and another with 0.7 g L^{-1} to see the effect of changing polymer concentration (and thus the depletion potential).

Figure 6.3 shows strain sweeps for 0.7 and 1.0 g L^{-1} gels at 25 °C, with the 1.0 g L^{-1} gel having a G′ value of 1.05 Pa and the 0.7 g L^{-1} gel a 0.7 Pa value. This increase is due to the stronger depletion potential between the particles making up the gel structure, meaning the gel structure as a whole is more rigid. There is also

an increase in the viscous modulus G″, from 0.45 Pa to 0.7 Pa, which is attributable to the increased xanthan concentration of the sample.

Despite a reasonable difference the magnitudes of G′ and G″, the response to strain for both gels remains the same, at around 1 % strain G′ begins to decrease with higher strain and at ∼ 15 % strain G′ and G″ crossover.

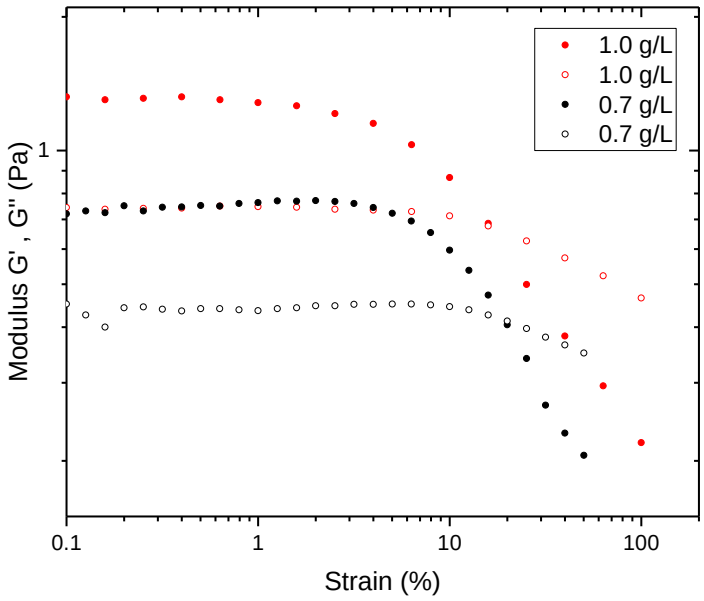

FIGURE 6.3: Strain sweeps of a 0.7 and 1.0 g L $^{-1}$ gel at 25 °C.

6.3 Low-Temperature Regime Gelation

With the baseline properties of xanthan-PDMS gels established above, in this section we will explore how the rheological properties of the gels change as temperature is increased, and whether a similar two regime dependence is seen as with τ_d in Chapter 5.

Figure 6.4 shows amplitude sweeps of freshly prepared 0.7 g L^{-1} PDMS-xanthan gels, at 25, 35, and 40 °C. At all temperatures the samples remain gelled, with G′ being greater than G″. As temperature is increased, the elastic modulus G′ remains the same at ∼ 0.8 Pa, showing that the level of gelation within the sample remains the same. As G′ is dependent primarily on the strength of the network and the depletion potential, this again shows that nothing fundamental in the composition is changing

as temperature increases. The decrease in G″ as temperature increases comes about due to the reduction of both solvent viscosity and polymer viscosity, causing the gels to be slightly stiffer at higher temperatures.

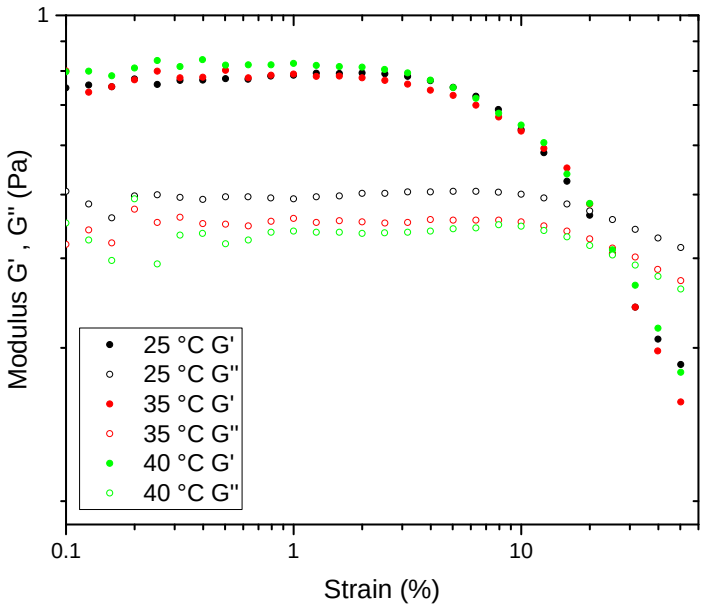

FIGURE 6.4: Amplitude sweeps at 0.5 Hz, of 0.7 g L^{-1} xanthan-PDMS gels ($\phi = 0.2$) at 25, 35 and 40 °C.

However, the most striking feature is that a significant increase in temperature has no effect on the critical strain at which G′ begins to drop, which can be seen as the point at which the gel structure begins to deform and break up, allowing the sample to begin to behave as a liquid. The fact that this response to strain is unchanged by temperature suggests that the initial structure of the gel is temperature independent, underpinning the previous assertion that the depletion potential in this system is unchanged by temperature.

Figure 6.5 shows strain sweeps of 1.0 g L^{-1} PDMS-xanthan gels between 25 and 50 °C. The magnitudes of G′ and G″ are similar to those shown in both Figures 6.1 and 6.3, showing the high level or reproducibility between both experiments and different samples. As with the 0.7 g L^{-1} gels, there is no change in the magnitude of G′ as temperature is increased and there is only a slight decrease in G″. The critical strain is again $\sim$ 15 % strain at all temperatures.

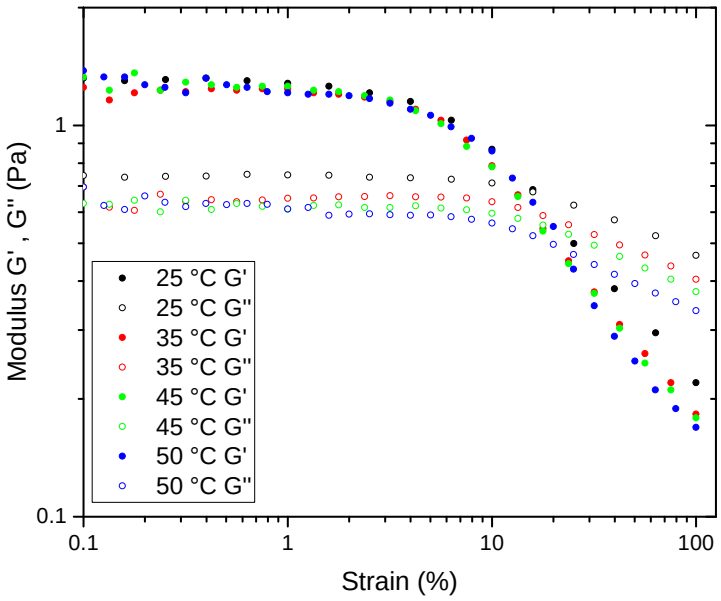

FIGURE 6.5: Amplitude sweeps at 0.5 Hz, of a 1.0 g L^{-1} xanthan-PDMS gels ($\phi = 0.2$) at 25, 35, 45 and 50 °C.

6.4 High-Temperature Regime Gelation

With no change in rheological properties observed in the low-temperature regime, the change to the high-temperature observed in Chapter 5 may be due to a change in the rheological properties occurring at 45 or 50 °C. To test this, a 1.0 g L^{-1} is heated from 40 °C to 70 °C in 5 °C intervals every 10 minutes, this is shown in Figure 6.6. The measurement is made at a fixed strain (0.5 %) within the plateau region of Figure 6.5 to allow the sample to be probed within the linear response regime, so the applied strain does not affect the properties of the gel.

As the sample is being heated at intervals, the elastic modulus decreases slightly during heating, and then recovers once the temperature plateaus, giving the slight undulation in G′. Because of this, the two dashed lines are added to aid the eye. It is clear that despite this slight variation in G′, there is no noticeable change in the rheological properties of the gel as it is taken into the high-temperature regime, even going 10 °C above the highest temperature studied in Chapter 5, yields no change in the rheological behaviour. Much like the previous measurements made, the viscous modulus G″ decreases with increased temperature.

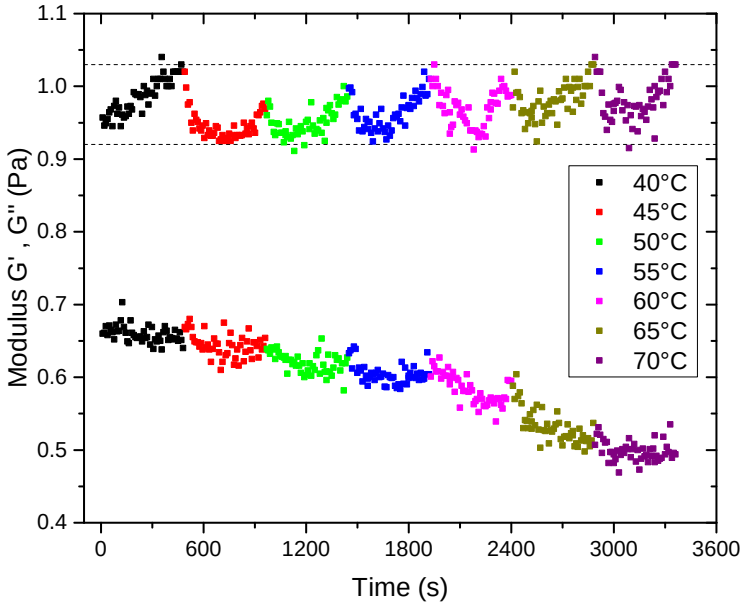

FIGURE 6.6: Oscillatory Rheology with fixed 0.5 % strain at 0.5 Hz for a 1.0 g L^{-1} xanthan-PDMS gel ($\phi = 0.2$) between 40 °C and 70 °C.

Looking in further detail at Figure 6.6, it is clear to see that there is no change in rheological behaviour that correlates with the change in the intrinsic viscosity of xanthan shown in Chapter 2, with the change in xanthan size having no apparent affect on the gel as a whole. Further more, the fact that there is no sudden increase or decrease in G′ at these high temperatures shows there is no aggregation or rupturing of the PDMS droplets making up the gel network, and that at all temperatures the PDMS droplets remain intact. This is presumably due to the combination of both steric and electrostatic stabilisation methods used to form the droplets.

6.5 Effect of Temperature on Sample Ageing

With rheology of fresh un-aged gels yielding no insight, Figure 6.7 shows how G′ and G″ evolve at a fixed 0.2 % strain (within the plateau region of Figure 6.6) so the strain should not affect the ageing of the gel, but allow us to probe how it stiffens with age at different temperatures. At very short time scales the gels thicken rapidly at a similar rate for each temperature as they settle in the geometry of the rheometer.

At 25 °C the gel stiffens very gradually, in a linear fashion after the initial rapid settling. The rate of stiffening measured is similar to that previously observed by Bartlett et al.[46] using a vane rheometer for the same experimental system at 20 °C. With a gel at 35 °C, the gel initially stiffens at a similar rate to the 25 °C gel before at around 500 minutes it begins to stiffen at an increased rate. This would indicate no real change at early times but at later times the gel is ageing at an accelerated rate.

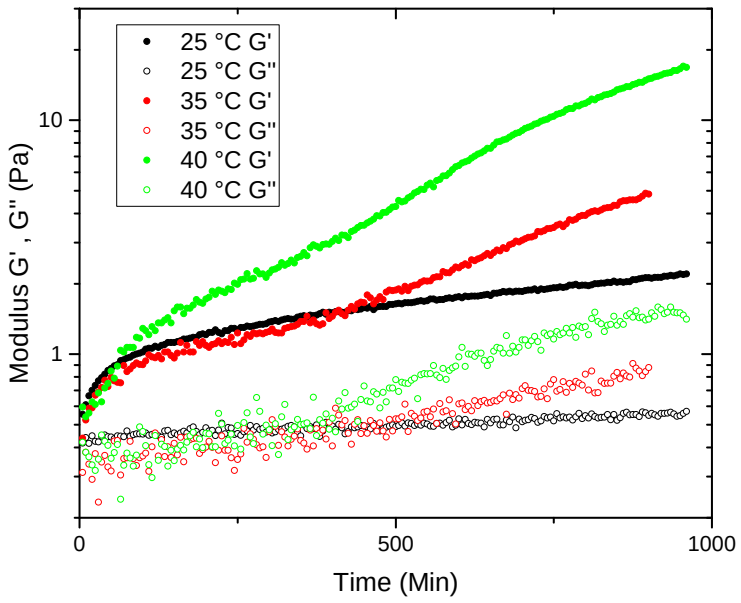

FIGURE 6.7: Evolution of G′ and G″ at 0.2 % strain for 0.7 g L^{-1} xanthan-PDMS gels ($\phi = 0.2$) at various temperatures.

Finally at 40 °C the sample thickened at a much accelerated rate for the entire experiment, with G′ changing over an order of magnitude within 12 hours. Previously Bartlett [46] found that at τ_d there was a sharp increase in G″ followed by a large fluctuation in G′ before finally a significant increase in G′. However, at the time corresponding to τ_d at 40 °C ($\sim$ 300 minutes) there is no change in either G′ or G″, indicating that the gel has not collapsed during the rheology experiment. The is most likely due to the rheometer geometry used to measure the gels, as τ_d has been shown to be affected by both the sample size and shape.

6.6 Summary

In this Chapter we have established the rheological properties of the PDMS-xanthan gel system at 25 °C, showing that the gels are shear-thinning in nature, as well as that both the elastic modulus G′ and the viscous modulus G″ increase with polymer concentration. By performing strain sweeps on freshly prepared gels we find that polymer concentration has no impact on the strain response of gels, with both 0.7 and 1.0 g L^{-1} gels having a linear regime until 1 % strain, and having predominantly fluid-like behaviour at $\sim$ 14 % strain.

By increasing the temperature at which strain sweeps are performed, we find that the samples remain gelled up to 70 °C, G′ being temperature independent, and G″ decreasing gradually with temperature. We interpret this as the depletion potential being unchanged, and thus the gel network remaining the same strength at all temperatures, causing G′ to remain the same. The decrease in G″ is due to the viscosity of both the EG/H_2O solvent and xanthan decreasing with temperature. We find that the change in intrinsic viscosity of xanthan at 55 °C does not cause any changes in the rheological properties of the gel as a whole, and that the PDMS droplets within the gel remain intact at all temperatures.

Finally we present data on the ageing of a 1.0 g L^{-1} PDMS-xanthan gel, and find that as temperature increases, the rate at which a sample stiffens increases significantly. This, coupled with the lack of change in freshly prepared samples, indicates that the change in τ_d seen in Chapter 5 comes about not due to fundamental changes to the gel composition at its formation, but due to the way temperature affects the ageing process during the gel's lifetime. In the next Chapter, we will explore the ageing dynamics of PDMS-xanthan gels at different temperatures using the technique Particle Tracking Velocimetry.

Chapter 7

Measuring Mesoscopic Changes During Gel Ageing

In this chapter, we present data collected using a novel technique to explore the mesoscopic dynamics of colloid-polymer gels, Particle Tracking Velocimetry. We find that in the low-temperature regime, there is a period of quiescence, with only small regions of localised collapse occurring, these then eventually propagate throughout the network, causing the entire gel to fail. In the high-temperature regime, we find homogeneous tracer movement before collapse, suggesting a dramatically different driving force behind gel collapse at these high temperatures. We find how changing the depletion potential affects the pre-collapse dynamics of a gel, as well as the crossover temperature between the two regimes.

7.1 Introduction

With Chapter 4 showing the rich behaviour previously observed in colloid-polymer gels, with most methods focusing on observation at collapse and after, in this chapter we will use a particle tracking technique Particle Tracking Velocimetry (PTV) to probe mesoscopic changes occurring before collapse, with an aim to finding both early warning of collapse as well as an explanation of the two-regime response to temperature seen in the delay time data.

Whilst no clear cause of the significant effect of temperature found through probing the microscopic length-scale, with a seemingly fixed ratio between τ_d/τ_{esc} at each

temperature. Also, rheological experiments in Chapter 6 show that at all temperatures a gel remains intact and has the same response to strain. As temperature increases, the sample stiffens much more as it ages, shown by a large increase in G′ at high temperatures, but only a slight increase at low temperatures. This shows that understanding how the gel ages at different temperatures is key to understanding the underlying cause of the response to temperature seen in Chapter 5, such as thinning particle strands, or a change in the dominant process occurring within the gel network.

7.2 Results - Low Temperature Regime (25 - 45 °C)

With the drive towards understanding how impending collapse of formulations can be predicted or detected at earlier times, Particle Tracking Velocimetry is used to detect localised movement within a gel prior to the observed macroscopic collapse at τ_d.

Figure 7.1 shows the mean tracer speed (calculated from Equation 2.11) in μm s^{-1} as a function of time for a 0.8 g L^{-1} gel. At the beginning of the experiment there is a small amount of tracer movement which is due to the gel forming and the tracers settling into the network, this movement is vertically down when looking at the images and minimal to no horizontal movement. Following this brief time of particle movement, there is an extended quiescent time in which there is no particle movement (the small undulations are presumably from statistical fluctuations due to the finite number of tracers), before the mean speed increases sharply to a peak speed (v_{max}) after which the mean speed begins to drop again. The time at which the maximum tracer speed is observed is determined as τ_{max}, which has been shown to correlate well with a simultaneous measurement of τ_d [84].

However, due to constraints of tracking an increased number of smaller tracer particles compared to the work done by Shaw [84], it was not possible to measure a value for τ_d during the PTV experiments, therefore the values of τ_{max} will be compared to the delay times previously measured and discussed in Chapter 4. Interestingly, as tracer movement begins to increase, it is possible to see the jagged nature of the curve in Figure 7.1a, especially around 120000 seconds, this jagged nature likely arises

from the heterogeneous nature of the network fractures. Meaning on a small area will give way before the rest of the gel network is able to take up the stress, so particle movement is again arrested for a short period before another part of the network yields, and so on and so forth, until irreparable damage has been done to the network, causing the sample to collapse macroscopically.

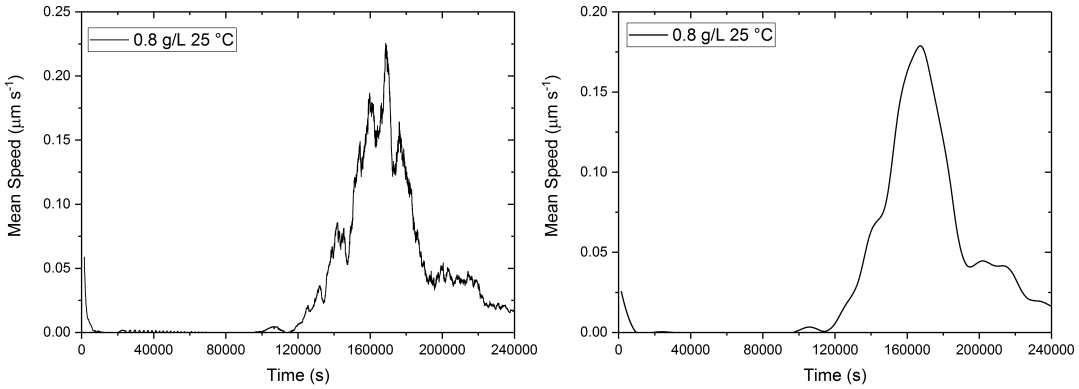

(A) Raw data. (B) Smoothed data.

FIGURE 7.1: PTV data for a 0.8 g L^{-1} xanthan-PDMS gel at 25 °C.

For Figure 7.1 the value for τ_{max} is determined as 168540 s from the raw data (7.1a) and 167520 s for the smoothed data (7.1b). The discrepancy between the two values is negligible mainly due to the fact, that in the raw data the peak velocity is very obvious and well defined. Comparing these values for τ_{max} with the previously measured τ_d value of $\sim 270000 \pm 70000$ s, shows that the value for τ_{max} is slight below the bottom range of the values of τ_d but is not dramatically lower. This lower value of τ_{max} can be attributed to the fact that the τ_d measurements were made with a lower resolution camera and at a much greater field of view, so that multiple samples could be observed at once, compared to the PTV experiments where only a single sample is measured.

Increasing the temperature to 30 °C still maintains the general shape once the data has been smoothed (Figure 7.2b), with a quiescent period initially, followed by a similar peak in tracer speed as seen at 25 °C. Compared to the 25 °C data, there seems to be a greater degree of tracer settling at the beginning of the experiment as the gel forms, but this amount of initial tracer settling was seen in room temperature samples by Shaw [84]. In the quiescent period there are small amounts of tracer movement ($\sim$ 30000 s) but for large periods of time there is no detectable movement within the

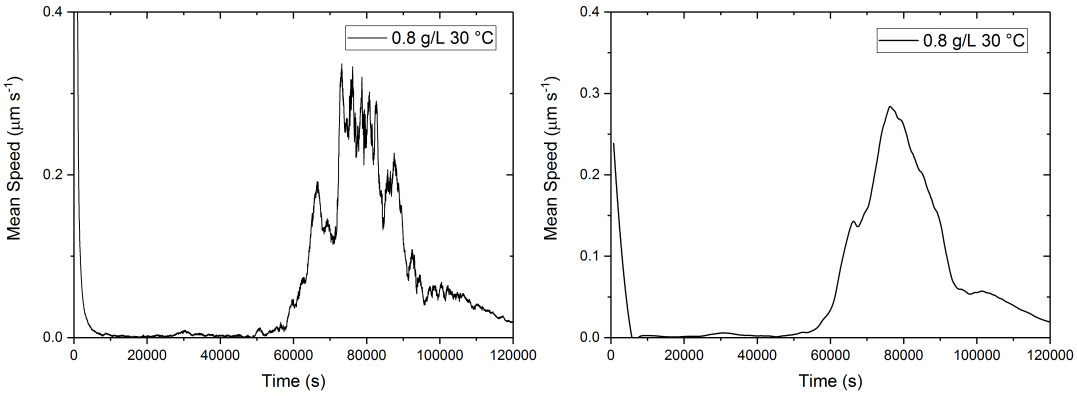

(A) Raw data. (B) Smoothed data.

FIGURE 7.2: PTV data for a 0.8 g L^{-1} xanthan-PDMS gel at 30 °C.

sample. There is still a jagged slope up towards the peak speed (v_{max}), however there are less times at which the sample recovers, giving a sharper increase towards v_{max}. Determining both τ_{max} and v_{max} from the raw data in Figure 7.2a is unreliable due to the many peaks of similar speed between 70000 and 80000 s, once the data has been smoothed, only a single peak remains allowing τ_{max} to be determined as 150900 s. Comparing this value of τ_{max} to the 145000 ± 30000 s value for τ_d shows excellent agreement between the two values.

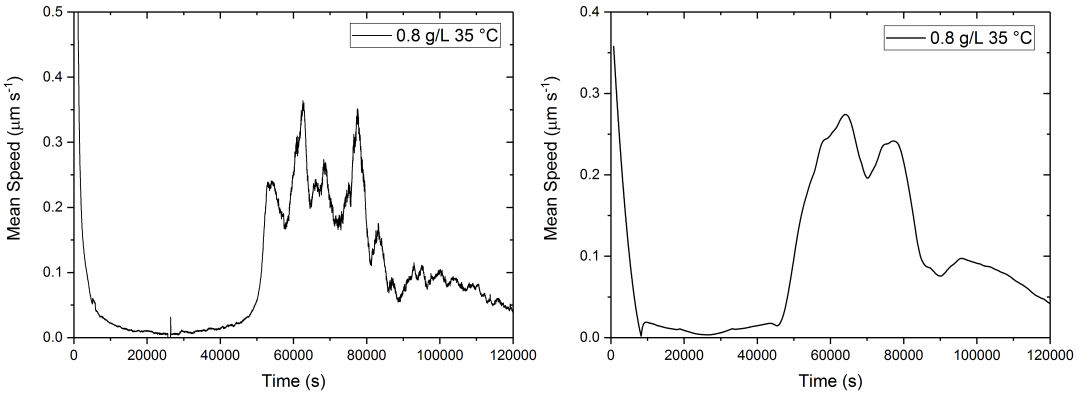

(A) Raw data. (B) Smoothed data.

FIGURE 7.3: PTV data for a 0.8 g L^{-1} xanthan-PDMS gel at 35 °C.

Figure 7.3 shows the raw and smoothed data for a 0.8 g L^{-1} at 35 °C, with the sample exhibiting the same behaviour as lower temperatures. Again, similar to Figure 7.2 there is no obvious τ_{max} value in the raw data, but in the smoothed data a value of 64070 s is apparent. Despite the width of the main peak in Figure 7.3b the value for τ_{max} agrees well with the previously measured τ_d value of ∼ 55000 ± 15000 s,

with an erratic and stochastic nature of the gel collapse observed in the PTV giving an insight into the range of τ_d values previously measured. At 35 °C there is still a quiescent time until $\sim$ 50000 s, but unlike 25 and 30 °C, there is no point in the gel lifetime at which there is no tracer movement, with the lowest value of tracer speed (v_{min}) being 0.0035 μm s^{-1}. At around 50000 s there is a significant increase in tracer movement, in an almost vertical manner, drastically different to the behaviour seen at 25 and 30 °C in which the mean tracer speed increases gradually with small decreases and increases as the gel structure redistributes stress throughout the network after a localised rupture. The steep gradient of mean speed at 35 °C suggests that the gel network has a limited ability to heal any damage done to it through localised ruptures and that also it cannot redistribute the stress applied to the network, again suggesting a changing structure as temperature is increased.

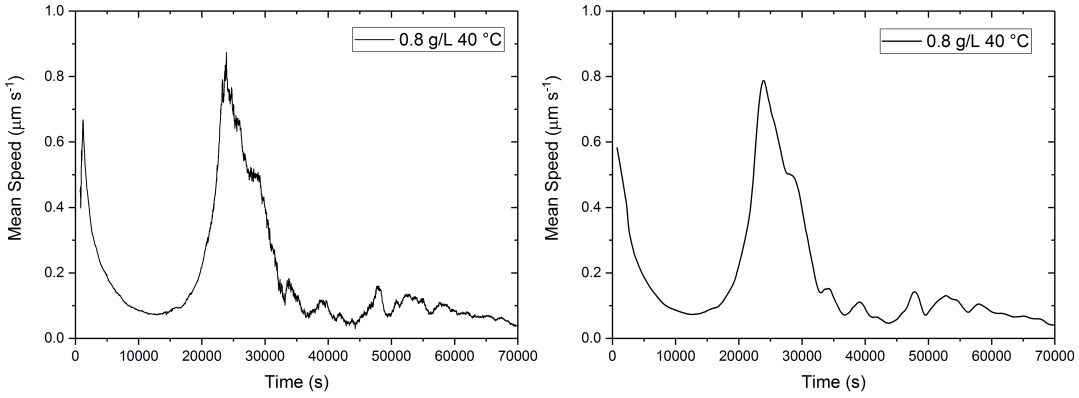

(A) Raw data. (B) Smoothed data.

FIGURE 7.4: PTV data for a 0.8 g L^{-1} xanthan-PDMS gel at 40 °C.

40 °C is the highest temperature within the low-temperature regime and exhibits similar behaviour to all other low temperature experiments. With a τ_{max} value of 23880 s, which is slightly low compared to the previously measured τ_d of 32000 $\pm$ 7000 s, there is still good agreement between the macroscopic collapse of a sample and the peak tracer speed in a sample. The initial tracer movement is comparable to the 30 and 35 °C samples, but unlike the lower temperature, the value for v_{min} does not reach zero or nearly zero, but a value of $\sim$ 0.073 μm s^{-1}. This lack of complete tracer arrest may well be due to the increased movement of the particle network within the gel, as indicated by the lower Kramer's escape time at higher temperatures, as well as Figure 6.7 in Chapter 5 showing a greatly accelerated stiffening (increasing G′).

However this change in quiescent period seems at odds with the measurements of the elastic modulus G′ as a function of temperature (Figure 6.5 in Chapter 6), which show that as temperature increases, G′ remains the same.

This disagreement arises from the significantly different length-scales that PTV and rheology probe, with PTV probing on the μm length-scale predominantly as each tracer bead is sensitive to changes in the immediate vicinity of each tracer. By looking at the ensemble behaviour of all the tracers we build up a picture of the dynamics within the gel. Whereas rheological measurements look at the entire sample and using a double gap geometry probes a length-scale of order mm or cm. This difference in length-scales shows that rheological measurements probe the strength of the entire gel network, whereas PTV looks at the strength of small portions of the network, and the apparent disparity between the two techniques suggests that despite the more dynamic/less static nature of the network at higher temperatures, the overall ability of the network to resist an applied stress (be it from a rheometer or gravitational stress) remains unchanged. More over, this opens up the possibility of using tracer beads within a gel as micro-rheometers to explore how homogenous the rheological properties of the gel are, or if they exhibit complex localised behaviours such as shear banding [109].

7.3 High Temperature Regime (50 - 60 °C)

With the high-temperature regime exhibiting a subdued response to temperature (the ratio τ_d/τ_{esc} remaining constant) it begs the question of if the pre-collapse behaviour will differ from that seen in the low-temperature regime, will the quiescent period be present and will τ_{max} continue to correlate with τ_d?

Figure 7.5 shows the raw and smoothed data for a 0.8 g L^{-1} at 50 °C, the first temperature within the high-temperature regime (excluding the crossover temperature), and shows significant differences when compared to the low temperature mean speed plots. The most significant difference is that there is no quiescent period at all, with there always being a significant amount of tracer movement. This may be explained by the fact that τ_d at high temperatures is incredibly short compared to 25 °C, however in Figure 7.5 τ_d and τ_{max} no longer correlate, with $\tau_d \sim 11000$ s and

$\tau_{max} = 4620$ s. As well as this, the vast majority of tracer movement appears to happen before macroscopic phase separation is observed, suggesting that a significantly different dynamic process is occurring at high temperatures.

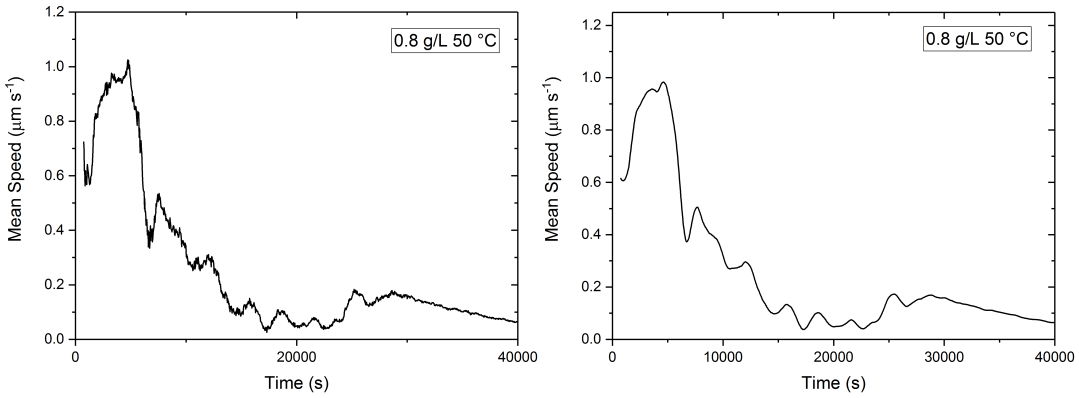

(A) Raw data. (B) Smoothed data.

FIGURE 7.5: PTV data for a 0.8 g L^{-1} xanthan-PDMS gel at 50 °C.

With this drastic change in pre-collapse behaviour the value of v_{min} no longer occurs before delayed collapse is observed but happens well after, so is of limited use in the high temperature regime. However v_{max} seems to be slightly higher than at lower temperatures but there is no significant difference observed between the low-temperature and high-temperature experiments. This would suggest that the particle speeds observed are a factor of both the dynamics of the system, as well as the viscosity of the gel, perhaps the solvent viscosity, or the bulk polymer viscosity. However, determining which value would require a significant improvement in spatial resolution.

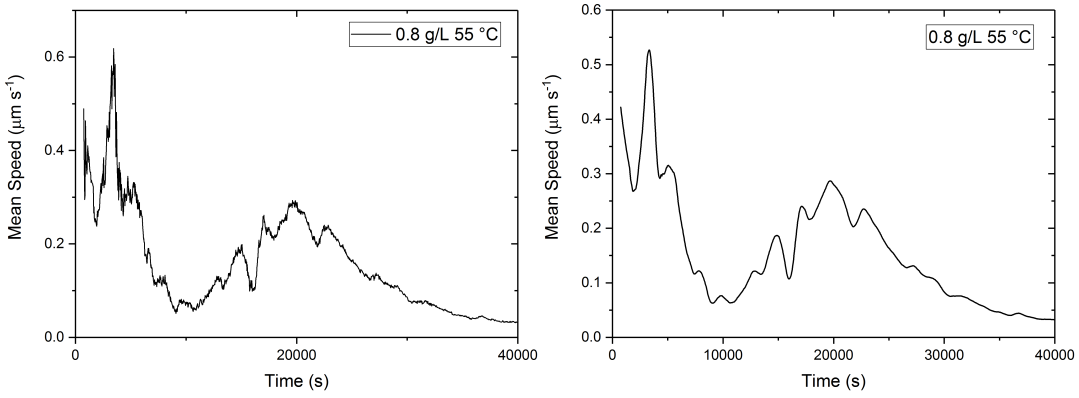

(A) Raw data. (B) Smoothed data.

FIGURE 7.6: PTV data for a 0.8 g L^{-1} xanthan-PDMS gel at 55 °C.

Increasing the temperature to 55 °C has little impact upon the mean speed as a function of time as shown in Figure 7.6, with the majority of tracer movement taking place early in the gel's lifetime, before τ_d. At 55 °C, the mean speed measured is lower than that of 50 °C, but similar to that of 35 °C, lending credence to the argument that tracer speed does not increase as temperature does purely due to the viscosity of the gel decreasing (either as a whole or the individual components).

Whilst at 50 °C there is only a single main peak of tracer movement, at 55 and 60 °C there is an emergence of a second peak at $\sim$ 20000 s (Figure 7.6) and 18000 s (Figure 7.7). Whilst at first glance this may suggest a return to the shape and dynamics seen at low temperature, that is not case, as the secondary peak occurs well after macroscopic collapse at τ_d, which is $\sim$ 10000 and 9500 s for 55 and 60 °C respectively. Examining the image stacks generated shows that this slowdown in tracer speed occurs as the gel phase separates into a colloid-rich and colloid-poor phase, with the colloid-rich phase effectively increasing in volume fraction as solvent is expelled into the colloid-poor phase beneath. As this volume fraction increases, the top phase of the sample becomes jammed before some parts rupture again allowing the phase separation to continue. It is also of note that in measuring τ_d, a height profile was generated which showed a relatively smooth movement of the interface after collapse (this can be seen in Figures 5.11 and 5.17) so this momentary jamming during the rapid-collapse phase is not sufficient to arrest a system once collapse has begun but may become a factor when working at higher xanthan concentration or at higher colloid volume fractions, and thus being of interest in industrial formulations.

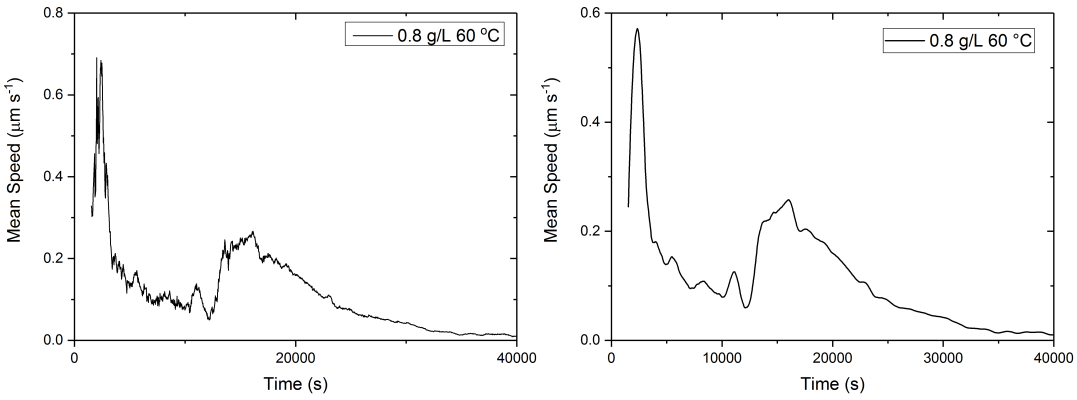

(A) Raw data. (B) Smoothed data.

FIGURE 7.7: PTV data for a 0.8 g L^{-1} xanthan-PDMS gel at 60 °C.

The biggest change from the low temperatures to high temperatures is the transition from heterogeneous tracer movement, in which a small number of tracers move in localised areas before collapse, to homogeneous tracer movement, in which all tracers move simultaneously before collapse is observed. An example of this can be seen in Figure 7.8 which shows trajectories before collapse for a 0.7 g L^{-1} gel at 25 °C and a 0.8 g L^{-1} gel at 55 °C. With only a small amount of the tracer beads moving in a localised region at low temperatures, consistent with the picture that coarsening of thicker gel strands and their eventual fracture is what leads to the collapse of the gel. Whereas at high temperature all the tracers move in a convection current type motion, with particles appearing to move downwards initially and then back up, with chaotic and straight vertical movement present.

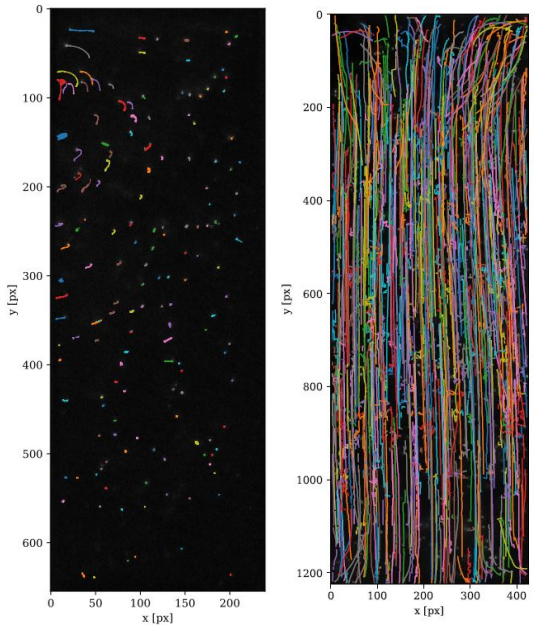

(A) (B)

FIGURE 7.8: Particle trajectories for two different xanthan-PDMS gels, one at 25 °C (A) and 50 °C (B). Both show tracer movement before delayed collapse is observed.

One way of rationalising both the plateau seen in the ratio between τ_d and τ_{esc} discussed in Chapter 4 and the change from heterogeneous tracer movement before τ_d to homogeneous tracer movement, is a change in the gel structure. With thicker multiple particle strands present at lower temperatures, the tracer beads are sensitive to the breakage of strands, rather than the breakage of individual bonds, as the entire strand must break to allow the tracer bead space to move. This co-operative

breakage that must occur gives rise to the heterogeneous nature of tracer movement, a schematic of how differing numbers of bonds need to be broken for a strand to rupture can be seen in Figure 7.9b, with the red lines showing where only a single bond needs to break to rupture a strand, and black lines showing some examples of where two or three particle-particle bonds need to be broken for the strand to rupture, and thus allow a tracer bead to move.

Conversely if the strands of the gel are only single particle strands, the tracer beads will be sensitive to not only the breakage of the strands but also of individual particle-particle bonds, as shown in Figure 7.9a only a single bond breakage is required for a strand to rupture. With the average lifetime of a single particle-particle bond being described by the Kramer's escape time, and being of order 10 seconds (as previously shown in Chapters 4 and 5), you would expect a tracer bead constrained by only single particle thick strand network would be able to move relatively unimpeded. This seemingly agrees with constant ratio between τ_d and τ_{esc} seen at high temperatures, as the time-scale of the structure present within the gel is similar to that of the individual particle-particle bonds, whereas the changing ratio between τ_d and τ_{esc} come about due to the changing structure comprised of different multiple particle strands.

7.4 Crossover Temperature Comparison

With two distinct temperature regimes, with an apparent sharp crossover at 45 °C for most xanthan concentrations studied, it is unclear whether the gels on the crossover temperature will exhibit the behaviour seen at low temperatures, having an quiescent period before a peak to v_{max}, with τ_{max} and τ_d correlating well, or no quiescence at high temperatures where τ_{max} no longer correlates with τ_d. If the crossover between the two regimes remains sharp this might be indicative of either a fundamental change in gel composition or a response from a component at 45 °C, however a less well defined crossover would suggest it is from a competition between two processes (such as bond/strand breaking and healing) or one process or parameter becoming the rate limited factor. One example of this is the strand thickness becoming thinner and thinner until it becomes a single particle strand, and thus can become no thinner.

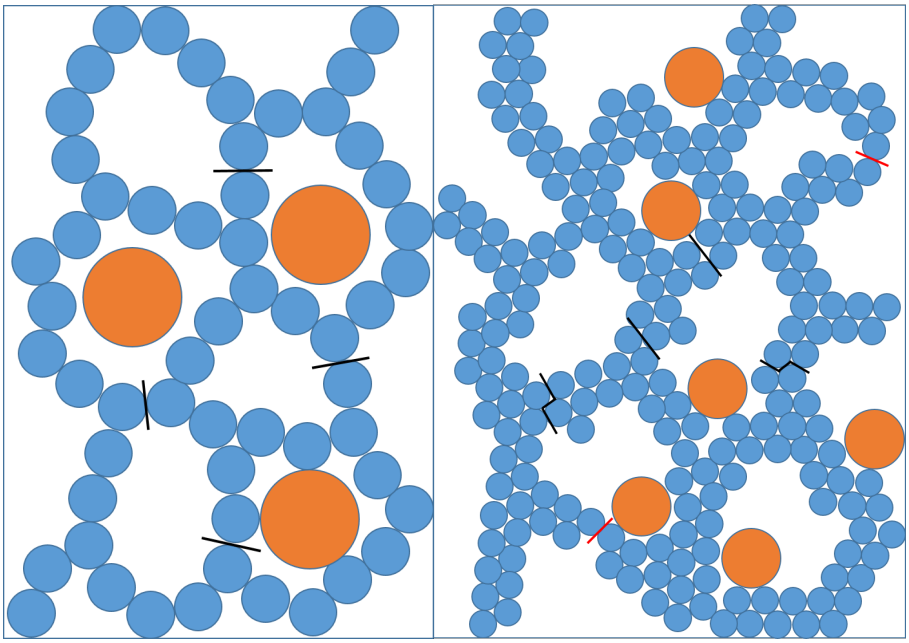

(A) (B)

FIGURE 7.9: Diagrams showing two gel structures of varying strand thicknesses, with tracer beads. Where (A) has only single particle strands and (B) multiple particle strands.

Therefore in this section we will study the PTV data for 0.7, 0.8, and 0.9 g L^{-1} xanthan-PDMS gels at the crossover temperature for each concentration.

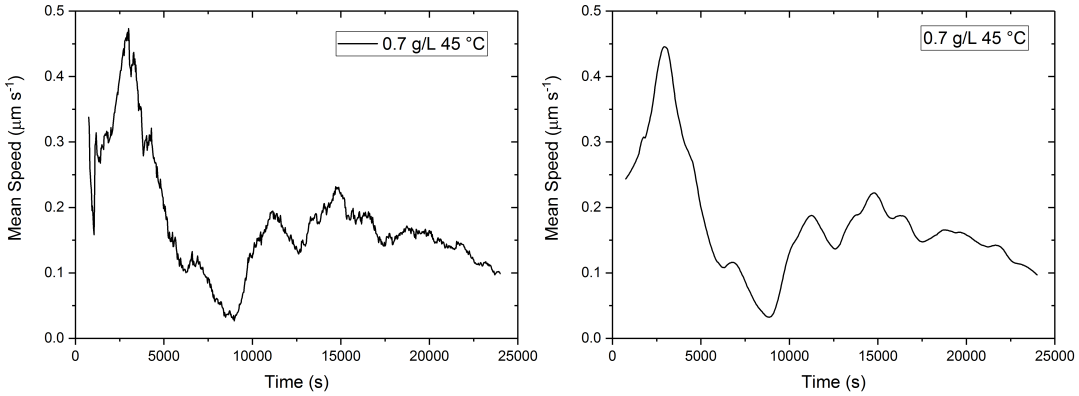

(A) Raw data. (B) Smoothed data.

FIGURE 7.10: PTV data for a 0.7 g L^{-1} xanthan-PDMS gel at 45 °C.

Figure 7.10 shows the raw and smoothed PTV data for a 0.7 g L^{-1} gel at 45 °C, with the gel appearing to exhibit the high temperature regime behaviour. There is significant tracer movement at early times, with no quiescent period present. τ_{max} is less than half of τ_d with the value for τ_d measured previously as $\sim$ 8200 s. As discussed, the drop in tracer speed is seen after τ_d whilst the gel is in the rapid

collapse period of its lifespan.

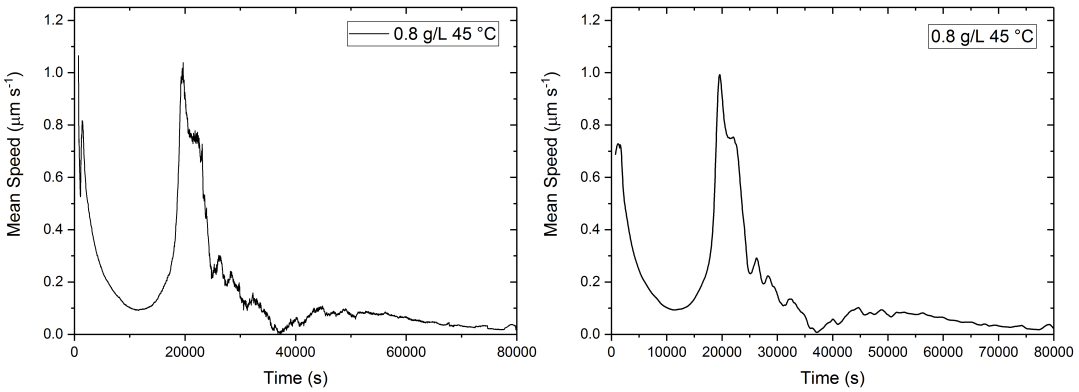

(A) Raw data. (B) Smoothed data.

FIGURE 7.11: PTV data for a 0.8 g L^{-1} xanthan-PDMS gel at 45 °C.

Whilst the crossover temperature for 0.7 and 0.8 g L^{-1} remains at 45 °C in the collapse data in Chapter 4, Figure 7.11 shows that a 0.8 g L^{-1} exhibits behaviour seen at low temperatures at 45 °C, different to that seen with a 0.7 g L^{-1} gel. τ_{max} (20000 s) correlates well with the previously measured τ_d of 15000 ± 1000 s, with τ_{max} being greater whereas most of the lower temperature samples have $\tau_{max} < \tau_d$ due to the increased camera resolution and method sensitivity. Similar to 40 °C there is no total quiescence of tracer movement prior to τ_{max}, but a significant reduction in mean speed after the initial settling seen in all samples at all temperatures. The value for v_{min} is μm s^{-1}, a significant increase when compared to 40 °C (0.073 μm s^{-1}) suggesting a definite drive towards the complete lack of arrest seen at higher temperatures, but at 45 °C the sample can suppress but not arrest internal movement.

7.4.1 0.9 g L^{-1} - Higher Crossover Temperature

With a 0.9 g L^{-1} gel, the transition between the 2 regimes of temperature response appears to occur at 50 °C in the collapse data, 5 °C higher than all gel concentrations below it. With this in mind it remains to be seen whether this higher transition temperature will behave like the 0.7 g L^{-1} gel which displays low-temperature behaviour at the crossover temperature or the 0.8 g L^{-1} gel, which exhibits high-temperature behaviour.

Figure 7.12 shows clearly that at 50 °C, a 0.9 g L^{-1} displays high-temperature regime behaviour, with high levels of tracer movement at early times, before the gel

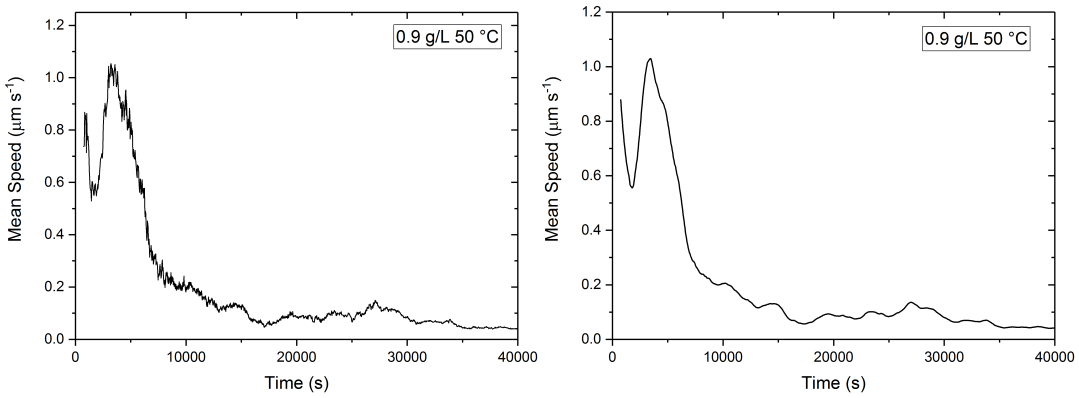

(A) Raw data. (B) Smoothed data.

FIGURE 7.12: PTV data for a 0.9 g L^{-1} xanthan-PDMS gel at 50 °C.

collapses. With τ_{max} being $\sim$ 5000 s and τ_d previously measured at 17000 s, there is no correlation between the two, as τ_d seems be when tracer movement begins to plateau at its lowest rate. v_{max} is of order 1.0 μm s^{-1}, the same as that seen for the 0.8 g L^{-1} gel at 50 °C, suggesting that an increased gel strength does not affect mean tracer speed, at least at high temperatures.

Gel Concentration	0.7 g L^{-1}	0.8 g L^{-1}	0.9 g L^{-1}
Crossover Temp (°C)	$T_c < 45$	$45 < T_c$	$T_c < 50$

TABLE 7.1: Crossover temperatures between the low and high temperature regimes determined from PTV.

7.5 Changing the Depletion Potential

As shown in previous chapters, changing the depletion potential in this gel system changes many properties of the gel such as τ_d and the elastic modulus G′. With this change in delay time, it would be reasonable to expect τ_{max} to continue to correlate with τ_d as seen above for the 0.8 g L^{-1} gel. With the rheological properties of the gel changing with depletion potential, it remains to be seen whether the tracer beads will move at a significantly different speed, or how quiescent the tracers will be at early times. With this in mind, this section will explore PTV data of 0.7 g L^{-1} gels between 25 and 55 °C, and compare them with the previously collected data using 0.8 g L^{-1} gels.

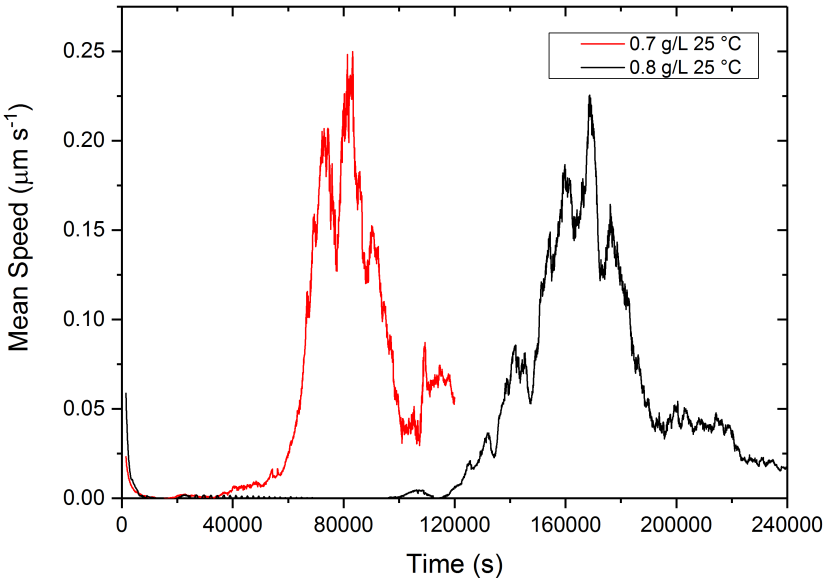

FIGURE 7.13: Raw PTV data for a 0.7 g L^{-1} gel at 25 °C and a 0.8 g L^{-1} gel at 25 °C.

Figure 7.13 shows raw PTV data for both a 0.7 and 0.8 g L^{-1} xanthan-PDMS gel at 25 °C. Both gels have a quiescent period at early times after a similar level of initial tracer settling, with both concentrations having zero tracer movement during the quiescent period. The first major difference is that τ_{max} for the 0.7 g L^{-1} is approximately half of the value for the 0.8 g L^{-1} gel. This shows that τ_{max} scales in a similar way to τ_d with respect to the depletion potential. Despite this difference in τ_{max}, the peak mean speed v_{max} for both gel concentrations is similar, with both being between 0.2 and 0.25 μm s^{-1}, with the overall shape of both peaks being very similar also. At first glance, this would appear to suggest that the tracer beads behave in a similar way for both the 0.7 and 0.8 g L^{-1} gel concentrations despite some differences in the rheological and collapse properties due to the differing depletion potential.

Looking in greater detail at a 0.7 g L^{-1} gel at 25 °C, Figure 7.14 shows both the raw and smoothed data. Similar to the 0.8 g L^{-1} gel shown in Figure 7.1 there is still a jaggedness to the slope suggesting that despite the lower depletion potential due to the lower xanthan concentration, the gel is still able to repair damage done to it. From $\sim$ 40000 s to 60000 s there is a very slow increase in tracer movement before the main peak to v_{max} begins. The smoothed data gives a v_{max} value of $\sim$ 0.20 μm

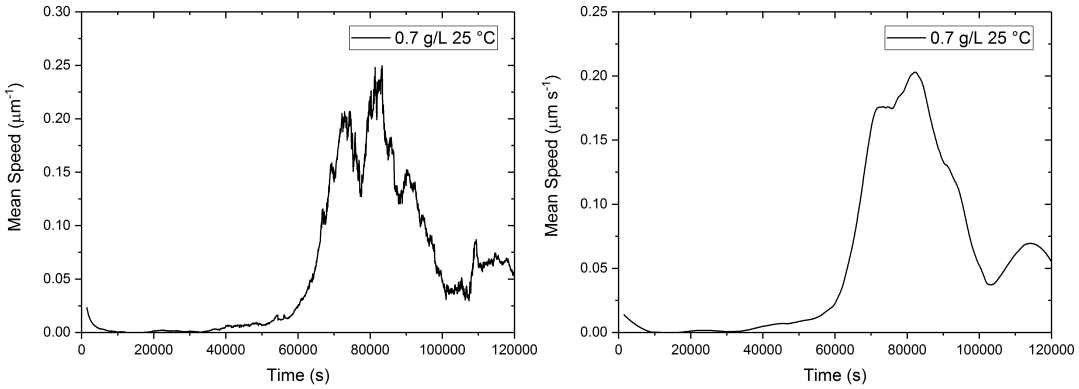

(A) Raw data. (B) Smoothed data.

FIGURE 7.14: PTV data for a 0.7 g L^{-1} xanthan-PDMS gel at 25 °C.

s^{-1}, about 0.5 μm s^{-1} lower than the peak observed in the raw data.

Figure 7.15 shows raw and smoothed PTV data for a 0.7 g L^{-1} gel at 35 °C, there is a similar level of initial tracer settling to the 0.8 g L^{-1} gel shown previously. However the degree of quiescence at early times is significantly diminished, with a v_{min} value of 0.1 μm s^{-1}. This value is significantly larger than the value of 0.0035 μm s^{-1} calculated for the 0.8 g L^{-1} gel, and is more akin to the value for 40 °C (Figure 7.4), which also happens to have a similar value for τ_{max} as well as τ_d in the collapse data in Chapter 5. This at first glance would appear to suggest that temperature and depletion potential are analogous to each other as not only the macroscopic delay time is the same, but also the mesoscopic dynamics shown by the tracer movement before collapse are the same.

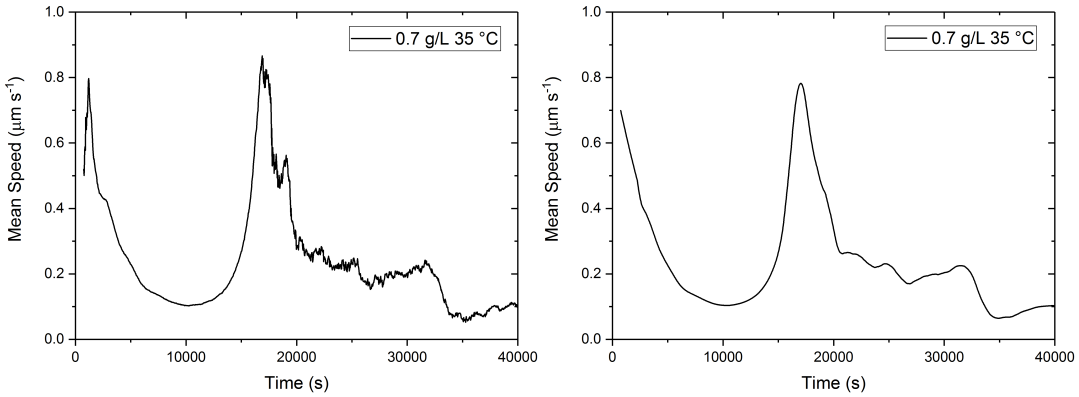

(A) Raw data. (B) Smoothed data.

FIGURE 7.15: PTV data for a 0.7 g L^{-1} xanthan-PDMS gel at 35 °C.

This is at at odds with the microscopic picture described in Chapter 5, where

τ_{esc} does not decrease at the same rate as τ_d, and as seen in Figure 5.10 the ratio at each temperature is concentration independent. This suggests that even though the collapse and PTV data appear to be almost quantitatively the same, there is still a fundamental difference in the ageing dynamics of the gel, due to the differing temperature and depletion potential.

The value of v_{max} at 35 °C is 0.8 μm s^{-1}, a significant increase compared to the value of 0.25 μm s^{-1} seen for the 0.8 g L^{-1} gel at 35 °C, which is interesting considering that both the 0.7 and 0.8 g L^{-1} gels have a similar v_{max} value at 25 °C. Whether a differing v_{max} value is indicative of a different property within the gel remains to be seen, as a thorough study of a single composition and temperature would be required to establish the inherent variation in measurements of v_{max}.

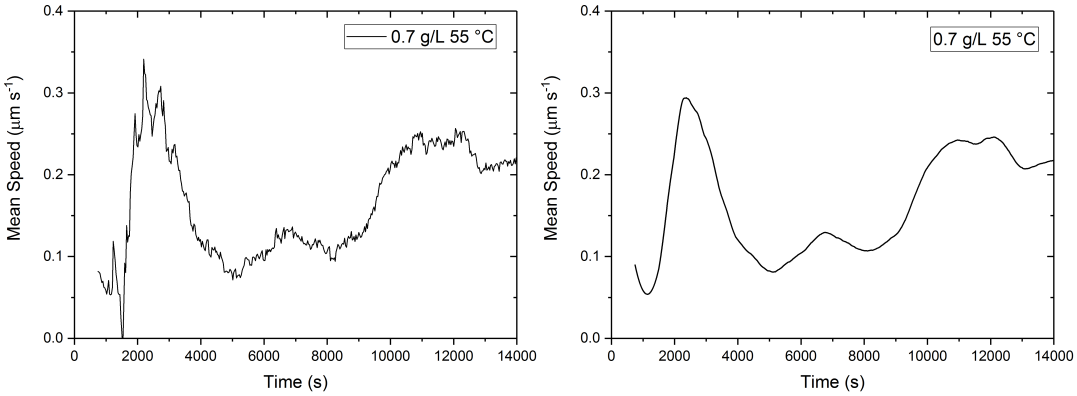

(A) Raw data. (B) Smoothed data.

FIGURE 7.16: PTV data for a 0.7 g L^{-1} xanthan-PDMS gel at 55 °C.

Much like the 0.8 g L^{-1} gel, in the high-temperature regime there is no quiescent period observed at 55 °C in a 0.7 g L^{-1} gel. The majority of tracer movement also occurs before τ_d ($\sim$ 6000 s), again, much the same as seen in both the 0.8 and 0.9 g L^{-1}. At around 5000 seconds the mean speed decreases to $\sim$ 0.1 μm s^{-1} suggesting that as the gel begins to collapse, the structure becomes slightly jammed as the interface begins to rise, but not sufficiently to halt the continued collapse of the gel.

It seems that 0.7 g L^{-1} gels follow the same general pattern as 0.8 g L^{-1}, in that τ_{max} correlates well with τ_d, v_{min} increases with temperature as the level of quiescence decreases. The low and high temperature regimes exhibit the same change from heterogeneous to homogeneous tracer movement before collapse.

7.6 Discussion - Reproducibility of PTV Measurements

Due to the length of time taken to perform one PTV experiment as well as the fact only one sample is observed at a time, doing a comprehensive data set on reproducibility was infeasible, as it would have severely limited the breadth of data collected. Shaw [84] previously performed PTV experiments at a lesser resolution with larger tracer beads and found a good degree of reproducibility at room temperature.

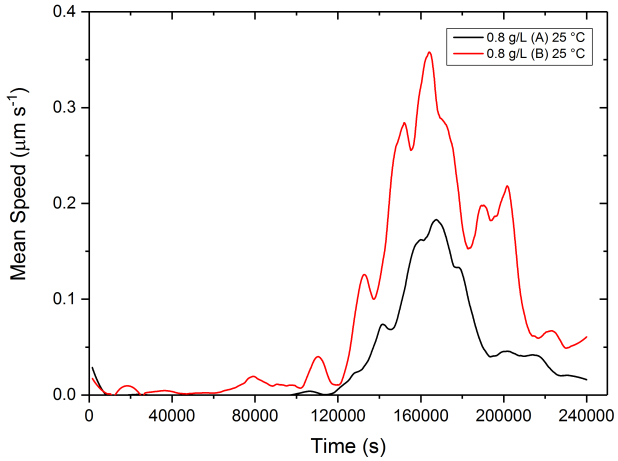

FIGURE 7.17: Smoothed PTV data for 2 different 0.8 g L^{-1} gels at 25 °C.

A repeat at 25 °C was performed and the mean speed plots are compared in Figure 7.17. Firstly, the value for τ_{max} for each sample is remarkably close, 167520 s and 164040 s for sample A and sample B respectively. Both samples exhibit the same behaviour, in that there is an initial amount of tracer settling, followed by an extended quiescent period, with a final peak in tracer speed to v_{max}. The values for v_{min} are similar with sample A having only minimal tracer movement in the quiescent period. Despite this marginal amount of tracer movement it does not appear to affect τ_{max} for sample B. Where the two samples differ dramatically is the value for v_{max}, with sample B having a value of 0.358 μm s^{-1} almost double the value of 0.183 μm s^{-1} for Sample A.

Sample	τ_{max}	v_{max}	v_{min}
A	164040	0.358	0.001
B	167520	0.183	0

TABLE 7.2: Summary of key values from two 0.8 g L^{-1} xanthan-PDMS gels at 25 °C, shown in Figure 7.17

This shows that whilst the speeds measured during a PTV experiment such as v_{max} and v_{min} do vary between sample, this doesn't necessarily impact the overall lifetime of the sample, with τ_{max} for both samples A and B being very similar. However this does raise the question of whether the trends observed as temperature is increased, with v_{max} seeming to rise with temperature in the low-temperature regime, and then tracer speed gradually reducing again in the high-temperature regime. However, this is of a greater magnitude than the difference between the two samples in Figure 7.17, with the variation between samples A and B being approximately 0.15 μm s^{-1}, and the change from 25 °to 45 °C for a 0.8 g L^{-1} gel being 0.8 μm s^{-1}.

7.7 Summary

In this chapter we have explored the application of the technique Particle Tracking Velocimetry to a colloidal gel, with an aim to probe the mesoscopic dynamics of the gel before macroscopic collapse is observed. We find that the two regimes of temperature response have fundamentally different dynamics before collapse, with low temperatures having a period of little to no tracer movement before a peak in tracer speed (v_{max}), the time at which this occurs τ_{max}, correlates well with the macroscopic delay time τ_d. Conversely, at high temperatures τ_{max} no longer correlates with τ_d, and the majority of tracer movement occurs before macroscopic collapse is observed, meaning that there is no period of quiescence. The extremes of the temperatures explored using PTV is shown below in Figure 7.18, which encapsulates both the significant difference in time-scale as well as the differing tracer movement between the low and high temperature regimes.

Further to this, at low temperatures we are able to observe the localised rupture of the strand network, with only a limited number of tracer beads moving initially before the failure eventually propagates throughout the gel sufficiently for it to collapse completely. Conversely, in the high-temperature regime, the tracer movement before collapse is homogeneous in nature, with no tracers appearing to be arrested within the network. This is an interesting observation as macroscopically the sample is still gelled rheologically as G$'$ is the same magnitude at all temperatures, with it being

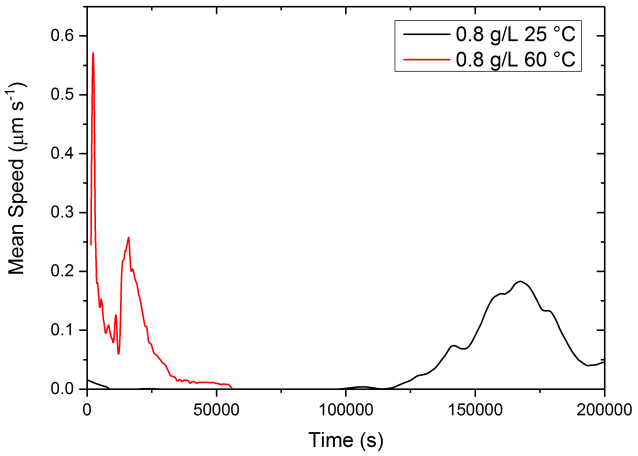

FIGURE 7.18: Smoothed PTV data for a 0.8 g L^{-1} at 25 °and at 60 °C.

greater than G'', showing that probing different length-scales gives a very different insight to the properties and dynamics of a gel.

We find that changing the depletion potential does not affect the magnitude of tracer speed observed before or during collapse, and only decreases τ_{max} in line with τ_d as observed in Chapter 5. This, as well as the fact that different samples of the same gel composition give both similar τ_{max}, v_{max}, and v_{min} values show that PTV is a reliable method to probe the mesoscopic changes within a gel at all points during it's lifetime, and has great scope for further refinement in the future.

Chapter 8

Conclusions

In this chapter we summarise the findings of this work. We begin by revisiting the main aims of this project, with the context of challenges in predicting and measuring industrial formulation stability. We then discuss how better control over temperature can affect a gel's lifetime, and compare our results to previous work using the same model colloid-polymer gel. We then summarise our findings when increasing temperature, finding a decrease in τ_d as temperature increases, we rationalise this response with an acceleration of the particle dynamics within the gel. We propose that temperature has no effect on the network formed within the gel, but using a combination of rheology and the method Particle Tracking Velocimetry, show that the structure of a gel ages in a different way at high and low temperatures. We conclude the chapter by discussing future work that could be performed, both broadening the body of collapse data as well as how PTV can be further developed into a strong tool for probing the mesoscopic length-scale in colloid-polymer gels.

8.1 Introduction

With various challenges facing gel formulation development, in this chapter we aim to summarise the findings of this work as well as their relevance to industrial challenges. As previously discussed, one of the main challenges facing industrial formulation development is time. With formulations requiring long-term stability and a limited tool-kit of techniques to determine stability at early times in a formulation's life, there is a significant drive towards accelerating the collapse of formulations for testing as well as development of techniques that give more information early in a gel formulation's lifetime. A more detailed summary of the challenges and techniques

used and their limitations can be found in the first section of both Chapter 1 and Chapter 4.

Some of the main questions of this thesis include:

- Does controlling temperature affect gel stability?
- Can we reliably accelerate gel collapse using temperature?
- Is gel stability wholly controlled by particle dynamics?
- Can we measure changes within a gel at early times?

In the next sections we answer, or at least begin to answer these questions, as well as propose future works that may yield a greater insight into some of the preliminary work using PTV.

8.2 Ambient Gel Collapse

Using a model xanthan-PDMS depletion gel, previously used by Teece [25], and Gilligan [106], as well a 3d printed cell-holder we have studied the macroscopic lifetime of gels whilst controlling the temperature to have less than a 0.1 °C variation throughout the experiment.

Comparing the delay time measured to previous measurements made by Teece and Gilligan, we find that by controlling the temperature to a higher degree increases the lifetime of gels of the same composition. Whilst the increase in τ_d compared to the work of Teece can be attributed to the change from cylindrical to rectangular vials, this is not the case for the work of Gilligan, as that work used the same rectangular vials as this work. This increase in τ_d despite the experiments in this work being carried out at 25 °C compared to 20 °C used previously, is presumably due to the significant reduction of temperature fluctuation throughout the experiment. This reduction in temperature variation within the sample reduces the internal stress of the sample and will narrow the distribution of coarsening events within the gel. Despite a difference in the value of τ_d measured, we continue to see the same exponential dependence of τ_d on polymer concentration.

We rationalise τ_d as a function of the individual bond breaking events occurring within the gel as it ages. We calculate the average particle-particle bond lifetime τ_{esc}, finding that as bond lifetime increases, so does the gel lifetime. One key difference between our calculation of τ_{esc} and the calculations of Teece et al. [25] is our use of the solvent viscosity η_0 rather than the polymer viscosity η_L. This value was chosen by considering the literature surrounding dynamics within depletion systems as well as our experimental data when increasing temperature, with the solvent viscosity scaled collapse data providing a horizontal region between 45 and 60 °C.

8.3 Temperature Accelerated Gel Collapse

With a common method of accelerating the collapse of formulations being storing them at higher temperatures, we expand our temperature control work to include temperatures up to 60 °C in 5 °C increments. Upon increasing temperature, we find a steep reduction in τ_d between 25 and 45 °C, above 45 °C there is still a reduction in τ_d but to a much lesser degree. Therefore we label these two regimes of temperature response the low-temperature and high-temperature regimes.

Having previously characterised the size of the depletant xanthan used in these colloid-polymer gels, we find that the crossover temperature between these two regimes of temperature response does not correspond to the conformation change of xanthan. This, as well as the fact that the crossover temperature shifts to higher temperatures for the highest polymer concentrations studied in this work, shows that this two regime response to temperature exhibited is not due to the change in conformation of xanthan.

We present preliminary data on a second system using a smaller polymer HEC-HHX, and observe a similar response to temperature, but no plateau regime due to the lower delay times generated using this polymer. However, due to the much stronger depletion potential generated ($\sim 30\ k_BT$) the Kramer's escape time has no correlation to the gel lifetime, however the height profiles appear similar to those of the xanthan-PDMS system.

Expanding on the relationship between τ_d and τ_{esc} at ambient temperature, we

calculate the escape time for each temperature studied, using the corresponding solvent viscosity η_0 for each temperature. We find that the ratio τ_d/τ_{esc} is independent of the xanthan concentration. We find that in the low-temperature regime, the ratio τ_d/τ_{esc} decreases as temperature increases, and then at $\sim$ 45 °C the ratio remains unchanged as temperature is increased further. This appears to fit with results of Sprakel et al. [60] who find that accelerating the rate of strand breakage using applied stress gives a two regime response to applied stress. With the first regime where the rate of strand healing is higher than strand breaking, which in our system would lead to a gradual coarsening of the network. In the high stress regime the rate of strand breaking is greater so the network never gets a chance to recover any damage and is just torn apart by the applied stress, this may well be the case in our high-temperature regime, where the gel cannot arrest the internal motion occurring and this rate of breakage is the determining factor in the gel collapse. Furthermore, whilst bond breakage does play a significant role in determining the stability of a formulation (as seen by the relation between τ_d and τ_{esc} at a single temperature) there is also another factor controlling gel collapse, which is not explained by only single-bond dynamics. We suggest that this may be the gel structure.

8.4 Gel Network Formation

With the hypothesis that the structure of a colloid-polymer gel also plays an important role in determining its stability, we explore the structure formed within freshly made gels at different temperatures, using oscillatory rheology.

We establish the rheological properties of PDMS-xanthan gels system at ambient temperature. The elastic G′ and viscous G″ moduli both increase with polymer concentration, with G′ being greater than G″ up to 14 % strain. The magnitude of G' increases from $\sim$ 0.8 to 1.05 Pa over the xanthan concentration range of 0.7 to 1.0 g L^{-1}, showing that the gels formed are very soft, which coupled with a viscous moduli of 0.4 and 0.8 Pa leads us to determine that these gels are weakly gelled. All gels studied have a linear regime up to 1 % strain, during which the applied strain has no effect on both G′ and G″, this again shows the weak nature of the gel network initially formed within the gel, agreeing with previous assertions [56] that the gel

network at early times consists of thinner particle strands, which over time coarsen into thicker strands.

We compare the gel structure formed at different temperatures within the low-temperature regime by performing strain sweeps at various temperatures. We find that increasing temperature has no effect on the magnitudes of both G' and G'', as well as the linear regime and the strain at which G' becomes lower than G''. Therefore, we can state that the response to temperature observed in the collapse data is not due to a fundamental change in the gel properties or structure at formation. To assess whether the crossover to the high-temperature regime is due to a change in the fundamental properties of a gel, a fixed strain is applied to a gel and the temperature ramped from 40 to 70 °C, to find if the rheological properties change when a gel is in the high-temperature regime. We find that the elastic modulus G' remains unchanged as temperature is increased into the high-temperature regime, showing that the gel structure remains unchanged, and that the PDMS droplets forming the structure remain intact and do not rupture.

With the structure of freshly prepared gels unchanged by temperature, we show preliminary time-resolved rheological data as a 1.0 g L^{-1} PDMS-xanthan gel ages at various temperatures. In this we find that the samples stiffen significantly quicker and to a much greater degree at higher temperatures, suggesting that the structural evolution is affected by temperature, which when coupled with the accelerated particle dynamics causes the drastic reduction in delay time observed.

8.5 Mesoscopic Changes Before and During Collapse

With the rheological data suggesting that the effect of temperature comes about through differing ageing dynamics, we use the method PTV to probe the intermediate length-scale between the previous macroscopic data and microscopic particle dynamics calculations. PTV allows us to observe movement within the gel well before macroscopic collapse is observed, which makes it a strong technique that can both collect information on a gel at all points during its lifetime, and be easily applied to a multitude of different systems.

We find that in the low-temperature regime there is a period of tracer quiescence before a gradual increase in tracer movement to a maximum value of tracer speed v_{max}. The time of maximum tracer movement τ_{max} correlates well with the delay time τ_d, suggesting a link with mesoscopic changes and macroscopic collapse. In the high-temperature regime there is no period of tracer quiescence and τ_{max} no longer correlates with τ_d. This lack of arrest of the gel lends credence to the argument that in the high-temperature regime strand breaking is the dominant force as the strands are not intact to hold the tracer beads in place.

However this leads to an apparent contradiction. As the rheological data shows that even up to 70 °C the sample is still gelled, and in the collapse data the 60 °C measurement for a 1.0 g L^{-1} xanthan-PDMS gel still has a delay time of $\sim$ 5 hours. This is where length-scale probed by each method must be considered, PTV is probing a much smaller length-scale than the macroscopic level that rheology and time-lapse microscopy observe. Which highlights another strength of PTV, in that the length-scale probed can be easily changed by adjusting the size of the tracer beads used.

With the preliminary data from PTV experiments we have limited spatial resolution of the dynamics within the sample. We observe that in the low-temperature regime tracer movement is heterogeneous in nature, as small localised areas of the gel rupture and then re-heal. Over time these small ruptures propagate throughout the gel, and eventually the gel is unable to recover from the failures and collapses macroscopically. However in the high-temperature regime tracer movement is homogeneous in nature, with all tracers moving at all times observed. This again supports the stranding breaking and healing arguments suggested above.

8.6 Future Work

With PTV showing great promise as a technique due to its ability to provide both time and spatially resolved data in one measurement the development of this technique would be an excellent next step in this work. Improving the throughput of the experimental set up by allowing imagining of multiple samples at once would be of great use, as currently only one may be observed at a time. However, the high

resolution of the PTV set up is one of it's main strengths, so ensuring little to no resolution is lost would be paramount. A cell-holder specifically designed for PTV experiments (cells closer together, thinner holder walls) would improve the field of view available when imagining cells, as well as make full illumination of multiple samples with a laser simpler.

With the increase in data collection the transfer and processing of data could also be improved up, as currently each image stack must be individually cropped and transferred, which coupled with the high resolution of the images collected leads to image stacks than can be up to twenty gigabytes in size. Whilst this is not a key change to improve the quality of data collected, it would indeed be a quality of life improvement when performing PTV experiments.

Further analysis of the current PTV available would also yield more information on the collapse of colloid-polymer gels, with parameters such as directional tracer movement, number of tracers, and distributions of tracer speed unanalysed in this work. However, insights may be limited due to the lack of depth resolution with the current analysis, as we currently can only asses a tracers x and y position in the sample, not its z position.

This leads on to the next major improvement to the current PTV set up, better spacial resolution. By using a different illumination method such as a scanning sheet of laser light (similar to that using in confocal microscopy) we would be able to accurately define the x, y, and z positions of each tracer bead and then generate 3D videos which would highlight areas of low or high movement throughout the sample. This would allow us to see where in the sample ruptures occur most often, such as near a wall, or at the top/bottom of the sample.

The other great strength of PTV is its transferability to a wide variety of dynamic and arrested systems. We believe the current methodology will be usable in an opaque system, given that sufficient tracer illumination and fluorescence can be achieved. With an opaque system seeing deep into the sample would be a challenge, a great deal of data could still be collected from probing near to the walls of a sample. This could possibly be overcome by the use of a different method of differentiating between tracer beads and the surrounding media that is not reliant on light. X-rays that can penetrate deep into an opaque sample and allow the movement of the tracers to be

tracked could be one such solution. Changing the size and nature of the tracer beads used would also allow PTV to be performed in a wide variety of different systems.

Further time-lapse experiments would also be a good avenue to broaden the scope of this work, using the same xanthan-PDMS system but changing the volume fraction of PDMS would be interesting, as this may change the low-temperature regime slope, or possibly shift the crossover temperature between the two regimes. Expanding the work using HEC HHX as a depletant would also be of great interest, however a significant amount of work would be required to characterise its properties at different temperatures.

Further work into the rich behaviour observed in this thesis would no doubt be fruitful and be of great interest both academically and industrially.

Bibliography

1. Marquez, L., Dunstall, S., Bartholdi, J. & Maccawley, A. 'Cool or hot': a study of container temperatures in Australian Wine Shipments. *Australasian Journal of Regional Studies* **18** (Jan. 1, 2012).

2. *Formulation Special Interest Group - Realising the Potential for Formulation in the UK* (2013).

3. McDonald, R. C., Mittelsteadt, C. K. & Thompson, E. L. Effects of Deep Temperature Cycling on Nafion® 112 Membranes and Membrane Electrode Assemblies. *Fuel Cells* **4,** 208–213 (July 2004).

4. Zhou, X., Baik, B.-K., Wang, R. & Lim, S.-T. Retrogradation of waxy and normal corn starch gels by temperature cycling. *Journal of Cereal Science* **51,** 57–65 (Jan. 1, 2010).

5. Freestone, I., Meeks, N., Sax, M. & Higgitt, C. The Lycurgus Cup — A Roman nanotechnology. *Gold Bulletin* **40,** 270–277 (Dec. 1, 2007).

6. Gwenin, V. V., Gwenin, C. D. & Kalaji, M. Colloidal Gold Modified with a Genetically Engineered Nitroreductase: Toward a Novel Enzyme Delivery System for Cancer Prodrug Therapy. *Langmuir* **27,** 14300–14307 (Dec. 6, 2011).

7. Hamaker, H. C. The London—van der Waals attraction between spherical particles. *Physica* **4,** 1058–1072 (Oct. 1, 1937).

8. Cosgrove, T. *Colloid Science: Principles, Methods and Applications* 400 pp. ISBN: 978-1-4443-2018-3 (John Wiley & Sons, Feb. 16, 2010).

9. Donald H. Napper. *Polymeric stabilization of colloidal dispersions / Donald H. Napper.* ISBN: 978-0-12-513980-9 (Academic Press, London, 1983).

10. Lekkerkerker, H. N. W. & Tuinier, R. *Colloids and the Depletion Interaction* 245 pp. ISBN: 978-94-007-1222-5 (Springer Science & Business Media, May 12, 2011).

11. Pusey, P. N. & Megen, W. v. Phase behaviour of concentrated suspensions of nearly hard colloidal spheres. *Nature* **320,** 340–342 (Mar. 1986).

12. Bosma, G. *et al.* Preparation of Monodisperse, Fluorescent PMMA–Latex Colloids by Dispersion Polymerization. *Journal of Colloid and Interface Science* **245,** 292–300 (Jan. 15, 2002).

13. Antl, L. *et al.* The preparation of poly(methyl methacrylate) latices in non-aqueous media. *Colloids and Surfaces* **17,** 67–78 (Jan. 1, 1986).

14. Phan, S.-E. *et al.* Phase transition, equation of state, and limiting shear viscosities of hard sphere dispersions. *Physical Review E* **54,** 6633–6645 (Dec. 1, 1996).

15. Smith, G. N., Finlayson, S. D., Rogers, S. E., Bartlett, P. & Eastoe, J. Electrolyte-induced Instability of Colloidal Dispersions in Nonpolar Solvents. *The Journal of Physical Chemistry Letters* **8,** 4668–4672 (Oct. 5, 2017).

16. Israelachvili, J. N. *Intermolecular and Surface Forces* 708 pp. ISBN: 978-0-12-391933-5 (Academic Press, July 22, 2011).

17. Derjaguin, B. On the repulsive forces between charged colloid particles and on the theory of slow coagulation and stability of lyophobe sols. *Transactions of the Faraday Society* **35,** 203–215 (Jan. 1, 1940).

18. Verwey, E. J. W., Overbeek, J. T. G. & Overbeek, J. T. G. *Theory of the Stability of Lyophobic Colloids* 228 pp. ISBN: 978-0-486-40929-0 (Courier Corporation, 1948).

19. Biggs, S., Habgood, M., Jameson, G. J. & Yan, Y.-d. Aggregate structures formed via a bridging flocculation mechanism. *Chemical Engineering Journal* **80,** 13–22 (Dec. 1, 2000).

20. Hart, P. Method of breaking reverse emulsions in a crude oil desalting system (May 9, 1995).

21. Asakura, S. & Oosawa, F. On Interaction between Two Bodies Immersed in a Solution of Macromolecules. *Journal of Chemical Physics* **22,** 1255–1256 (1954).

22. Asakura, S. & Oosawa, F. Interaction between particles suspended in solutions of macromolecules. *Journal of Polymer Science* **33,** 183–192 (Dec. 1, 1958).

23. Poon, W. C. K., Pirie, A. D. & Pusey, P. N. Gelation in colloid-polymer mixtures. *Faraday Discussions.* 101, 65–76 (1995).

24. Fleer, G. J. & Tuinier, R. Analytical phase diagrams for colloids and non-adsorbing polymer. *Advances in Colloid and Interface Science* **143,** 1–47 (Nov. 4, 2008).

25. Teece, L. J., Faers, M. A. & Bartlett, P. Ageing and collapse in gels with long-range attractions. *Soft Matter* **7,** 1341–1351 (2011).

26. Tuinier, R., ten Grotenhuis, E., Holt, C., Timmins, P. A. & de Kruif, C. G. Depletion interaction of casein micelles and an exocellular polysaccharide. *Physical Review E* **60,** 848–856 (July 1, 1999).

27. Milling, A. & Biggs, S. Direct Measurement of the Depletion Force Using an Atomic Force Microscope. *Journal of Colloid and Interface Science* **170,** 604–606 (Mar. 15, 1995).

28. Rudhardt, D., Bechinger, C. & Leiderer, P. Direct Measurement of Depletion Potentials in Mixtures of Colloids and Nonionic Polymers. *Physical Review Letters* **81,** 1330–1333 (Aug. 10, 1998).

29. Rudhardt, D., Bechinger, C. & Leiderer, P. Repulsive depletion interactions in colloid-polymer mixtures. *Journal of Physics: Condensed Matter* **11,** 10073 (1999).

30. Tuinier, R, Rieger, J & de Kruif, C. G. Depletion-induced phase separation in colloid–polymer mixtures. *Advances in Colloid and Interface Science* **103,** 1–31 (Mar. 19, 2003).

31. Verma, R., Crocker, J. C., Lubensky, T. C. & Yodh, A. G. Attractions between Hard Colloidal Spheres in Semiflexible Polymer Solutions. *Macromolecules* **33,** 177–186 (Jan. 1, 2000).

32. Lekkerkerker, H. N. W., Poon, W. C.-K., Pusey, P. N., Stroobants, A. & Warren, P. B. Phase Behaviour of Colloid + Polymer Mixtures. *EPL (Europhysics Letters)* **20,** 559 (Nov. 15, 1992).

33. Buscall, R. *et al.* Towards rationalising collapse times for the delayed sedimentation of weakly-aggregated colloidal gels. *Soft Matter* **5,** 1345–1349 (Mar. 24, 2009).

34. Ilett, S. M., Orrock, A., Poon, W. C. K. & Pusey, P. N. Phase behavior of a model colloid-polymer mixture. *Physical Review E* **51,** 1344–1352 (Feb. 1, 1995).

35. Lu, P. J. *et al.* Gelation of particles with short-range attraction. *Nature* **453,** 499–503 (May 22, 2008).

36. Zaccarelli, E., Lu, P. J., Ciulla, F., Weitz, D. A. & Sciortino, F. Gelation as arrested phase separation in short-ranged attractive colloid–polymer mixtures. *Journal of Physics: Condensed Matter* **20,** 494242 (2008).

37. Taylor, S. L., Evans, R. & Royall, C. P. Temperature as an external field for colloid–polymer mixtures: 'quenching' by heating and 'melting' by cooling. *Journal of Physics: Condensed Matter* **24,** 464128 (Nov. 21, 2012).

38. Berry, G. C. Thermodynamic and Conformational Properties of Polystyrene. I. Light-Scattering Studies on Dilute Solutions of Linear Polystyrenes. *The Journal of Chemical Physics* **44,** 4550–4564 (June 15, 1966).

39. Poon, W. C. K. *et al.* An experimental study of a model colloid-polymer mixture. *Journal de Physique II* **3,** 1075–1086 (July 1, 1993).

40. Tuinier, R., Fan, T.-H. & Taniguchi, T. Depletion and the dynamics in colloid–polymer mixtures. *Current Opinion in Colloid & Interface Science* **20,** 66–70 (Feb. 2015).

41. Fan, T.-H., Xie, B. & Tuinier, R. Asymptotic analysis of tracer diffusivity in nonadsorbing polymer solutions. *Physical Review E* **76,** 051405 (Nov. 16, 2007).

42. Fan, T.-H., Dhont, J. K. G. & Tuinier, R. Motion of a sphere through a polymer solution. *Physical Review E* **75,** 011803 (Jan. 19, 2007).

43. Fan, T.-H. & Tuinier, R. Hydrodynamic interaction of two colloids in nonadsorbing polymer solutions. **6,** 647–654 (Jan. 28, 2010).

44. Zaccarelli, E. Colloidal gels: equilibrium and non-equilibrium routes. *Journal of Physics: Condensed Matter* **19,** 323101 (Aug. 15, 2007).

45. Martin, J. E. & Adolf, D. The Sol-Gel Transition in Chemical Gels. *Annual Review of Physical Chemistry* **42,** 311–339 (1991).

46. Bartlett, P., Teece, L. J. & Faers, M. A. Sudden collapse of a colloidal gel. *Physical Review E* **85.** 2, 021404 (2012).

47. Sedgwick, H., Egelhaaf, S. U. & Poon, W. C. K. Clusters and gels in systems of sticky particles. *Journal of Physics: Condensed Matter* **16,** S4913 (Oct. 27, 2004).

48. Varadan, P. & Solomon, M. J. Shear-Induced Microstructural Evolution of a Thermoreversible Colloidal Gel. *Langmuir* **17,** 2918–2929 (May 1, 2001).

49. Grant, M. C. & Russel, W. B. Volume-fraction dependence of elastic moduli and transition temperatures for colloidal silica gels. *Physical Review E* **47,** 2606–2614 (Apr. 1, 1993).

50. Kim, S. Y. & Zukoski, C. F. Role of Polymer Segment–Particle Surface Interactions in Controlling Nanoparticle Dispersions in Concentrated Polymer Solutions. *Langmuir* **27,** 10455–10463 (Sept. 6, 2011).

51. Starrs, L., Poon, W. C. K., Hibberd, D. & Robins, M. Collapse of transient gels in colloid-polymer mixtures. *Journal of Physics: Condensed Matter* **14,** 2485–2509 (2002).

52. Derec, C., Senis, D., Talini, L. & Allain, C. Rapid settling of a colloidal gel. *Physical Review E* **67.** 6 (June 2003).

53. Lietor-Santos, J. J., Kim, C., Lu, P., Fernandez-Nieves, A. & Weitz, D. Gravitational compression of colloidal gels. *European Physical Journal E* **28.** 2, 159–164 (Feb. 2009).

54. Poon, W. C. K. *et al.* Delayed sedimentation of transient gels in colloid–polymer mixtures: dark-field observation, rheology and dynamic light scattering studies. *Faraday Discussions* **112,** 143–154 (Jan. 1, 1999).

55. Gopalakrishnan, V., Schweizer, K. S. & Zukoski, C. F. Linking single particle rearrangements to delayed collapse times in transient depletion gels. *Journal of Physics-Condensed Matter* **18.** 50, 11531–11550 (Dec. 2006).

56. Teece, L. J. *et al.* Gels under stress: The origins of delayed collapse. *Colloids and Surfaces A: Physicochemical and Engineering Aspects* (Mar. 31, 2014).

57. Tanaka, H., Nishikawa, Y. & Koyama, T. Network-forming phase separation of colloidal suspensions. *Journal of Physics: Condensed Matter* **17,** L143 (2005).

58. Tanaka, H. & Araki, T. Spontaneous coarsening of a colloidal network driven by self-generated mechanical stress. *EPL (Europhysics Letters)* **79,** 58003 (2007).

59. Zia, R. N., Landrum, B. J. & Russel, W. B. A micro-mechanical study of coarsening and rheology of colloidal gels: Cage building, cage hopping, and Smoluchowski's ratchet. *Journal of Rheology (1978-present)* **58,** 1121–1157 (Sept. 1, 2014).

60. Sprakel, J., Lindström, S. B., Kodger, T. E. & Weitz, D. A. Stress Enhancement in the Delayed Yielding of Colloidal Gels. *Physical Review Letters* **106,** 248303 (June 17, 2011).

61. Smith, P. A., Petekidis, G., Egelhaaf, S. U. & Poon, W. C. K. Yielding and crystallization of colloidal gels under oscillatory shear. *Physical Review E* **76,** 041402 (Oct. 15, 2007).

62. Harich, R. *et al.* Gravitational collapse of depletion-induced colloidal gels. **12,** 4300–4308 (May 11, 2016).

63. Carpineti, M. & Giglio, M. Spinodal-type dynamics in fractal aggregation of colloidal clusters. *Physical Review Letters* **68,** 3327–3330 (June 1, 1992).

64. Verhaegh, N. A. M., Asnaghi, D., Lekkerkerker, H. N. W., Giglio, M. & Cipelletti, L. Transient gelation by spinodal decomposition in colloid-polymer mixtures. *Physica A: Statistical Mechanics and its Applications* **242,** 104–118 (Aug. 1, 1997).

65. Lu, P. J. & Weitz, D. A. Colloidal Particles: Crystals, Glasses, and Gels. *Annual Review of Condensed Matter Physics* **4,** 217–233 (2013).

66. Weeks, E. R. & Weitz, D. A. Properties of Cage Rearrangements Observed near the Colloidal Glass Transition. *Physical Review Letters* **89,** 095704 (Aug. 12, 2002).

67. Trappe, V., Prasad, V., Cipelletti, L., Segre, P. N. & Weitz, D. A. Jamming phase diagram for attractive particles. *Nature* **411,** 772–775 (June 2001).

68. Liu, A. J. & Nagel, S. R. Nonlinear dynamics: Jamming is not just cool any more. *Nature* **396,** 21–22 (Nov. 1998).

69. Fleer, G. J., Skvortsov, A. M. & Tuinier, R. A Simple Relation for the Concentration Dependence of Osmotic Pressure and Depletion Thickness in Polymer Solutions. *Macromolecular Theory and Simulations* **16,** 531–540 (July 23, 2007).

70. Milas, M. & Rinaudo, M. Properties of xanthan gum in aqueous solutions: Role of the conformational transition. *Carbohydrate Research* **158,** 191–204 (Dec. 15, 1986).

71. Matsuda, Y., Biyajima, Y. & Sato, T. Thermal Denaturation, Renaturation, and Aggregation of a Double-Helical Polysaccharide Xanthan in Aqueous Solution. *Polymer Journal* **41,** 526–532 (Apr. 29, 2009).

72. Pelletier, E., Viebke, C., Meadows, J. & Williams, P. A. A rheological study of the order–disorder conformational transition of xanthan gum. *Biopolymers* **59,** 339–346 (Oct. 15, 2001).

73. Milas, M. & Rinaudo, M. Conformational investigation on the bacterial polysaccharide xanthan. *Carbohydrate Research* **76,** 189–196 (Nov. 1979).

74. Liu, W. & Norisuye, T. Thermally induced conformation change of xanthan: interpretation of viscosity behaviour in 0.01 m aqueous sodium chloride. *International Journal of Biological Macromolecules* **10,** 44–50 (Feb. 1988).

75. Dixon, M. A thermostat cell-holder for the Beckman spectrophotometer. *Biochemical Journal* **58,** 1–3 (Sept. 1954).

76. *Ormerod2 Documentation* RepRapPro.

77. Goodwin, J. & Hughes, R. *Rheology for Chemists* ISBN: 978-0-85404-839-7 (Jan. 22, 2008).

78. *Understanding Rheology of Structured Fluids* TA Instruments.

79. Adrian, R. J. Particle-Imaging Techniques for Experimental Fluid Mechanics. *Annual Review of Fluid Mechanics* **23,** 261–304 (1991).

80. Kasagi, N. & Matsunaga, A. Three-dimensional particle-tracking velocimetry measurement of turbulence statistics and energy budget in a backward-facing step flow. *International Journal of Heat and Fluid Flow* **16,** 477–485 (Dec. 1, 1995).

81. Malik, N. A., Dracos, T. & Papantoniou, D. A. Particle tracking velocimetry in three-dimensional flows. *Experiments in Fluids* **15,** 279–294 (Sept. 1, 1993).

82. Allan, D. *et al. Trackpy: Trackpy V0.2.4* Oct. 15, 2014.

83. Crocker, J. C. & Grier, D. G. Methods of Digital Video Microscopy for Colloidal Studies. *Journal of Colloid and Interface Science* **179,** 298–310 (Apr. 15, 1996).

84. Shaw, F. *Investigating the Collapse Dynamics of Colloidal Gels through Particle Tracking Velocimetry.* Thesis (University of Bristol, June 2017).

85. Savitzky, A. & Golay, M. J. E. Smoothing and Differentiation of Data by Simplified Least Squares Procedures. *Analytical Chemistry* **36,** 1627–1639 (July 1, 1964).

86. Steinier, J., Termonia, Y. & Deltour, J. Smoothing and differentiation of data by simplified least square procedure. *Analytical Chemistry* **44,** 1906–1909 (Sept. 1, 1972).

87. Zhang, I., Royall, C. P., Faers, M. A. & Bartlett, P. Phase separation dynamics in colloid-polymer mixtures: the effect of interaction range. *Soft Matter* **9.** 6, 2076–2084 (2013).

88. Sun, T. & Teja, A. S. Density, Viscosity, and Thermal Conductivity of Aqueous Ethylene, Diethylene, and Triethylene Glycol Mixtures between 290 K and 450 K. *Journal of Chemical & Engineering Data* **48,** 198–202 (Jan. 1, 2003).

89. Garcia-Ochoa, F, Santos, V. E, Casas, J. A & Gomez, E. Xanthan gum: production, recovery, and properties. *Biotechnology Advances* **18,** 549–579 (Nov. 1, 2000).

90. Katzbauer, B. Properties and applications of xanthan gum. *Polymer Degradation and Stability. Biodegradable Polymers and Macromolecules* **59,** 81–84 (Jan. 3, 1998).

91. Avery, M. P. *et al.* The Rheology of Dense Colloidal Pastes Used in 3D-Printing. *NIP & Digital Fabrication Conference* **2014,** 140–145 (Jan. 1, 2014).

92. Hamman, J. H. Chitosan Based Polyelectrolyte Complexes as Potential Carrier Materials in Drug Delivery Systems. *Marine Drugs* **8,** 1305–1322 (Apr. 19, 2010).

93. Zhong, L & Oostrom, M. Rheological behavior of xanthan gum solution related to shear thinning fluid delivery for subsurface remediation. *Journal of hazardous materials* **244-245C,** 160–170 (2012).

94. Wignall, G. D., Ballard, D. G. H. & Schelten, J. Measurements of persistence length and temperature dependence of the radius of gyration in bulk atactic polystyrene. *European Polymer Journal* **10,** 861–865 (Sept. 1974).

95. Kestin, J., Sokolov, M. & Wakeham, W. A. Viscosity of liquid water in the range -8 °C to 150 °C. *Journal of Physical and Chemical Reference Data* **7,** 941–948 (July 1, 1978).

96. Yamakawa, H. & Fujii, M. Intrinsic Viscosity of Wormlike Chains. Determination of the Shift Factor. *Macromolecules* **7,** 128–135 (Jan. 1, 1974).

97. Benoit, H. & Doty, P. Light Scattering from Non-Gaussian Chains. *The Journal of Physical Chemistry* **57,** 958–963 (Sept. 1, 1953).

98. Schmidt, M. Combined integrated and dynamic light scattering by poly(y-benzyl glutamate) in a helocogenic solvent. *Macromolecules* **17,** 553–560 (Apr. 1, 1984).

99. Buscall, R. & White, L. R. The consolidation of concentrated suspensions. Part 1.—The theory of sedimentation. *Journal of the Chemical Society, Faraday Transactions 1: Physical Chemistry in Condensed Phases* **83,** 873–891 (Jan. 1, 1987).

100. Kilfoil, M. L., Pashkovski, E. E., Masters, J. A. & Weitz, D. A. Dynamics of weakly aggregated colloidal particles. *Philosophical Transactions of the Royal Society of London A: Mathematical, Physical and Engineering Sciences* **361,** 753–766 (Apr. 15, 2003).

101. Glasrud, G. G., Navarrete, R. C., Scriven, L. E. & Macosko, C. W. Settling behaviors of iron oxide suspensions. *AIChE Journal* **39,** 560–568 (Apr. 1993).

102. Curvers, D. *et al.* The influence of ionic strength and osmotic pressure on the dewatering behaviour of sewage sludge. *Chemical Engineering Science* **64,** 2448–2454 (May 15, 2009).

103. Brooks, K. P., Rector, D. R. & Smith, P. A. Gravity Settling of Hanford Single-Shell Tank Sludges. *Separation Science and Technology* **34,** 1351–1370 (Jan. 1, 1999).

104. Kim, C. *et al.* Gravitational Stability of Suspensions of Attractive Colloidal Particles. *Physical Review Letters* **99,** 028303 (July 11, 2007).

105. Teece, L. *Controlling the Collapse of Weak Colloid-Polymer Gels* PhD thesis (University of Bristol, June 2011).

106. Gilligan, S. *Delayed Gravitational Collapse of Colloid-Polymer Gels* PhD thesis (University of Bristol, Nov. 2017).

107. Yen Ni Hsu, K. *The Synthesis and Assembly of Janus, Ternary and Patchy Particles & Understanding the Collapse of a Colloidal Gel* PhD thesis (University of Bristol, Apr. 4, 2012).

108. Zhang, I. *A Real-Space Study of Phase Behaviour and Slow Dynamics in Colloid-Polymer Mixtures* PhD thesis (University of Bristol, June 2014).

109. Fielding, S. M. Shear banding in soft glassy materials. *Reports on Progress in Physics* **77,** 102601 (2014).